Radio Frequency Spectroscopy Of a Quasi-Two-Dimensional Fermi Gas

by

Yingyi Zhang

Department of Physics
Duke University

Date:____________________________
Approved:

____
John Thomas, Supervisor

____
Haiyan Gao

____
Ashutosh Kotwal

____
Harold Baranger

____
Glenn Edwards

Dissertation submitted in partial fulfillment of the
requirements for the degree of Doctor of Philosophy
in the Department of Physics
in the Graduate School of
Duke University

2013

ABSTRACT

(Physics)

Radio Frequency Spectroscopy Of a Quasi-Two-Dimensional Fermi Gas

by

Yingyi Zhang

Department of Physics
Duke University

Date:____________________________
Approved:

____
John Thomas, Supervisor

____
Haiyan Gao

____
Ashutosh Kotwal

____
Harold Baranger

____
Glenn Edwards

An abstract of a dissertation submitted in partial fulfillment of
the requirements for the degree of Doctor of Philosophy
in the Department of Physics
in the Graduate School of
Duke University

2013

Abstract

This dissertation presents the first experiments on radio frequency (rf) spectroscopy of a quasi-two dimensional strongly interacting ultracold atomic Fermi gas. A 50-50 mixture of spin-up and spin-down atoms is confined in a series of pancake-shaped traps produced using an optical standing-wave. To make the system quasi-two dimensional, I adjust the Fermi energy in the weakly confined direction to be comparable to the harmonic oscillator energy level spacing in the tightly confined direction. For a perfectly two dimensional system, at low enough temperature, spin-up and spin-down atoms should form dimers in the ground state of the tightly confined direction. However, in our quasi-two dimensional system I find that the simple dimer theory does not agree with the measured radio-frequency spectra. Instead, the data can be explained by polaron to polaron transitions, which is a many-body effect. Here, a polaron is a spin-down impurity surrounded by a cloud of particle-hole pairs in a spin-up Fermi sea. With this unique strongly interacting quasi-two dimensional system, I am able to study the interplay between confinement induced two-body pairing and many-body physics in confined mesoscopic systems of several hundred atoms, which has not been previously explored and offers new challenges for predictions.

Acknowledgements

I finally reach the point that I can write my dissertation and prepare for graduation. When I look back the whole journey as a graduate student, I feel so lucky to learn from and work with the people I have been with these years.

I owe a great debt of gratitude to my advisor Dr. John Thomas. I still remember my first time talking to John and trying to join his group, he told me "We are doing very, very hard experiments." Looking back my life working in the lab, I agree this sentence more than in the beginning although I am quite familiar with what we are doing. I gain confidence at the same time while learning to be alert and patient when doing endless trouble shooting in the lab. I would like to thank John for giving me the opportunity to work within his group. He is definitely a world class physicist. The positive atmosphere around him attracts us to work like a big family. He always says "We are having fun!" Talking with him in the morning makes me full of energy for a whole day. The completion of this dissertation would not have been possible without his encouragement and support. As well as advisor, he is my good friend. We went to lunch together after moved to NCSU and shared personal stories with each other besides research ideas. I believe this friendship will last a lifetime even after I leave this group.

I am indebted to senior students Bason and Le. They built up the equipment system from scratch in our lab right before I joined the group. They trained me in their last days here and I really admire them not only because they are senior and really experts, but also they are so humble, nice and patient. I felt the family atmosphere and decided to join this group after working with them for the first summer. In the five years after that I tried my best to take good care of the apparatus in our lab and treated it as my baby also because I appreciate the efforts Bason and Le put in.

After Bason and Le left, I worked with postdoc Du who became my mentor and good friend later. He taught me a lot, from we need to use pen instead of pencil to take lab note, to we should never give up and believe in science. Trouble shooting with him for one year, I learnt from him details of experiments as well as the method to see big physics pictures behind them. I can not say enough good things about him.

I want to thank Jessie, who is another postdoc in our group but working in another lab when Du was here. He always respected my opinion when we discussed even when I was quite junior. That makes me feel involved in my early days in the group and start gaining confidence since then. He is a good teacher in every aspect and good luck with his career as a teaching professor.

After I became the leading student in the lab, I asked for help from and discussed problems with three postdocs in our lab, Ilya, James and Haibin. I am so affected by Ilya's positive attitude that right now I also believe that the best place in the world is the place where I am. Although James works in another lab, he always appears at the time when I want to ask him questions. The talking I have with Haibin who reads all the possible papers inspires me many new ideas.

I also feel lucky to work with all the students in our group. Chenglin who has already left our group was in my batch. We were competitors and friends.

I want to wish Willie luck in his experiment, who I treat as my little brother. I will miss Chingyun, the girl who is smart and warm hearted. I also wish Ethan luck, the strong man working in the next lab. The new members in our group, a sweet couple, Arun and Nithya seem to get involved in our JETlab family very well. The future of the lab looks bright with all of them.

Outside our group, I want to thank professor Haiyan Gao who I asked first to become my committee member since she is as respectable as a role model and as nice as a friend, who you can share personal story with. She is always supportive and tries to encourage me while we are talking. I want to thank professor Glenn Edwards who I like since taking his quantum class in my first year. As my committee member, he cares about my progress in research and even spent time talking with me and let me show him around in the lab. I also want to thank professor Harold Baranger who was my "faculty mentor" for my first year here and later becomes my committee member as well. I still remember that he invited me to his cozy family dinner after heard about that I felt lonely in my first few days in America. I really appreciate that. It seems I asked all the nice professors to be my committee members. The same thing happened to professor Ashutosh Kotwal who was our instructor for the seminar techniques class in my third year. I was encouraged by him and put so much effort into this class in order to win the first place in the final poster competition. I still have my "first place" tag in my drawer. I also want to thank professor Richard Palmer, who was our director of graduate studies. I took his mathematical methods course in my first year, and he was a great teacher with a sense of humor. We share the same hobby, taking pictures. He organized many get-together events for graduate students, even invited us to visit his wooden house. I want to thank our DGSA Donna Rugar, my Duke mom, for her help in these years.

I got help from and became friends with other graduate students in and outside physics department. Dong Liu, the best in my batch, helped me a lot in the homework discussions in my first two years in Duke. I used to go to everywhere with Shangying Wang before I became stuck in the lab. I want to thank Wangzhi Zheng to be my wedding day photographer, Min Huang to be my sweet little sister and Jie Ren to share experience as parent with me.

Last but not least, I want to thank my parents for their endless support. I want to thank my husband for his encouragement and love. I also want to thank my new born daughter, if she has a chance to see this, for making this thesis writing no so easy.

Contents

List of Tables

List of Figures

Chapter 1

Introduction

My dissertation is on the radio frequency spectroscopy of a quasi-two dimensional ultracold strongly interacting Fermi gas, which contains a 50-50 mixture of the lowest two hyperfine states of ^{6}Li, $|1\rangle$ and $|2\rangle$. Strong interactions are achieved using a magnetically tunable collisional (Feshbach) resonance. An optical standing wave confines the atom cloud in a series of pancake-shaped traps as shown in Figure 1.1. The harmonic oscillation frequency ν_z in the tightly confined direction is about 25 times $\nu_\perp$, where $\nu_\perp$ is the oscillation frequency in the weakly confined transverse plane.

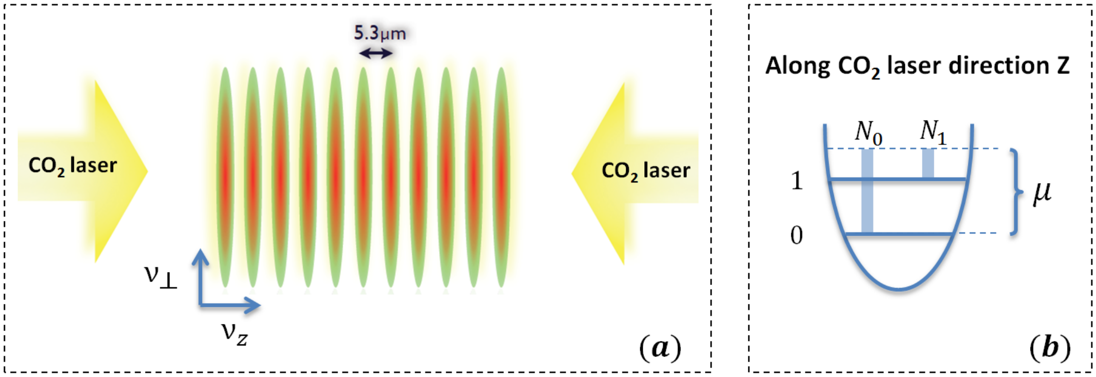

Figure 1.1: CO_2 laser standing wave trap (a) and axial energy level (b).μ shows the chemical potential for N_0 atoms in the ground state and N_1 in the first excited state.

The highest occupied energy level in the transverse plane at zero temperature is the transverse Fermi energy $E_{F\perp}$. When all atoms are in the ground axial state, $E_{F\perp} = h\nu_\perp\sqrt{N}$, which determines the geometry of the system. Here N is the total atom number in one pancake, which can be measured experimentally. When $E_{F\perp}$ is much smaller than the energy spacing $h\nu_z$ in the axial direction, the system approaches the ideal 2D limit and all the atoms are in the axial ground state. When $E_{F\perp}$ is comparable to $h\nu_z$, the system is quasi-2D and can be described by using a few axial states as shown in Figure 1.1(b) [1]. In our quasi-2D system, $E_{F\perp} \simeq 1.5h\nu_z$, but more than 90% of the atoms are still in the axial ground state at zero temperature.

The 2D confinement induces atoms to bind into dimers even when the atoms would be unbound in free space in 3 dimensions. Several groups have observed radio frequency spectra, through which the dimer binding energy E_b can be measured. The measurements agree with dimer theory when $E_{F\perp} \ll h\nu_z$ [2] [3]. In our experiment $E_{F\perp} \simeq 1.5h\nu_z$ and E_b is magnetically tunable. In the strongly interacting region near the Feshbach resonance $E_b \simeq 0.25h\nu_z$. Here we observe a large discrepancy with dimer theory predictions [4].

Since in the strongly interacting region E_b is comparable to $E_{F\perp}$, in other words, the dimer size is comparable to the interparticle spacing, many-body modification of the dimer binding energy is a possible explanation for our observed discrepancies. This strongly interacting many-body modification does not exist in a nearly 2D system, where $E_{F\perp} \ll h\nu_z$. In order to have many-body effects, where $E_b \sim E_{F\perp}$, the binding energy needs to be small $E_b \ll h\nu_z$ and the system is weakly interacting. The weakly interacting many-body effect gives no modification to dimer theory since 2D BCS theory [5], which describes the system, gives the same prediction as dimer theory.

Table 1.1: Comparison of 2D and quasi-2D systems.

2D	Quasi-2D
$E_{F\perp} \ll h\nu_z$	$E_{F\perp} \sim h\nu_z$
for $E_{F\perp} \sim E_b$, require $E_b \ll h\nu_z$ weakly interacting many-body system	for $E_{F\perp} \sim E_b$, require $E_b \sim h\nu_z$ strongly interacting many-body system
explainable by dimer theory and 2D BCS theory	can not be explained by simple dimer theory

2D BCS theory is not applicable in the strongly interacting region. However, we find that our data can be explained by transitions between non-interacting 2D polaron states. Here a polaron is an atom in one hyperfine state surrounded by a cloud of particle-hole pairs in another hyperfine state. Table 1.1 lists the comparison of 2D and quasi-2D systems. This dissertation is the first study of pairing in a quasi-two dimensional Fermi gas [4]. Our experiments have spurred several theoretical works [1, 6, 7] in order to understand how the system changes in the quasi-2D geometry.

1.1 Background

In order to explain my work, background knowledge of this field is necessary. In §1.1.1, I will generally introduce some previous research in ultracold Fermi gases and its importance. In §1.1.2, the key concepts "Feshbach resonance", by which the system achieves strongly interaction, and "BEC-BCS crossover" will be introduced.

1.1.1 Fermi gases with tunable interactions

Optical methods have been used to control and study atomic systems for a long time. Currently, a large branch of modern physics is atomic, molecular and optical (AMO) physics. In AMO physics, laser cooling and trapping of atoms is a rapidly developing area. In 1997, the Nobel Prize was given for laser cooling and trapping of neutral atoms. But the real boom in this field started from the realization of Bose-Einstein condensation (BEC) in 1995, which led to the Nobel price in 2001. This condensation means that when the system is cooled down to a certain transition temperature all the bosons occupy the ground state in energy space. Although BEC was theoretically predicted in papers by Satyendra Nath Bose and Albert Einstein in 1924−25, it took nearly 70 years to be realized. Many experiments have been done since then to study this novel phase of matter. While research in cold Bose systems was still active, laser cooling techniques started being used to cool Fermi gases.

Fermi gases are more important for understanding nature than Bose gases. Fermions are the building blocks of matter, like protons, neutrons and electrons. According to Pauli-exclusion principle, only one fermion can occupy one quantum state. So, even at zero temperature, fermions must pile up in energy space, one for each energy state, instead of crowding in the ground state like bosons. Although there is no BEC, ultracold Fermi systems have another novel phase of matter, superfluid pairs.

Quantum effects become paramount when the system reaches quantum degeneracy. As the atomic Fermi gas is cooled down, the de Broglie wavelength λ_T of the atoms increases since $\lambda_T = h/(\sqrt{2\pi m k_B T})$. We call the system degenerate when the wave packets of the particles start overlapping with each other. In other words, the de Broglie wavelength of atoms is comparable to the interparticle spacing, where $n_3\lambda_T^3 \sim 1$ in a 3D system or $n_2\lambda_T^2 \sim 1$ in a 2D system. Here n is the atomic density. Degenerate Fermi gases have been created since 1999 by using several methods, such as double rf knife evaporative cooling of ^{40}K in a magnetic trap [8], sympathetic cooling ^{6}Li with ^{7}Li in a magnetic trap [9–11] and evaporative cooling in an optical dipole trap [12, 13].

In 2002, the first degenerate strongly interacting degenerate Fermi gas was created by our group at Duke in ^{6}Li [14]. Anisotropic expansion in this system provided an early suggestion of the existence of quantum Fermi superfluid. We choose the alkali atom ^{6}Li because of its simple atomic structure and the fact that it has a broad collisional (Feshbach) resonance. We keep it as gas in order to make the system dilute. In other words, we want the interparticle spacing to be much longer than the effective range of the atomic potential. This assures that two-atom collisions dominate, which gives us a simple system to study since we can ignore collisions involving three or more atoms. This is also very important for achieving resonant scattering in a Fermi gas, which leads to strong interactions.

In this ultracold Fermi gas, atoms interact with each other by collisions. The atoms can not see the details of the atomic potential when they collide, since the de Broglie wavelength is much longer than the effective range R. The atoms only feel the potential at long length scales, which is described by quantum scattering theory. The formal way to solve this scattering problem is to do a partial wave expansion in the angular momentum components l of the incoming and outgoing waves. Since the atoms move so slowly, $l = R/\lambda_B \ll 1$, only the lowest order $l = 0$ wave matters, which is spherically symmetric, so called s-wave scattering. The atomic potential look like large symmetric balls in collisions. The incoming atom can not see any detailed structure of the scattering potential. The strength of the collisional interaction between the atoms is determined by the s-wave scattering length for the two spin states. When the interaction between atoms is strong, the behavior of Fermi system will not depend on the details of the atomic potential. We call such a gas a unitary Fermi gas. The only length scales that matter in the system are the average interparticle spacing, which is determined by the density n, and the thermal de Broglie wavelength λ_T. The unitarity of the ultracold Fermi gas allows it share similarity with other strongly interacting Fermi systems in nature [15–17], such as quark-gluon plasma and neutron matters [18].

Let me take an example of the anisotropic expansion behavior we observed in our Fermi gas [14]. This unique hydrodynamic behavior is called "elliptic flow" [14]. Similar hydrodynamic expansion has been observed in the quark gluon plasma created at the Relativistic Heavy Ion Collider (RHIC) at Brookhaven National Laboratory. The quark-gluon plasma is an extreme form of matter that is believed to have existed tens of μs after the Big Bang. It is remarkable that the quark-gluon plasma is 19 orders of magnitude higher in temperature and 25 orders of magnitude higher in density than our ultracold dilute Fermi gas, yet both systems have similar hydrodynamic behavior and extremely low viscosity. In addition, there is an interesting connection to string theory, which predicts a minimum ratio of shear viscosity to entropy density for a broad class of strongly interacting systems [19].

A high temperature superconductor also has similarity with the strongly interacting Fermi gases. The "high temperature" here is relative to the "ordinary" or metallic superconductors which usually have transition temperatures close to absolutely zero. The highest known transition temperature is 138 K which is still around 160 degrees lower than room temperature. BCS theory successfully explained ordinary superconductivity by using loosely bound Cooper pairs formed by spin-up and spin-down electrons in momentum space. This type of pairing leads to superfluidity below a critical temperature T_c. This critical temperature T_c can be raised by increasing the interaction strength between atoms. Employing a collisional (Feshbach) resonance as discussed below we can tune the interaction so that T_c is a large fraction of the Fermi temperature T_F, roughly $T_c/T_F = 0.20$ [20–25] in strongly interacting Fermi gases. However, for a metal, T_F is on the order of thousands of degrees Kelvin. If the critical temperature for superconductivity in a solid scaled the same way as in our Fermi gas, it would be far above room temperature. The similarity of these two systems can be used to test current theoretical predictions for high temperature superconductors.

1.1.2 Feshbach resonance in ^{6}Li and BEC-BCS crossover

A Feshbach resonance in the s-wave scattering between two states is the key to obtain strong interactions [26].The Pauli exclusion principle prevents identical fermions from s-wave scattering. In order to have interaction, we use a two-component Fermi gas with atoms in two of the lowest three hyperfine states of ^{6}Li. I will discuss these states in detail in Chapter 2.

Feshbach resonance arise in nuclear physics and is named after physicist Herman Feshbach [27]. It was predicted that a Feshbach resonance would exist in alkali atomic systems in 1993 [28]. Alkali atoms have only one valence electron ($s = 1/2$). For a two-atom system, the spin state can be either singlet ($S = s_1 + s_2 = 0$, $M_s = 0$) or triplet ($S = s_1 + s_2 = 1, M_s = -1, 0, 1$). Here S is the total electron spin number and M_s is the z-component projection.

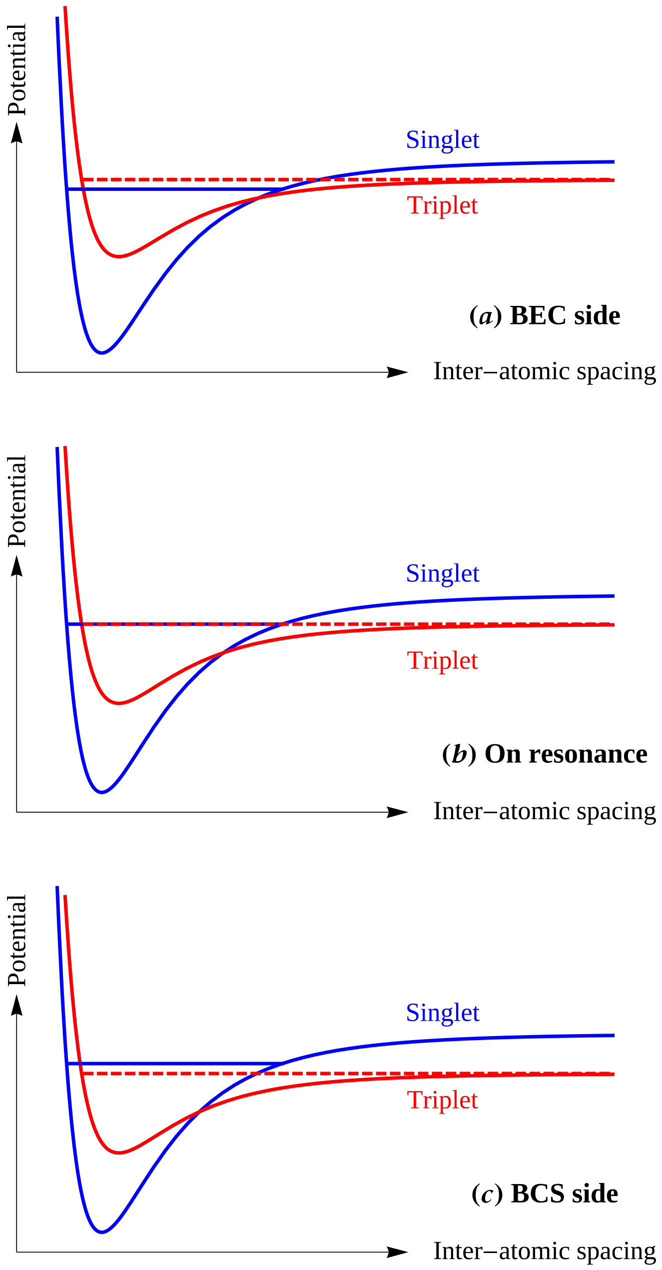

Figure 1.2: Relative positions of atomic potentials of singlet and triplet states around Feshbach resonance. Three different relative positions of energy levels of singlet bound state (solid horizontal blue line) and triplet scattering state (red dashed line) are shown. (a) corresponds to BEC side; (b) corresponds to on resonance; (c) corresponds to BCS side.

In Figure 1.2, schematics of molecular potentials for both singlet and triplet states are shown. Bound molecular states exist in the deep singlet potential. Here we only consider the highest one. For the shallow triplet potential, the incoming two-atom scattering state is higher in energy than the singlet bound state in the energy space. When an external magnetic field is applied, the Zeeman shift for the triplet scattering state changes the relative position of its energy level with respect to the singlet bound state. Feshbach resonance happens when the energy of the triplet scattering state is tuned to the singlet bound state energy. In our ^{6}Li atomic system, for high magnetic field, single atoms in hyperfine states $|1\rangle$, $|2\rangle$ or $|3\rangle$ are mostly $m_s = -1/2$ as shown in Table 2.2 and Figure 2.1. Hence the total spin state for two colliding atoms state is a triplet state. Electron magnetic moments dominate while the nuclear moment is 10^4 times smaller. Since only the energy of the triplet state can be tuned by external magnetic field, any mixture of two of these three hyperfine states can have a Feshbach resonance.

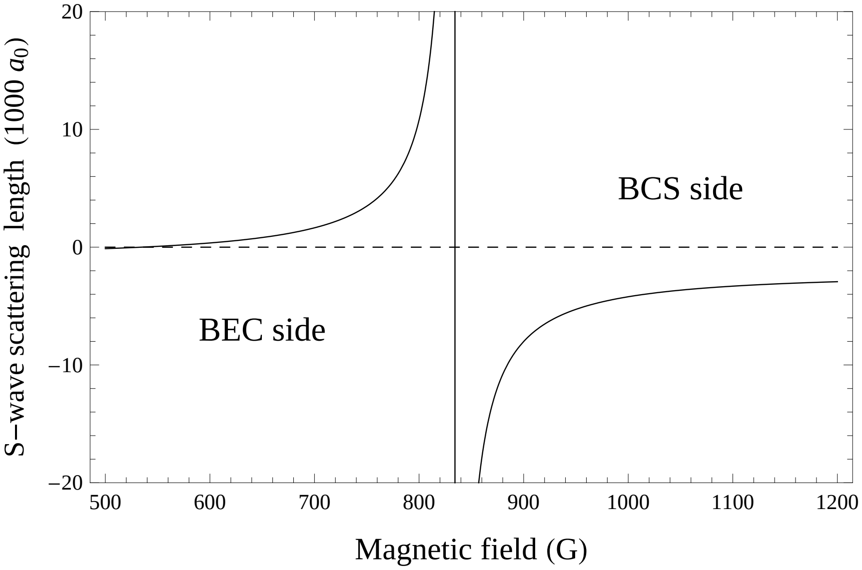

Figure 1.3: S-wave scattering length versus magnetic field for ^{6}Li (1,2) scattering channels.

The zero-energy s-wave scattering length would reach infinity on resonance as shown in Figure 1.3 [29], where interaction between atoms reaches maximum. Here I only show the ^{6}Li scattering length for hyperfine states 1 and 2 as an example. I will discuss scattering lengths for other combinations of hyperfine states in ^{6}Li later in Figure 3.2 in chapter 3.

When the magnetic field is small and the triplet scatting state is still above the singlet bound state as shown in Figure 1.2(a), atoms tend to fall into the bound state and form stable molecular dimers. Here Bose-Einstein condensation (BEC) can exist at low temperature. This corresponds to the left side of resonance in Figure 1.3 and is called the BEC side. Conversely, when the magnetic field is large enough to tune the energy of the triplet scattering state below the singlet bound state as shown in Figure 1.2(c), atoms tend to stay in the scattering state. The singlet molecular state is unstable and decays into the triplet continuum due to the hyperfine coupling. At low temperature, atoms can form weakly bound boson-like Cooper pairs and the Fermi gas turns into a superfluid. This corresponds to the right side of the resonance in Figure 1.3. Since Cooper pairs are the description given by the microscopic theory of low temperature superconductivity proposed by John Bardeen, Leon Neil Cooper, and John Robert Schrieffer(BCS), this side of the Feshbach resonance is called the BCS side.

The whole region across the Feshbach resonance is the so called BEC-BCS crossover region. The fact that the system can be tuned smoothly between a molecular dimer BEC and a BCS superfluid, which is caused by many-body effects, through the Frshbach resonance makes the BEC-BCS crossover a region of great interest.

1.2 Rf spectroscopy in Fermi gases

Radio frequency spectroscopy is the tool we use to study the quasi-2D system. In §1.2.1, I will give a short introduction of the pairing energy experiments using the radio frequency spectroscopy. I will also talk about the previous research on cold gases in reduced dimensions. In §1.2.2, I will give a brief overview of rf spectroscopy in a quasi-2D Fermi gas.

1.2.1 Previous rf spectroscopy experiments and research on ultracold gases in reduced dimensions

After the realization of degenerate strongly interacting Fermi gas, several groups searched for proof of superfluidity and looked for pairing in this system [30–33]. In 2004, the Innsbruck group directly observed the energy gap by using a radio-frequency(rf) spectroscopy method [34]. A second peak was observed beside the bare atomic resonance transition through the whole BEC-BCE crossover, which was interpreted as evidence for pairing and proof of superfluidity. Later in 2006, pairing in spin imbalanced strongly interacting Fermi gas was studied by Hulet's group [35]. In 2007, MIT group used radio frequency(rf) spectroscopy method to study the imbalanced Fermi gas [36]. They observed pairing of the minority component for both the normal and superfluid states which means the system does not need to be superfluid to have pairing as the 2004 paper claimed. They also used in situ phase-contrast imaging and the inverse Abel transformation [37] to obtain spatially resolved rf spectroscopy [38]. In their 2008 paper [39, 40], they did radio frequency(rf) transitions from a mixture of ^{6}Li hyperfine states, $|1\rangle$ and $|3\rangle$, to the final states, $|1\rangle$ and $|2\rangle$. This method avoids strong final state interactions as in the previous experiments working from the mixture of $|1\rangle$ and $|2\rangle$, since $|2\rangle$ only weakly interacts with states $|1\rangle$ and $|3\rangle$ for magnetic field near the 1-3 Feshbach resonance.

These works in three-dimensional (3D) ^{6}Li strongly interacting Fermi gas show the radio frequency(rf) spectroscopy is a powerful tool to study pairing. These experiments also raised some important problems to consider when using the radio frequency(rf) spectroscopy method, such as final state interactions and mean field shifts caused by the inhomogeneous density in the harmonic trapping potential.

On the another hand, experiments on ultracold atomic systems in reduced dimensions were motivated by finite size effects which are crucial in the physics of quantum dots [41], in studying how spontaneous emission is modified in cavities [42–44], and in understanding the properties of thin superconducting films [45].

In the solid state context, strongly interacting two-dimensional Fermi gases were studied in the cuprates, in two-dimensional electron gases in nanostructures [46], and in thin ^{3}He films [47].

Ultracold atomic systems are impurity-free and tunable. In Bose gases, 1D to 2D dimensional crossover effects had been studied experimentally in combined magnetic and optical potentials [48] as well as in optical lattices [49–51]. With tunable interactions, energy and spin composition, ultracold Fermi gases are ideally suited for exploring pairing interactions in reduced dimensions. [3, 5, 52–55]. Important questions can be studied about the role of dimensionality, finite size and many-body effects.

Our group chose a quasi-two dimensional system since it plays a pivotal role in quantum many-body physics. The restriction of motion also profoundly increases the role of fluctuations and leads to qualitatively new effects in the interaction between atoms [15, 56–61]. We focused on directly observing the pairing energy in this quasi-two dimensional system by using radio frequency(rf) spectroscopy.

Based on zero-temperature two dimensional dimer theory, two-dimensional(2D) confinement can stabilize bound dimers in the the whole BEC-BCS region [5, 57], while in free space, bound dimers exist only in the BEC regime. These dimers are called confinement induced dimers.

Experimental studies were done by several groups including our group recently. Köhl's group in Cambridge studied fermion pairing energy in nearly two-dimensional ^{6}Li Fermi gas using radio frequency(rf) spectroscopy method in optical lattice, which is formed by retro-reflected laser beam of wavelength $\lambda = 1064\,nm$ [3]. They observed the confinement induced dimer pairing energy directly. Zwierlein's group in MIT studied the evolution of ^{6}Li fermion pairing from three to two dimensions using radio frequency(rf) spectroscopy as well [55]. They also used optical lattice generated by retro-reflected beam of wavelength $\lambda = 1064\,nm$. They observe a second peak appear in the spectrum as the dimension was reduced from 3D to 2D, which corresponds to the confinement induced dimer pairing energy.

For both Fermi gases in Köhl's group and Zwierlein's group, the 2D (ideal gas) Fermi energies $E_{F\perp} = h\nu_\perp\sqrt{N}$ are very small compared with energy level spacing in the tightly confined direction $h\nu_z$, i.e. $E_{F\perp} \ll h\nu_z$, which makes the system close to pure two-dimensional. While the pairing energy observed experimentally agreed with theoretical prediction very well in Zwierlein's group, Köhl's group saw some discrepancies, which have been interpreted in terms of 2D polarons [6, 7]. In contrast, our rf spectra in BEC-BCS crossover region with $E_{F\perp} = 1.5h\nu_z$ show large discrepancies from the dimer theory in quasi-two dimensional system [4].

1.2.2 Rf spectroscopy of a quasi-2D Fermi gas

In my thesis, I study pairing in a quasi-two dimensional Fermi gas of ^{6}Li in standing wave CO$_2$ optical traps with a wavelength $\lambda = 10.6\,\mu m$ as shown in Figure 1.1. The ratio of the ideal gas transverse Fermi energy $E_{F\perp} = h\nu_\perp\sqrt{N}$ to the energy level spacing $h\nu_z$ of the tightly conning potential is held nominally constant, with $E_{F\perp} \simeq 1.5h\nu_z$. In this case, the system is not strictly 2D, but is far from 3D, as at most the first few oscillator states are relevant for many-body predictions [53].

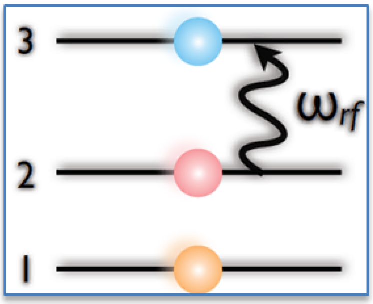

Figure 1.4: Bare-atom transition from state 2 to 3.

We work with a 50-50 mixture of ^{6}Li hyperfine states 1-2 or 1-3. Radio-frequency(rf) transitions are driven to initially empty states (for 1-2 mixture, we drive 2 to 3; for 1-3 mixture, we drive 1 to 2; for 1-3 mixture, we drive 3 to 2). The depletion of the initial occupied state is measured. We observe a two-peak rf spectra for all the transitions at low temperature, as shown in Figure 1.5. The left peak corresponds to the bare atomic transition from 2 to 3 as shown in Figure 1.4. The broader peak on the right side is caused by the binding energy of 1-2 pairing, since more energy is needed to break the pair.

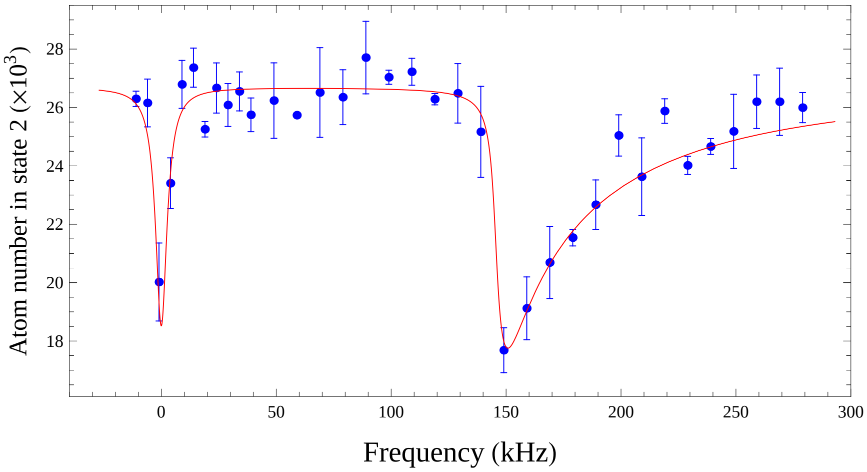

Figure 1.5: Data fitting with dimer transition theory in the BEC region. This spectrum was taken at 720G. Data are blue dots while red line is theory fitting.

The dimer binding energy E_b can be tuned by an external magnetic field. Well-below the Feshbach resonance in the molecular BEC region, $E_b \gg E_{F\perp}$. Here the dimers are small compared to the interparticle spacing. The observed spectra exhibit the expected threshold form and agree with the dimer transition theory quite well as shown in Figure 1.5.

However, around the Feshbach resonance, a large discrepancy was observed between the data and the dimer transition theory. We calculate the whole spectrum based on dimer theory, which I will discuss in detail in Chapter 3. In Figure 1.6, I show the dimer theory prediction of the rf spectrum on the top of the experimental result. We also tried to use 2D BCS theory to explain our data to include many-body effects. However, it gives the same prediction as the dimer theory [5].

When we go further in considering many-body effects, we find that the peak locations in the spectra can be described by transitions between noninteracting polaron states, i.e., an impurity atom in state 2 or in state 3, immersed in a cloud

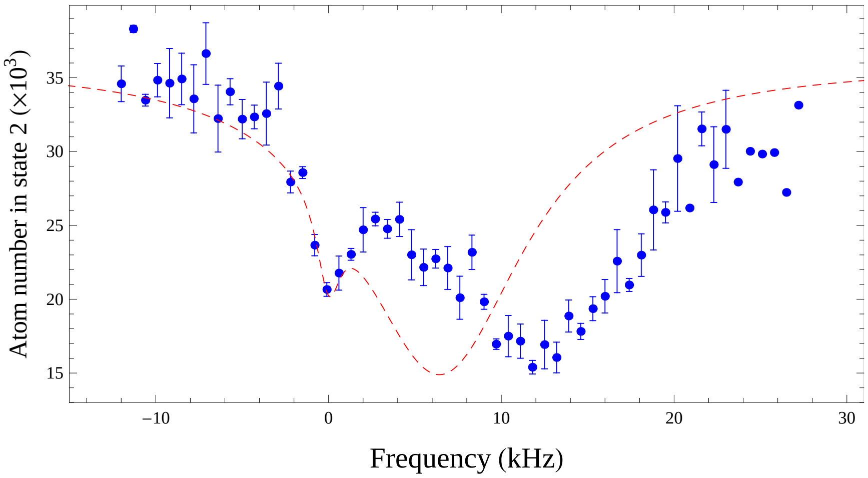

Figure 1.6: Data with dimer transition theory prediction around Feshbach resonance. This spectrum was taken at 832G. Data are blue dots while red dashed line is theory prediction.

of particle-hole pairs in state 1. In Figure 1.7, a schematic shows a 1-2 polaron to 1-3 polaron transitions. In this regime, where $E_{F\perp} > E_b$, the polaron binding energy is larger than the corresponding dimer binding energy. For the case in Figure 1.6, the 12 polaron binding energy $E_p^{12} = 24.7$ kHz, while the 12 dimer binding energy $E_b^{12} = 7.25$ kHz. The 13 polaron binding energy $E_p^{13} = 13.1$ kHz, while the 13 dimer binding energy $E_b^{13} = 0.81$ kHz. Near the Feshbach resonance, polarons are expected to be energetically more favorable than the corresponding dimers when $E_{F\perp} > E_b$ [2,61,62].

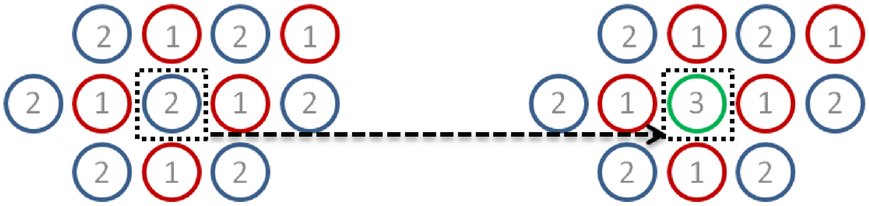

Figure 1.7: 1-2 polaron to 1-3 polaron transitions.

We believe that our experimental results exhibit many-body effects in the strongly interacting region. Our experiments have spurred several theoretical papers. Pietilä found that in the limit of weak attraction, the gas can be described in terms of effective polarons, which qualitatively explained our data. He also found a crossover from a gas of noninteracting polarons to a pseudogap regime, which qualitatively explained the differences in the experimental measurements in our group and Zwierlein's group [7]. Recently, Parish's group qualitatively explained our data showed that higher axial states can substantially modify fermion pairing. By using a modified BCS theory, they argued that our pairing experiment has already observed the effects of higher axial states [1].

For transitions starting from a 1-3 mixture, the pairing energy extracted from the spectra does not agree with the dimer transition theory in the BEC-BCS crossover. We do not fully understand all of the spectra. However, we believe the spectra contain information about new many-body effects, which requires more theoretical work.

1.3 Dissertation organization

I will introduce ^{6}Li hyperfine structure and the calculation of the radio frequency spectra using Fermi's golden rule in Chapter 2. Since wave functions for the initial and the final states of the rf transitions are required for the spectrum calculation, I will derive these wave functions first by assuming dimer transitions and then assuming polaron transitions. In Chapter 3, wave functions of the dimer bound states and the scattering states are derived. Transition frequencies and the full spectrum will be calculated to fit our data. In Chapter 4, wave function of 2D polaron states are used as the initial and final states for rf transition, and polaron transition frequencies are calculated for data fitting. In chapter 5, I briefly introduce our experimental apparatus and methods, especially the set-up for the quasi-two dimensional system. The data fits with both dimer theory and polaron theory are discussed in chapter 6. Conclusions and a summary are given in the last chapter.

Chapter 2

Radio frequency Spectroscopy

Radio frequency spectroscopy is a very powerful method to study the properties of a system. Basically, atoms are induced to jump from one energy level to another by a rf pulse with an appropriate frequency. In order to understand how atoms jump and how to extract information about the system from the rf spectroscopy experiment, we need to know the ^{6}Li hyperfine energy levels and the elementary theory of coherent rf spectroscopy for two-level systems. Based on these background knowledge, I will introduce the Rabi frequency and show how we experimentally measure it. I will also show how we accurately calibrate the magnetic field by using rf spectroscopy. Finally, using Fermi's Golden Rule I will calculate the rf transition rate between initial and final states, with which we can predict the rf spectrum and fit the experimental data.

2.1 Hyperfine Structure of ^{6}Li and Magnetic Field Calibration

Here I will calculate the hyperfine states and energies of ^{6}Li in an applied magnetic field. The ^{6}Li hyperfine structure plays an important role in the rf spectroscopy experiment, since atoms will be excited among these hyperfine states and the energy differences between these states determine what frequency we should use in the experiment.

Let us start by writing down the Hamiltonian for the ^{6}Li ground state hyperfine interactions in a magnetic field:

$$H = \frac{a_{hf}}{\hbar^2}\mathbf{S}\cdot\mathbf{I} - \frac{\mu_0}{\hbar}(g_J\mathbf{S} + g_I\mathbf{I})\cdot\mathbf{B}, \tag{2.1}$$

where the first term comes from the hyperfine interaction and the second term comes from magnetic field Zeeman shift $-\mathbf{m}\cdot\mathbf{B}$. The magnetic moment is $\mathbf{m} = \frac{\mu_0}{\hbar}(g_J\mathbf{S} + g_I\mathbf{I})$ and the bias magnetic field $\mathbf{B} = B\hat{\mathbf{e}}_z$. We use accurate parameters with the values listed below in Table 2.1:

Table 2.1: ^{6}Li hyperfine parameters and g-factors for magnetic moments in Bohr magnetons.

ground state magnetic hyperfine constant	$\frac{a_{hf}}{h} = 152.1368407 \times 10^6$ Hz
Bohr magneton	$\frac{\mu_0}{h} = 1.399624604 \times 10^6$ Hz/G
total electronic g factor	$g_J = -2.0023010$
the nuclear g factor	$g_I = 0.0004476540$

For $B = 0$, $H = \frac{a_{hf}}{\hbar^2}\mathbf{S}\cdot\mathbf{I}$. Then the total spin $\mathbf{F} = \mathbf{I} + \mathbf{S}$ is conserved: $[\mathbf{F}, \mathbf{S}\cdot\mathbf{I}] = 0$, where $S = 1/2$, $I = 1$. So, F and F_z should be good quantum numbers and we can use the $|(S,I),F,M_F\rangle$ basis, with $\mathbf{S}\cdot\mathbf{I} = \frac{1}{2}\left(\mathbf{F}^2 - \mathbf{I}^2 - \mathbf{S}^2\right)$,

$$\begin{aligned} H|(S,I),F,M_F\rangle &= E_n|(S,I),F,M_F\rangle \\ \frac{a_{hf}}{\hbar^2}\mathbf{S}\cdot\mathbf{I}|(S,I),F,M_F\rangle &= a_{hf}\frac{F(F+1) - I(I+1) - S(S+1)}{2}|(S,I),F,M_F\rangle. \end{aligned} \tag{2.2}$$

Here,

$$F = \tfrac{3}{2} \quad E_n = \tfrac{a_{hf}}{2}$$

$$F = \tfrac{1}{2} \quad E_n = -a_{hf}.$$

So, there are two F energy levels and the energy difference between them is $\frac{3}{2}a_{hf}$.

For $B \neq 0$, $H = \frac{a_{hf}}{\hbar^2}\mathbf{S} \cdot \mathbf{I} - \frac{\mu_0}{\hbar}(g_J S_z + g_I I_z)B$. We know that

$$\dot{\mathbf{F}} = \frac{i}{\hbar}[H, \mathbf{F}] = \mu \times \mathbf{B}. \tag{2.3}$$

As $\mathbf{B}$ is along the z direction, $\mu \times \mathbf{B}$ is perpendicular to the z direction. Hence,

$$\dot{F}_z = \frac{i}{\hbar}[H, F_z] = 0. \tag{2.4}$$

Therefore, for $B \neq 0$, F_z is still a good quantum number. So we will use the $|m_S, m_I\rangle$ basis, while $F_z = m_S + m_I$ is conserved. In order to work with this basis, we can write the Hamiltonian as

$$H = \frac{a_{hf}}{\hbar^2} I_z S_z - \frac{\mu_0 B}{\hbar} g_J S_z - \frac{\mu_0 B}{\hbar} g_J I_z + \frac{a_{hf}}{2\hbar^2}(I_+ S_- + I_- S_+). \tag{2.5}$$

Here, $I_\pm = I_x \pm iI_y$, $S\pm = S_x \pm iS_y$ and $I_x S_x + I_y S_y = \frac{1}{2}(I_+ S_- + I_- S_+)$. H will be block-diagonal in this basis if we order the six $|m_S, m_I\rangle$ based on the value of F_z. $\psi = \sum_i \alpha_i |m_S, m_I\rangle_i$ where $i = 1, 2, \cdots, 6$.

$$H\psi = E\psi \tag{2.6}$$

$$
\begin{pmatrix}
H_{11} & H_{12} & 0 & 0 & 0 & 0 \\
H_{21} & H_{22} & 0 & 0 & 0 & 0 \\
0 & 0 & H_{33} & H_{34} & 0 & 0 \\
0 & 0 & H_{43} & H_{44} & 0 & 0 \\
0 & 0 & 0 & 0 & H_{55} & 0 \\
0 & 0 & 0 & 0 & 0 & H_{66}
\end{pmatrix}
\begin{pmatrix} \alpha_1 \\ \alpha_2 \\ \alpha_3 \\ \alpha_4 \\ \alpha_5 \\ \alpha_6 \end{pmatrix}
= E
\begin{pmatrix} \alpha_1 \\ \alpha_2 \\ \alpha_3 \\ \alpha_4 \\ \alpha_5 \\ \alpha_6 \end{pmatrix}
\tag{2.7}
$$

This allows us to break this 6×6 matrix into two 2×2 matrixes with $F_z = \pm\frac{1}{2}$ and two simple 1×1 matrixes with $F_z = \pm\frac{3}{2}$ that are easier to solve. Let's solve them one by one.

2.1.1 Case I, $F_z = \frac{1}{2}$

When $F_z = \frac{1}{2}$, $|m_S, m_I\rangle = |\frac{1}{2}, 0\rangle$ or $|-\frac{1}{2}, 1\rangle$. Let's call them $|a\rangle$ and $|b\rangle$ respectively. Then, $|\psi\rangle = \alpha|a\rangle + \beta|b\rangle$

$$
\begin{pmatrix} H_{aa} - E & H_{ab} \\ H_{ba} & H_{bb} - E \end{pmatrix}
\begin{pmatrix} \alpha \\ \beta \end{pmatrix} = 0
\tag{2.8}
$$

$$
\begin{aligned}
H_{aa} &= \left\langle \frac{1}{2}, 0 \right| \frac{a_{hf}}{\hbar^2} I_z S_z - \frac{\mu_0 B}{\hbar} g_J S_z - \frac{\mu_0 B}{\hbar} g_I I_z \left| \frac{1}{2}, 0 \right\rangle \\
&= -\mu_0 B \frac{g_J}{2}
\end{aligned}
\tag{2.9}
$$

$$
\begin{aligned}
H_{bb} &= \left\langle -\frac{1}{2}, 1 \right| \frac{a_{hf}}{\hbar^2} I_z S_z - \frac{\mu_0 B}{\hbar} g_J S_z - \frac{\mu_0 B}{\hbar} g_I I_z \left| -\frac{1}{2}, 1 \right\rangle \\
&= -\frac{a_{hf}}{2} + \mu_0 B \frac{g_J}{2} - \mu_0 B g_I
\end{aligned}
\tag{2.10}
$$

$$\begin{aligned} H_{ab} &= \left\langle \frac{1}{2}, 0 \right| \frac{a_{hf}}{2\hbar^2} I_- S_+ \left| -\frac{1}{2}, 1 \right\rangle \\ &= \frac{a_{hf}}{2} \sqrt{(S - m_S)(S + m_S + 1)} \sqrt{(I + m_I)(I - m_I + 1)} \\ &= \frac{a_{hf}}{\sqrt{2}} = H_{ba} \end{aligned} \tag{2.11}$$

Now, use (2.9)−(2.11) in (2.8) and solve the determinant equation.

$$\left(-\mu_0 B \frac{g_J}{2} - E\right)\left(-\frac{a_{hf}}{2} + \mu_0 B \frac{g_J}{2} - \mu_0 B g_I - E\right) - \frac{a_{hf}^2}{2} = 0, \tag{2.12}$$

$$E_\pm = -\frac{1}{2}\left(\frac{a_{hf}}{2} + \mu_0 B g_I\right) \pm \frac{1}{2}\sqrt{\frac{9}{4}a_{hf}^2 + (\mu_0 B)^2(-g_J + g_I)^2 + \mu_0 B(-g_J + g_I)a_{hf}}. \tag{2.13}$$

In order to simplify the form of $E_\pm$, we define $q_0 \equiv \frac{\mu_0 B}{a_{hf}}(-g_J + g_I)$, and $Z_+ \equiv q_0 + 1/2$, $R_+ \equiv \sqrt{2 + Z_+^2}$ following the notations in paper [63], then

$$\frac{E_\pm}{a_{hf}} = -\frac{1}{4} - \frac{\mu_0 B}{2a_{hf}} g_I \pm \frac{R_+}{2}. \tag{2.14}$$

Now put $E_\pm$ back in (2.8),

$$\left(-\mu_0 B \frac{g_J}{2} - E_\pm\right)\alpha_\pm + \frac{a_{hf}}{\sqrt{2}}\beta_\pm = 0 \tag{2.15}$$

We get $\beta_\pm = -\frac{1}{\sqrt{2}}(Z_+ \mp R_+)\alpha_\pm$. Then since $|\alpha_\pm|^2 + |\beta_\pm|^2 = 1$,

$$\begin{aligned}
\alpha_- &= \frac{1}{\sqrt{1+(Z_+ + R_+)^2/2}}, \\
\beta_- &= -\frac{1}{\sqrt{2}} \frac{Z_+ + R_+}{\sqrt{1+(Z_+ + R_+)^2/2}}, \\
\alpha_+ &= \frac{1}{\sqrt{1+(Z_+ - R_+)^2/2}}, \\
\beta_+ &= \frac{1}{\sqrt{2}} \frac{R_+ - Z_+}{\sqrt{1+(R_+ - Z_+)^2/2}}. \qquad (2.16)
\end{aligned}$$

We realize $\alpha_- = \beta_+$ and $\beta_- = -\alpha_+$. If we set $\sin\theta_+ \equiv \alpha_-$ and $\cos\theta_+ \equiv -\beta_-$, we can write two eigenstates with corresponding eigenvalues $E_{caseI,1}$ and $E_{caseI,2}$ as in (2.14)

$$\psi_{caseI,1} = \sin\theta_+ \left|\frac{1}{2}, 0\right\rangle - \cos\theta_+ \left|-\frac{1}{2}, 1\right\rangle, \qquad (2.17)$$

$$\psi_{caseI,2} = \cos\theta_+ \left|\frac{1}{2}, 0\right\rangle + \sin\theta_+ \left|-\frac{1}{2}, 1\right\rangle. \qquad (2.18)$$

The definitions of $\sin\theta_+$ and $\cos\theta_+$ here are based on the principle that in high magnetic field $\cos\theta_+$ terms survive while $\sin\theta_+$ terms vanish.

2.1.2 Case II, $F_z = -\frac{1}{2}$

When $F_z = -\frac{1}{2}$, $|m_S, m_I\rangle = |\frac{1}{2}, -1\rangle$ or $|-\frac{1}{2}, 0\rangle$. Let's still call them $|a\rangle$ and $|b\rangle$ respectively for the calculation. Then, $|\psi\rangle = \alpha|a\rangle + \beta|b\rangle$. As in case I, we have

$$\begin{pmatrix} H_{aa} - E & H_{ab} \\ H_{ba} & H_{bb} - E \end{pmatrix} \begin{pmatrix} \alpha \\ \beta \end{pmatrix} = 0. \qquad (2.19)$$

$$\begin{aligned} H_{aa} &= \left\langle \frac{1}{2}, -1 \right| \frac{a_{hf}}{\hbar^2} I_z S_z - \frac{\mu_0 B}{\hbar} g_J S_z - \frac{\mu_0 B}{\hbar} g_I I_z \left| \frac{1}{2}, -1 \right\rangle \\ &= -\frac{a_{hf}}{2} - \mu_0 B \frac{g_J}{2} + \mu_0 B g_I \end{aligned} \tag{2.20}$$

$$\begin{aligned} H_{bb} &= \left\langle -\frac{1}{2}, 0 \right| \frac{a_{hf}}{\hbar^2} I_z S_z - \frac{\mu_0 B}{\hbar} g_J S_z - \frac{\mu_0 B}{\hbar} g_I I_z \left| -\frac{1}{2}, 0 \right\rangle \\ &= \mu_0 B \frac{g_J}{2} \end{aligned} \tag{2.21}$$

$$\begin{aligned} H_{ab} &= \left\langle \frac{1}{2}, -1 \right| \frac{a_{hf}}{2\hbar^2} I_- S_+ \left| -\frac{1}{2}, 0 \right\rangle \\ &= \frac{a_{hf}}{2} \sqrt{(S - m_S)(S + m_S + 1)} \sqrt{(I + m_I)(I - m_I + 1)} \\ &= \frac{a_{hf}}{\sqrt{2}} = H_{ba} \end{aligned} \tag{2.22}$$

Put (2.20)−(2.22) back in (2.19) and solve the determinant equation.

$$\left(\mu_0 B \frac{g_J}{2} - E\right) \left(-\frac{a_{hf}}{2} - \mu_0 B \frac{g_J}{2} + \mu_0 B g_I - E\right) - \frac{a_{hf}^2}{2} = 0, \tag{2.23}$$

$$E_\pm = -\frac{1}{2} \left(\frac{a_{hf}}{2} - \mu_0 B g_I\right) \pm \frac{1}{2} \sqrt{\frac{9}{4} a_{hf}^2 + (\mu_0 B)^2 (-g_J + g_I)^2 - \mu_0 B (-g_J + g_I) a_{hf}}. \tag{2.24}$$

To simplify $E_\pm$, we define $Z_- \equiv q_0 - 1/2$, $R_- \equiv \sqrt{2 + Z_-^2}$ following the notations in paper [63], then

$$\frac{E_\pm}{a_{hf}} = -\frac{1}{4} + \frac{\mu_0 B}{2 a_{hf}} g_I \pm \frac{R_-}{2}. \tag{2.25}$$

Using $E_\pm$ in (2.19),

$$\frac{a_{hf}}{\sqrt{2}} \alpha_\pm + \left(\mu_0 B \frac{g_J}{2} - E_\pm\right) \beta_\pm = 0 \tag{2.26}$$

We can get $\alpha_\pm = \frac{1}{\sqrt{2}}(Z_+ \pm R_-)\beta_\pm$. Then again we use $|\alpha_\pm|^2 + |\beta_\pm|^2 = 1$,

$$\begin{aligned}
\alpha_- &= \frac{1}{\sqrt{2}}\frac{Z_- - R_-}{\sqrt{1+(R_- - Z_-)^2/2}}, \\
\beta_- &= \frac{1}{\sqrt{1+(R_- - Z_-)^2/2}}, \\
\alpha_+ &= \frac{1}{\sqrt{2}}\frac{R_- + Z_-}{\sqrt{1+(R_- + Z_-)^2/2}}, \\
\beta_+ &= \frac{1}{\sqrt{1+(R_- + Z_-)^2/2}}. \qquad (2.27)
\end{aligned}$$

We set $\sin\theta_- \equiv \beta_+$ and $\cos\theta_- \equiv -\alpha_+$. Then we can write these two eigenstates with corresponding eigenvalues $E_{caseII,1}$ and $E_{caseII,2}$ as in (2.25)

$$\begin{aligned}
\psi_{caseII,1} &= \cos\theta_- \left|\frac{1}{2}, -1\right\rangle + \sin\theta_- \left|-\frac{1}{2}, 0\right\rangle, \qquad (2.28) \\
\psi_{caseII,2} &= -\sin\theta_- \left|\frac{1}{2}, -1\right\rangle + \cos\theta_- \left|-\frac{1}{2}, 0\right\rangle. \qquad (2.29)
\end{aligned}$$

Again, the definitions of $\sin\theta_-$ and $\cos\theta_-$ here are based on the principle that in high magnetic field $\cos\theta_-$ terms survive while $\sin\theta_-$ terms vanish.

2.1.3 Case III, $F_z = \pm\frac{3}{2}$

$F_z = \frac{3}{2}$, $|m_S, m_I\rangle = |\frac{1}{2}, 1\rangle \equiv \psi_{caseIII,1}$ and $F_z = -\frac{3}{2}$, $|m_S, m_I\rangle = |-\frac{1}{2}, -1\rangle \equiv \psi_{caseIII,2}$. Since for both of them the Hamiltonian will be simple 1×1 matrixes, then $H\psi = E\psi$.

$$\begin{aligned}
E_{caseIII,1} = E_6 &= \left\langle \frac{1}{2}, 1 \right| \frac{a_{hf}}{\hbar^2} I_z S_z - \frac{\mu_0 B}{\hbar} g_J S_z - \frac{\mu_0 B}{\hbar} g_I I_z \left| \frac{1}{2}, 1 \right\rangle \\
&= \frac{a_{hf}}{2} - \mu_0 B \frac{g_J}{2} - \mu_0 B g_I \qquad (2.30)
\end{aligned}$$

$$\begin{aligned} E_{caseIII,2} = E_3 &= \left\langle -\frac{1}{2}, -1 \middle| \frac{a_{hf}}{\hbar^2} I_z S_z - \frac{\mu_0 B}{\hbar} g_J S_z - \frac{\mu_0 B}{\hbar} g_I I_z \middle| -\frac{1}{2}, -1 \right\rangle \\ &= \frac{a_{hf}}{2} + \mu_0 B \frac{g_J}{2} + \mu_0 B g_I \end{aligned} \tag{2.31}$$

2.1.4 Summary of ^{6}Li hyperfine structure

Finally, we obtain all six eigenstates and eignevalues. If we list them in the order of eigenvalues from small to large denoted from E_1 to E_6, we have:

$$\begin{aligned}
|1\rangle = \psi_{caseI,1} &= \sin\theta_+|\tfrac{1}{2},0\rangle - \cos\theta_+|-\tfrac{1}{2},1\rangle & \tfrac{E_1}{a_{hf}} &= -\tfrac{1}{4} - \tfrac{\mu_0 B}{2a_{hf}}g_I - \tfrac{R_+}{2} \\
|2\rangle = \psi_{caseII,2} &= -\sin\theta_-|\tfrac{1}{2},-1\rangle + \cos\theta_-|-\tfrac{1}{2},0\rangle & \tfrac{E_2}{a_{hf}} &= -\tfrac{1}{4} + \tfrac{\mu_0 B}{2a_{hf}}g_I - \tfrac{R_-}{2} \\
|3\rangle = \psi_{caseIII,2} &= |-\tfrac{1}{2},-1\rangle & \tfrac{E_3}{a_{hf}} &= \tfrac{1}{2} + \tfrac{\mu_0 B}{2a_{hf}}g_J + \tfrac{\mu_0 B}{a_{hf}}g_I \\
|4\rangle = \psi_{caseII,1} &= \cos\theta_-|\tfrac{1}{2},-1\rangle + \sin\theta_-|-\tfrac{1}{2},0\rangle & \tfrac{E_4}{a_{hf}} &= -\tfrac{1}{4} + \tfrac{\mu_0 B}{2a_{hf}}g_I + \tfrac{R_-}{2} \\
|5\rangle = \psi_{caseI,2} &= \cos\theta_+|\tfrac{1}{2},0\rangle + \sin\theta_+|-\tfrac{1}{2},1\rangle & \tfrac{E_5}{a_{hf}} &= -\tfrac{1}{4} - \tfrac{\mu_0 B}{2a_{hf}}g_I + \tfrac{R_+}{2} \\
|6\rangle = \psi_{caseIII,1} &= |\tfrac{1}{2},1\rangle & \tfrac{E_6}{a_{hf}} &= \tfrac{1}{2} - \tfrac{\mu_0 B}{2a_{hf}}g_J - \tfrac{\mu_0 B}{a_{hf}}g_I.
\end{aligned}$$

Since the phase of the eigenstates can be changed for our convenience, we'd better make these eigenstates connect to the eigenstates we know when $\mathbf{B} = 0$ seamlessly.

From the beginning of this section, we know that when $\mathbf{B} = 0$, the basis is $|(S,I),F,M_F\rangle$. Now try to write $|(S,I),F,M_F\rangle$ as the combination in the basis $|m_S,m_I\rangle$ and compare with the non zero magnetic field eigenstates we obtain above when $\mathbf{B} = 0$.

$$|(S,I),F,F_z\rangle = \textstyle\sum_{m_S,m_I} |m_S,m_I\rangle\langle m_S,m_I|F,M_F\rangle$$
$$|(\tfrac{1}{2},1),\tfrac{3}{2},\tfrac{3}{2}\rangle = |\tfrac{1}{2},1\rangle = |6\rangle|_{\mathbf{B}=0}$$
$$|(\tfrac{1}{2},1),\tfrac{3}{2},\tfrac{1}{2}\rangle = \sqrt{\tfrac{1}{3}}|-\tfrac{1}{2},1\rangle + \sqrt{\tfrac{2}{3}}|\tfrac{1}{2},0\rangle = |5\rangle|_{\mathbf{B}=0}$$
$$|(\tfrac{1}{2},1),\tfrac{3}{2},-\tfrac{1}{2}\rangle = \sqrt{\tfrac{2}{3}}|-\tfrac{1}{2},0\rangle + \sqrt{\tfrac{1}{3}}|\tfrac{1}{2},-1\rangle = |4\rangle|_{\mathbf{B}=0}$$
$$|(\tfrac{1}{2},1),\tfrac{3}{2},-\tfrac{3}{2}\rangle = |-\tfrac{1}{2},-1\rangle = |3\rangle|_{\mathbf{B}=0}$$
$$|(\tfrac{1}{2},1),\tfrac{1}{2},-\tfrac{1}{2}\rangle = \sqrt{\tfrac{1}{3}}|-\tfrac{1}{2},0\rangle - \sqrt{\tfrac{2}{3}}|\tfrac{1}{2},-1\rangle = |2\rangle|_{\mathbf{B}=0}$$
$$|(\tfrac{1}{2},1),\tfrac{1}{2},\tfrac{1}{2}\rangle = \sqrt{\tfrac{2}{3}}|-\tfrac{1}{2},1\rangle - \sqrt{\tfrac{1}{3}}|\tfrac{1}{2},0\rangle = -|1\rangle|_{\mathbf{B}=0}$$

Only $|1\rangle$ has a -1 phase difference with the known engenstate at $\mathbf{B}=0$.

For large $\mathbf{B}$, $R_\pm, Z_\pm \to \infty$, $\sin\theta_\pm$ terms will vanish and $\cos\theta_\pm \to 1$, then

$$\begin{array}{lll} |6\rangle = |\tfrac{1}{2},1\rangle & |5\rangle = |\tfrac{1}{2},0\rangle & |4\rangle = |\tfrac{1}{2},-1\rangle \\ |3\rangle = |-\tfrac{1}{2},-1\rangle & |2\rangle = |-\tfrac{1}{2},0\rangle & |1\rangle = -|-\tfrac{1}{2},1\rangle \end{array}$$

Again, only $|1\rangle$ has a -1 phase difference with know engenstate $|-\frac{1}{2},1\rangle$. So, we can add a -1 phase to our $|1\rangle$ and get the ideal basis for the hyperfine structure of ^{6}Li in a magnetic field as shown in Table 2.2.

Table 2.2: Hyperfine energy eigenstates and eigen-energies.

Eigenstate	Eigen-energy
$\|1\rangle = -\sin\theta_+\|\frac{1}{2},0\rangle + \cos\theta_+\|-\frac{1}{2},1\rangle$	$\frac{E_1}{a_{hf}} = -\frac{1}{4} - \frac{\mu_0 B}{2a_{hf}}g_I - \frac{R_+}{2}$
$\|2\rangle = -\sin\theta_-\|\frac{1}{2},-1\rangle + \cos\theta_-\|-\frac{1}{2},0\rangle$	$\frac{E_2}{a_{hf}} = -\frac{1}{4} + \frac{\mu_0 B}{2a_{hf}}g_I - \frac{R_-}{2}$
$\|3\rangle = \|-\frac{1}{2},-1\rangle$	$\frac{E_3}{a_{hf}} = \frac{1}{2} + \frac{\mu_0 B}{2a_{hf}}g_J + \frac{\mu_0 B}{a_{hf}}g_I$
$\|4\rangle = \cos\theta_-\|\frac{1}{2},-1\rangle + \sin\theta_-\|-\frac{1}{2},0\rangle$	$\frac{E_4}{a_{hf}} = -\frac{1}{4} + \frac{\mu_0 B}{2a_{hf}}g_I + \frac{R_-}{2}$
$\|5\rangle = \cos\theta_+\|\frac{1}{2},0\rangle + \sin\theta_+\|-\frac{1}{2},1\rangle$	$\frac{E_5}{a_{hf}} = -\frac{1}{4} - \frac{\mu_0 B}{2a_{hf}}g_I + \frac{R_+}{2}$
$\|6\rangle = \|\frac{1}{2},1\rangle$	$\frac{E_6}{a_{hf}} = \frac{1}{2} - \frac{\mu_0 B}{2a_{hf}}g_J - \frac{\mu_0 B}{a_{hf}}g_I$

Here $\sin\theta_\pm = [1+(Z_\pm+R_\pm)^2/2]^{-1/2}$, $\cos^2\theta_\pm = 1-\sin^2\theta_\pm$, and $Z_\pm = \frac{\mu_0 B}{a_{hf}}(-g_J+g_I)\pm\frac{1}{2}$, $R_\pm = \sqrt{2+(Z_\pm)^2}$.

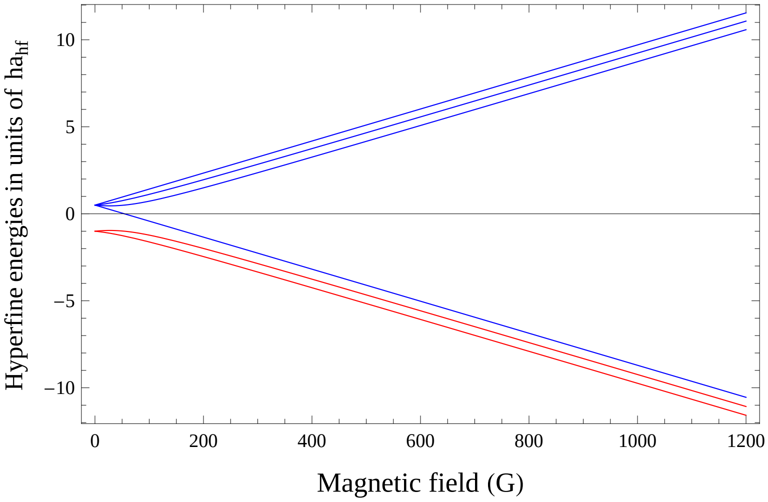

Figure 2.1: Hyperfine energies of ^{6}Li versus magnetic fields. E_1 lowest to E_6 highest.

In Figure 2.1, we can see that as magnetic field increases, the original degenerate states for both $F = \frac{3}{2}$ (blue lines) and $F = \frac{1}{2}$ (red lines) split into six different states. In the high magnetic field region the hyperfine energy shifts are approximately linear with magnetic field (about -1.4 MHz/G for the three lower states) since the Zeeman shifts will dominate compared with shifts caused by hyperfine interactions. However, the energy differences between states 1 and 2, or 2 and 3 will vary as the magnetic field changes.

Figure 2.2 shows that how the differences between energy levels change along with magnetic field in our working region(500G to 1200G). The energy differences correspond to the resonance frequencies of radio frequency (rf) pulse for the corresponding atomic transition. Since there is one to one correspondence between the magnetic field and the atomic transition frequency, we can use this property to calibrate the magnetic field in the system. If we take the derivative of the

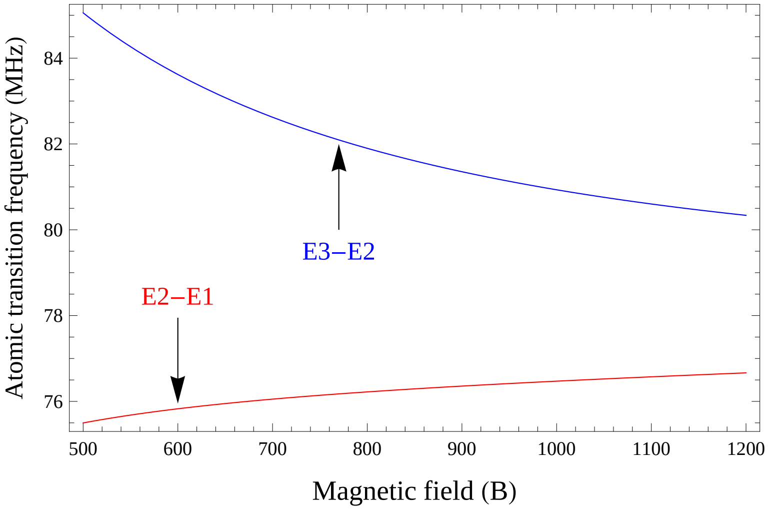

Figure 2.2: Atomic transition frequencies of ^{6}Li versus magnetic field for transition between $|1\rangle$ and $|2\rangle$, and transition between $|2\rangle$ and $|3\rangle$.

energy difference, we can get the accuracy of this calibration method as shown in Figure 2.3.

The Mathematica file that I use to accurately calculate the hyperfine energies versus magnetic field is in appendix A.

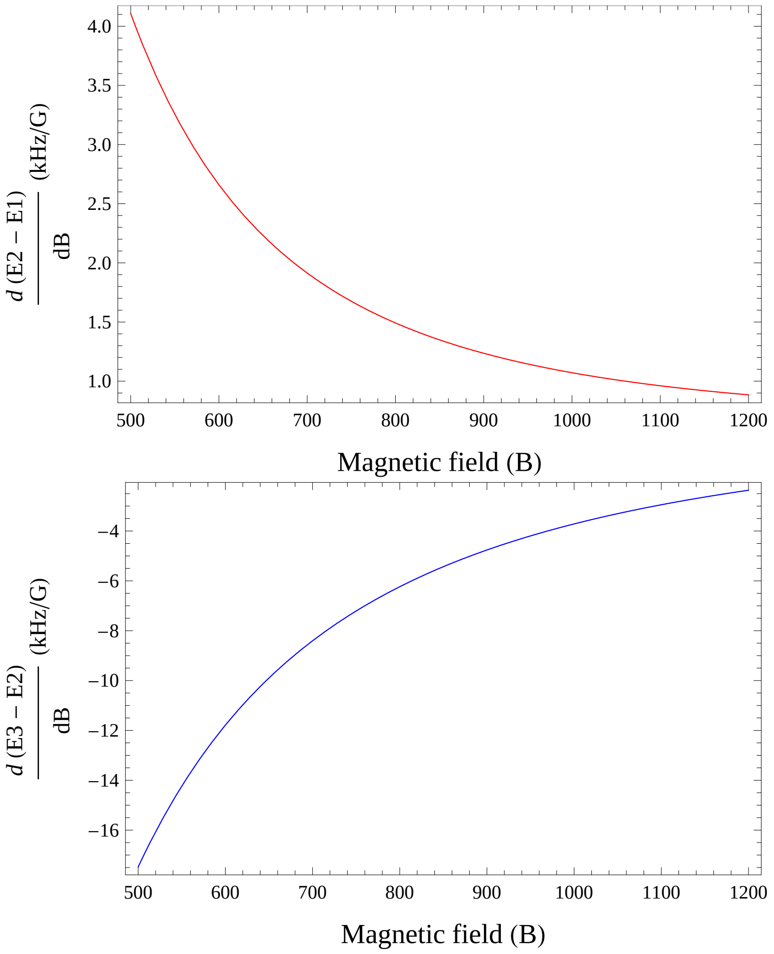

Figure 2.3: Derivative of the atomic transition frequencies of ^{6}Li versus magnetic field for transition between $|1\rangle$ and $|2\rangle$ (top), and transition between $|2\rangle$ and $|3\rangle$ (bottom).

2.2 Coherent Radio Frequency Spectroscopy

Having derived the hyperfine structure of ^{6}Li, we need to talk about the elementary theory of coherent radio frequency (rf) spectroscopy. Since this is our starting point for rf epectroscopy experiments. Here we just consider a simple two level system. We will see that this elementary theory predicts both Rabi oscillation and peak positions in the spectrum of the simple two level transition, which we use to calibrate our rf magnetic field.

Let's start by writing down the Hamiltonian of an arbitrary system with an radio frequency (rf) pulse.

$$H = H_0 + H'(t),$$
$$H_0|n\rangle = E_n|n\rangle;\; E_n = \hbar\omega_n. \tag{2.32}$$

Here $H'(t) = -\mathbf{m}\cdot\mathbf{B}_{rf}(t)$ is the magnetic dipole energy caused by the radio frequency (rf) pulse. We choose radio frequency (rf) magnetic field polarized along the x direction.

$$\mathbf{B}_{rf}(t) = \hat{\mathbf{e}}_x B^0_{rf}\cos\omega t, \tag{2.33}$$

$$\mathbf{m} = \mu_0(g_J\mathbf{S} + g_I\mathbf{I}), \tag{2.34}$$

where $\mathbf{m}$ contains both electric-spin and nuclear magnetic dipole moments. B^0_{rf} is the rf pulse amplitude and ω is the rf frequency. Since the magnetic field $\mathbf{B}$ in our system is along the z direction as I mentioned in the previous section, if the rf pulse is also along z direction, $\langle n|H'|k\rangle = \langle n| - m_z B^0_{rf}\cos\omega t|k\rangle = 0$, $M_n \neq M_k$, where $|n\rangle$ and $|k\rangle$ are ^{6}Li hyperfine states. Therefore, the rf pulse must be perpendicular to z direction to make transitions between states of different total $M = M_I + M_S$.

When we write a state in the eigenstate basis $|\psi(t)\rangle = \sum_n a_n(t)e^{-i\omega_n t}|n\rangle$ and substitute into the time-dependent Schrödinger equation

$$H|\psi(t)\rangle = i\hbar\frac{\partial}{\partial t}|\psi(t)\rangle, \tag{2.35}$$

we obtain

$$\begin{aligned}\sum_n a_n(t)e^{-i\omega_n t}(H_0+H')|n\rangle &= \sum_n (i\hbar\dot{a}_n+\hbar\omega_n a_n)e^{-i\omega_n t}|n\rangle,\\ \sum_n a_n(t)e^{-i\omega_n t}H'|n\rangle &= i\hbar\sum_n \dot{a}_n e^{-i\omega_n t}|n\rangle. \end{aligned} \tag{2.36}$$

Hitting both sides of equation (2.36) with $\langle k|$, we obtain

$$\langle k|\sum_n a_n(t)e^{-i\omega_n t}H'|n\rangle = i\hbar\sum_n \dot{a}_n e^{-i\omega_n t}\langle k|n\rangle = i\hbar\dot{a}_k e^{-i\omega_k t}, \tag{2.37}$$

$$\dot{a}_k(t) = -\frac{i}{\hbar}\sum_n e^{i\omega_{kn}t}a_n(t)H'_{kn}. \tag{2.38}$$

Here, $\omega_{kn}=\omega_k-\omega_n$, $H'_{kn}=\langle k|H'|n\rangle$. If we define the Rabi frequency Ω_{kn} by

$$\hbar\,\Omega_{kn}\equiv\langle k|m_x|n\rangle B^0_{rf}, \tag{2.39}$$

we can write (2.38) as

$$\dot{a}_k(t) = i\sum_n e^{i\omega_{kn}t}\Omega_{kn}a_n(t)\cos\omega t. \tag{2.40}$$

Later on, we will see that when the rf frequency is resonant with the two level energy splitting there is an atom number oscillation between these levels as time goes by at this Rabi frequency Ω_{kn}.

In a simple two energy level system as shown in Figure 2.4, we assume the

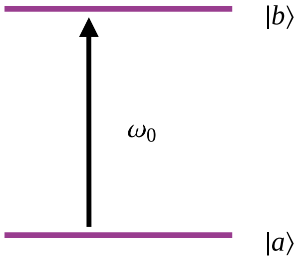

Figure 2.4: A schematic of a two energy level transition.

upper level is $|b\rangle$ and lower level is $|a\rangle$, and $\omega_b - \omega_a = \omega_0 > 0$.

$$\dot{a}(t) = \frac{i\Omega}{2} e^{-i\omega_0 t}(e^{-i\omega t} + e^{i\omega t}) b(t) \tag{2.41}$$

$$\dot{b}(t) = \frac{i\Omega}{2} e^{i\omega_0 t}(e^{-i\omega t} + e^{i\omega t}) a(t) \tag{2.42}$$

Since the terms with $e^{\pm i(\omega_0+\omega)t}$ rapidly oscillate when $\omega_0 + \omega \gg \Omega$,

$$\int_0^t dt \frac{i\Omega}{2} e^{-i(\omega_0+\omega)t} a(t) \simeq 0. \tag{2.43}$$

That means after a time integration these terms would not affect $a(t)$ or $b(t)$ too much. So, we can drop these terms by using the rotating-wave approximation and get

$$\dot{a}(t) \simeq \frac{i\Omega}{2} e^{i\Delta t} b(t) \tag{2.44}$$

$$\dot{b}(t) \simeq \frac{i\Omega}{2} e^{i\Delta t} a(t), \tag{2.45}$$

where $\Delta \equiv \omega - \omega_0$ is frequency detuning in respect to ω_0.

2.2.1 On Resonance - Rabi Oscillation

When rf frequency is on resonance, $\Delta = 0$,

$$\dot{a}(t) = \frac{i\Omega}{2}\, b(t),\, \dot{b}(t) = \frac{i\Omega}{2}\, a(t). \tag{2.46}$$

$$\ddot{a}(t) + \left(\frac{i\Omega}{2}\right)^2 a(t) = 0,\, \ddot{b}(t) + \left(\frac{i\Omega}{2}\right)^2 b(t) = 0. \tag{2.47}$$

$a(t)$, $b(t)$ should have the solution forms

$$\begin{aligned} a(t) &= A\cos\left(\frac{\Omega}{2}t\right) + B\sin\left(\frac{\Omega}{2}t\right) && (2.48)\\ b(t) &= C\cos\left(\frac{\Omega}{2}t\right) + D\sin\left(\frac{\Omega}{2}t\right). && (2.49)\end{aligned}$$

We can calculate the coefficients A, B, C, D by using the initial conditions $a(0) = 1$, $b(0) = 0$. Then, we obtain

$$a(t) = \cos\left(\frac{\Omega}{2}t\right),\, b(t) = i\sin\left(\frac{\Omega}{2}t\right) \tag{2.50}$$

$$|\,a(t)|^2 = \cos^2\left(\frac{\Omega}{2}t\right),\, |\,b(t)|^2 = \sin^2\left(\frac{\Omega}{2}t\right). \tag{2.51}$$

Here $|\,a(t)|^2 + |\,b(t)|^2 = 1$. So, there is an atom number oscillation between level a and b along the time axis at the Rabi frequency Ω.

Experimentally, we can measure the Rabi frequency in our two level system. It is an important parameter for extracting other information about the system. Let's use the two level system formed by the two lowest ^{6}Li hyperfine states 1 and 2. We start by having all the atoms in state 2. After finding the resonant rf frequency ω_0 for transition from state 2 to state 1, we record the atom number in

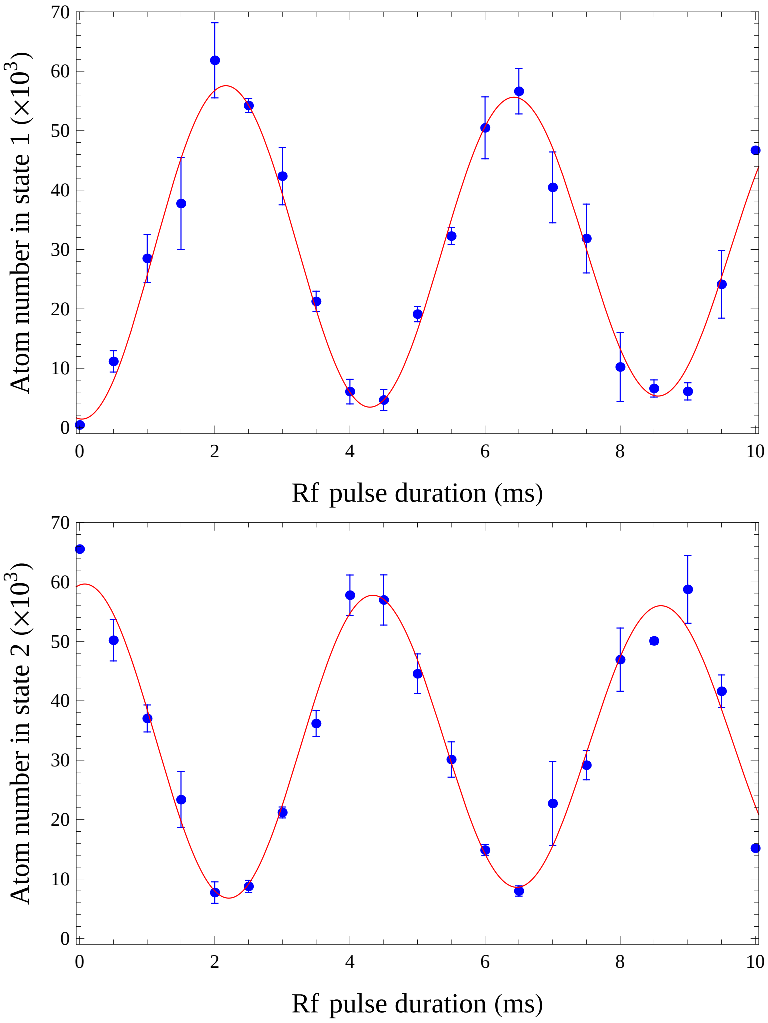

Figure 2.5: Rabi frequency oscillation at 822 G between $|1\rangle$ and $|2\rangle$. $\Omega_{21} = 2\pi \times (234.6 \pm 2.8)$ Hz

both states for different rf pulse durations. Figure 2.5 is one set of data showing how atom numbers oscillate between state 1 and 2 around 822 G. Here the Rabi frequency is about 234 Hz. Note that the number in state 1 is 180 degree out of phase with that in state 2 as it should be.

Since the Rabi frequency $\Omega_{kn} = \frac{1}{\hbar}\langle k|m_x|n\rangle B_{rf}^0$, it can be affected by both rf amplitude B_{rf}^0 and magnetic dipole matrix element $\langle k|m_x|n\rangle$. Let's calculate the magnetic dipole matrix elements for transitions among the three lowest hyperfine states of ^{6}Li and see how the applied bias magnetic field can change the Rabi frequency for transitions between them. From table 2.2, we know

$$\begin{aligned}
|1\rangle &= -\sin\theta_+|\tfrac{1}{2},0\rangle + \cos\theta_+|-\tfrac{1}{2},1\rangle \\
|2\rangle &= -\sin\theta_-|\tfrac{1}{2},-1\rangle + \cos\theta_-|-\tfrac{1}{2},0\rangle \\
|3\rangle &= |-\tfrac{1}{2},-1\rangle.
\end{aligned}$$

Since $m_x = (g_J\mu_0 S_x + g_I\mu_0 I_x)/\hbar$ and $|g_I|$ is very small compared with $|g_J|$, we can ignore the second term, $m_x \simeq g_J\mu_0 S_x/\hbar \simeq -2\mu_0\frac{S_+ + S_-}{2\hbar}$.

$$\begin{aligned}
\langle 2|m_x|1\rangle &= -\tfrac{\mu_0}{\hbar}\langle -\tfrac{1}{2},0|S_-|\tfrac{1}{2},0\rangle(-\cos\theta_-\sin\theta_+) = \mu_0\cos\theta_-\sin\theta_+ \\
\langle 3|m_x|2\rangle &= -\tfrac{\mu_0}{\hbar}\langle -\tfrac{1}{2},-1|S_-|\tfrac{1}{2},-1\rangle(-\sin\theta_-) = \mu_0\sin\theta_- \\
\langle 3|m_x|1\rangle &= 0.
\end{aligned}$$

So, rf transitions can only happen between states 1 and 2 or between states 2 and 3 with Rabi frequencies

$$\begin{aligned}
\Omega_{21} &= \frac{\mu_0 B_{rf}^0}{\hbar}\cos\theta_-\sin\theta_+ \\
\Omega_{32} &= \frac{\mu_0 B_{rf}^0}{\hbar}\sin\theta_-. \qquad (2.52)
\end{aligned}$$

Here $\sin\theta_\pm = [1 + (Z_\pm + R_\pm)^2/2]^{-1/2}$, $\cos^2\theta_\pm = 1 - \sin^2\theta_\pm$, and $Z_\pm = \frac{\mu_0 B}{a_{hf}}(-g_J + g_I) \pm \frac{1}{2}$, $R_\pm = \sqrt{2 + (Z_\pm)^2}$. For $\mathbf{B} = 0$, $\Omega_{21} = \frac{1}{3}\frac{\mu_0 B_{rf}^0}{\hbar}$ and $\Omega_{32} = \frac{2}{3}\frac{\mu_0 B_{rf}^0}{\hbar}$.

When the magnetic field is high enough that $B > a_{hf}/\mu_0 \simeq 152/1.4 = 108$ G, as in the region we use, from 500 G to 1200 G, $Z_\pm = 1.84 \times 10^{-2} \times B \pm \frac{1}{2} \simeq 1.84 \times 10^{-2} \times B$, $R_\pm \simeq Z_\pm$ and $\sin\theta_\pm \simeq [(Z_\pm + Z_\pm)^2/2]^{-1/2} = 1/(\sqrt{2}Z_\pm)$, $\cos\theta_\pm \simeq 1$. Hence,

$$\Omega_{32} = \Omega_{21} = \frac{\mu_0 B_{rf}^0}{\sqrt{2}\,\hbar} \frac{1}{1.84 \times 10^{-2} \times B}. \tag{2.53}$$

These two Rabi frequencies should be inversely proportional to the bias magnetic field **B**. We can calculate the ratio of the Rabi frequencies for different magnetic fields based on this relation. Figure 2.6 shows another Rabi frequency measurement at 526 G for the same transition between states 1 and 2 with same rf amplitude B_{rf}^0 as in Figure 2.5 where $B = 822$ G. Here the Rabi frequency is about 363 Hz. Compared with data from Figure 2.5, we have:

$$\begin{aligned} \left(\frac{\Omega_{822\mathrm{G}}}{\Omega_{526\mathrm{G}}}\right)_{measure} &= \frac{234.6 \text{ Hz}}{363.3 \text{ Hz}} = 0.646 \\ \left(\frac{\Omega_{822\mathrm{G}}}{\Omega_{526\mathrm{G}}}\right)_{calculate} &= \frac{526 \text{ G}}{822 \text{ G}} = 0.640. \end{aligned} \tag{2.54}$$

Hence, the measured ratio is in very good agreement with the calculated value,

$$\left(\frac{\Omega_{822\mathrm{G}}}{\Omega_{526\mathrm{G}}}\right)_{measure} \simeq \left(\frac{\Omega_{822\mathrm{G}}}{\Omega_{526\mathrm{G}}}\right)_{calculate}.$$

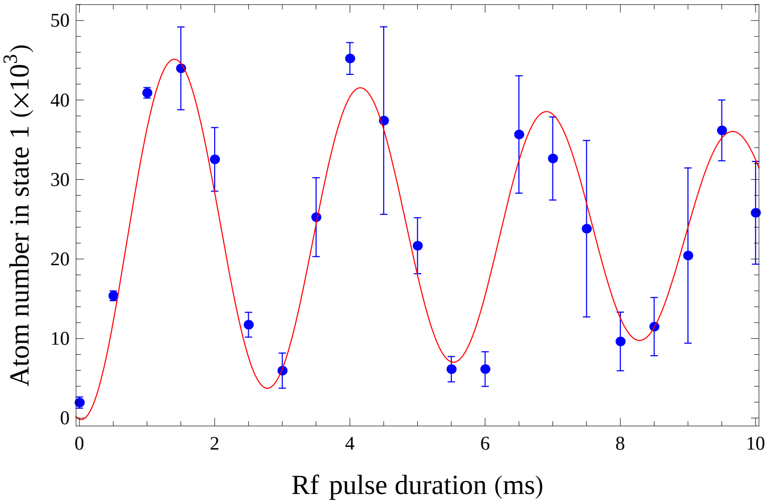

Figure 2.6: Rabi frequency oscillation at 526 G between $|1\rangle$ and $|2\rangle$. $\Omega_{21} = 2\pi \times (363.3 \pm 4.5)$ Hz

2.2.2 Lineshape for coherent Excitation

When there is detuning $\Delta \neq 0$, from equations (2.45) we have

$$\ddot{a}(t) - i\Delta\dot{a} + \left(\frac{\Delta}{2}\right)^2 a = 0 \qquad (2.55)$$

$$\ddot{b}(t) - i\Delta\dot{b} + \left(\frac{\Delta}{2}\right)^2 b = 0. \qquad (2.56)$$

If we assume

$$a \sim e^{i\delta t},\ b \sim e^{-i\delta t}, \qquad (2.57)$$

we get $\delta^2 - \Delta\delta - (\frac{\Omega}{2})^2 = 0$ which gives us $\delta = \frac{\Delta}{2} \pm \frac{1}{2}\sqrt{\Delta^2 + \Omega^2} \equiv \frac{\Delta}{2} \pm \frac{\Omega'}{2}$. Here, $\Omega' = \sqrt{\Delta^2 + \Omega^2}$. Then we can write $a(t)$ and $b(t)$ as

$$a(t) = e^{i\frac{\Delta}{2}t}(Ae^{\frac{i}{2}\Omega' t} + Be^{-\frac{i}{2}\Omega' t}), \qquad (2.58)$$

$$b(t) = e^{-i\frac{\Delta}{2}t}(Ce^{\frac{i}{2}\Omega' t} + De^{-\frac{i}{2}\Omega' t}). \qquad (2.59)$$

As in the no detuning case, we also can calculate the coefficients A, B, C, D by using the initial condition $a(0) = 1$, $b(0) = 0$. Then we obtain

$$
\begin{aligned}
a(t) &= e^{i\frac{\Delta}{2}t}\left[\cos\left(\frac{\Omega' t}{2}\right) - i\frac{\Delta}{\Omega'}\sin\left(\frac{\Omega' t}{2}\right)\right] && (2.60)\\
b(t) &= i\frac{\Omega}{\Omega'}e^{-i\Delta t}\sin\frac{\Omega' t}{2}. && (2.61)
\end{aligned}
$$

$$
\begin{aligned}
|\,a(t)|^2 &= \cos^2\left(\frac{\Omega' t}{2}\right) + \frac{\Delta^2}{\Omega'^2}\sin^2\left(\frac{\Omega' t}{2}\right) && (2.62)\\
|\,b(t)|^2 &= \frac{\Omega^2}{\Omega'^2}\sin^2\left(\frac{\Omega' t}{2}\right). && (2.63)
\end{aligned}
$$

We also have $|\,a(t)|^2 + |\,b(t)|^2 = 1$.

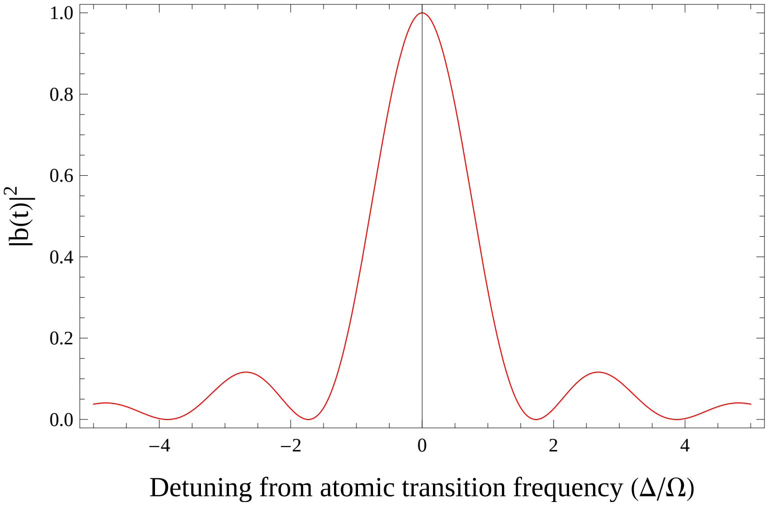

Figure 2.7: Rf transition fraction versus frequency detuning from the bare atomic transition.

If we plot $|b(t)|^2 = \frac{1}{1+\frac{\Delta^2}{\Omega^2}}\sin^2\left(\sqrt{1+\frac{\Delta^2}{\Omega^2}}\frac{\Omega t}{2}\right)$ with respect to the dimensionless detuning Δ/Ω, when $\Omega t = \pi$ which corresponds to the full transition of atoms from $|a\rangle$ to $|b\rangle$, we can see a obvious peak around 0. This tells us that we have the maximum transition when rf frequency is on resonance and how the transition probability decreases with detuning, as in Figure 2.7. This is the basic principle of the rf spectroscopy experiment.

However, in our real experiment, the system works in the non-coherent region. We can not observe the exact shape of the transition peak as in Figure 2.7 with a π pulse. But we still can see a quite narrow peak at zero detuning as in Figure 2.8 by using a relatively large Ωt which is about 15 times of π.

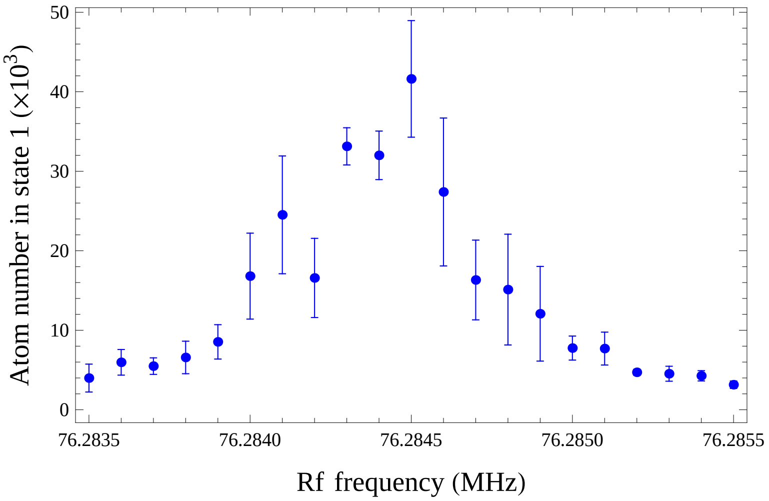

Figure 2.8: Atomic transition spectrum from pure state 2 to state 1 at 844.2 G (76.2846 MHz).

So, on the one hand, experimentally we can find the transition rf frequency quite accurately from the spectrum, while on the other hand we have the accurate relation between magnetic field and the transition rf frequency. That makes rf spectroscopy a perfect way to be used to calibrate the magnetic field.

2.3 Calculation of Rf transition spectrum using Fermi's golden rule

As I mentioned in the end of last section, our real system is not coherent. In order to calculate the rf transition rate and obtain the rf spectrum, we need to use Fermi's golden rule.

A simple golden rule calculation gives the radio-frequency-induced transition rate out of the initial state to all possible final states

$$R_i(\omega_{rf}) = \sum_f R_{f\leftarrow i}, \tag{2.64}$$

where ω_{rf} is the rf frequency, and

$$\begin{aligned}
R_{f\leftarrow i} &= \frac{2\pi}{\hbar}|\tilde{H}'_{fi}|^2\,\delta(E_f - E_i - \hbar\omega_{rf}) \\
\tilde{H}'_{fi} &= \langle f|\tilde{H}'|i\rangle \\
H' &\equiv \tilde{H}'_{32}|3\rangle\langle 2|\,e^{-i\omega_{rf}t} + h.c. \\
&= -\frac{\hbar\Omega_{32}}{2}|3\rangle\langle 2|\,e^{-i\omega_{rf}t} - \frac{\hbar\Omega_{32}}{2}|2\rangle\langle 3|\,e^{i\omega_{rf}t}
\end{aligned} \tag{2.65}$$

Here, $\langle f|\tilde{H}'|i\rangle$ is the matrix element of the rf perturbation between the final and initial states. We assume the initial hyperfine state for the atom pair is $|1\rangle|2\rangle$ and final state is pair state $|1\rangle|3\rangle$. Ω_{32} is the Rabi frequency for changing the hyperfine state of a single atom from the chosen populated state 2 to the initially unpopulated state 3. In equation (2.65), H' is written in the rotating wave approximation. Only the first term can cause the transition we require.

We can write the wave-function of the initial and final states as

$$\begin{aligned} |i\rangle &= \frac{1}{\sqrt{2}}(|1\rangle_a|2\rangle_b - |1\rangle_b|2\rangle_a)|I\rangle, \\ |f\rangle &= \frac{1}{\sqrt{2}}(|1\rangle_a|3\rangle_b - |1\rangle_b|3\rangle_a)|F\rangle. \end{aligned} \tag{2.66}$$

Here the atom-pair hyperfine state is anti-symmetric and the relative motion states(bound or scattering) that are denoted as $|I\rangle$ and $|F\rangle$ are symmetric in the interchange of atoms a and b. For hyperfine state part the notations are consistent with what I used in section 2.1 and subscripts a, b denotes different atoms. Then the matrix element is

$$\begin{aligned} \tilde{H}'_{fi} &= -\frac{\hbar\,\Omega_{32}}{4}\left({}_a\langle 1|_b\langle 3| -_b \langle 1|_a\langle 3|\right)\left(|3\rangle_{aa}\langle 2| + |3\rangle_{bb}\langle 2|\right)\left(|1\rangle_a|2\rangle_b - |1\rangle_b|2\rangle_a\right)\langle F|I\rangle \\ &= -\frac{\hbar\,\Omega_{32}}{4}\left[{}_a\langle 1|_b\langle 3|(|3\rangle_{bb}\langle 2|)|1\rangle_a|2\rangle_b + (-1)^2_a\langle 3|_b\langle 1|(|3\rangle_{aa}\langle 2|)|2\rangle_a|1\rangle_b\right]\langle F|I\rangle \\ &= -\frac{\hbar\,\Omega_{32}}{2}\langle F|I\rangle. \end{aligned} \tag{2.67}$$

Since the center of mass energy does not change in the rf transition, $E_f - E_i$ is the total change in the atomic hyperfine energy ($\equiv \hbar\omega_{fi}$) plus the change in the energy of the relative motion of the pair $E_F - E_I$. We sum up all the final states to get the total rate out of initial state

$$R_i = \frac{2\pi}{\hbar}\sum_f |H'_{fi}|^2\delta(E_f - E_i - \hbar\omega_{rf}). \tag{2.68}$$

Then,

$$\begin{aligned}\int_0^\infty d\omega_{rf}\,R_i(\omega_{rf}) &= \frac{2\pi}{\hbar}\sum_f |H'_{fi}|^2 \int_0^\infty d\omega_{rf}\,\delta(E_f - E_i - \hbar\omega_{rf}) \\ &= \frac{2\pi}{\hbar^2}\left(\frac{\hbar\Omega_{32}}{2}\right)^2 \sum_F |\langle F|I\rangle|^2. \end{aligned} \tag{2.69}$$

From the completeness of final relative motion states, which contain scattering and bound states, $\sum_F |F\rangle\langle F| = 1$, we have $\sum_F \langle I|F\rangle\langle F|I\rangle = \langle I|I\rangle = 1$ and the total rate out of $|i\rangle$ is just

$$\int_0^\infty d\omega_{rf}\,R_i(\omega_{rf}) = \frac{\pi}{2}\Omega_{32}^2 \tag{2.70}$$

We can define a normalized transition rate $I(\omega)$ where

$$R_i(\omega_{rf}) = \frac{\pi}{2}\Omega_{fi}^2\,I(\omega_{rf}) \tag{2.71}$$

$$\int_0^\infty d\omega_{rf} I(\omega_{rf}) = 1 \tag{2.72}$$

If we define

$$\omega_{rf} = \omega_{fi} + \omega, \tag{2.73}$$

with ω the frequency relative to the (unshifted) free-atom hyperfine transition frequency ω_{fi}, we can write $I(\omega)$ as,

$$I(\omega) = \sum_F |\langle F|I\rangle|^2\,\hbar\,\delta(E_F - E_I - \hbar\omega), \tag{2.74}$$

$$\text{and,} \qquad \int_{-\infty}^{\infty} d\omega I(\omega) = 1. \tag{2.75}$$

This normalized transition rate is a concise form compared with $R_i(\omega_{rf})$. In order to calculate the transition rates, we need to find wave functions of $|F\rangle$ and $|I\rangle$. They can be either bound state and scattering state of dimers or polarons.

Chapter 3

Theory of Confinement-induced Dimers

In §2.3, I derived the rf transition rate by using Fermi's golden rule. In the equation (2.75), wave function forms of the initial and final states are required to calculate the rf transition rate. In this chapter, I will consider dimer theory and use dimer bound state or scatting state to be the initial and final states of the rf transition. The transition spectrum can be predicted and will be used to compare with experimental spectrum in Chapter 6.

In two dimensional systems, atom-pairs exist not only on the BEC side of the Feshbach resonance as in three dimensions, but also can be stabilized in the BCS region. This is caused by the confinement of the two dimensional geometry [5,57]. We call these atom-pairs confinement-induced dimers. Our initial motivation to do the radio frequency spectroscopy experiments was to directly observe the binding energy of this kind of confinement induced dimer. Since our system is quasi-two dimensional, we also expect difference from two dimensional system.

First, I will solve the Schrödinger equation for a harmonically-trapped two atom system by using a time-dependent Green's function. Then I obtain the stationary Green's function and calculate the dimer binding energies. At last, the wave function forms for the bound state and scattering state will be calculated.

3.1 Green's function solution of the time dependent Schrödinger equation

In order to calculate the dimer binding energies and dimer wave functions, first we need to write down the Hamiltonian of the system and solve the Schrödinger equation. Here we will use a Green's function method to solve the Schrödinger equation.

For the Hamiltonian, we write the kinetic and potential energy of a two-atom system in a three dimensional harmonic trap:

$$H^{(0)} = \frac{\mathbf{p}_1^2}{2m} + \frac{\mathbf{p}_2^2}{2m} + \frac{1}{2}m\omega_x^2 x_1^2 + \frac{1}{2}m\omega_x^2 x_2^2 + \frac{1}{2}m\omega_y^2 y_1^2 + \frac{1}{2}m\omega_y^2 y_2^2 + \frac{1}{2}m\omega_z^2 z_1^2 + \frac{1}{2}m\omega_z^2 z_2^2. \tag{3.1}$$

$H^{(0)}$ can be separated into two parts for the center-of-mass motion and the relative motion:

$$\begin{aligned} H^{(0)} &= \left(\frac{\mathbf{P}^2}{2M} + \frac{1}{2}M\omega_x^2 X^2 + \frac{1}{2}M\omega_y^2 Y^2 + \frac{1}{2}M\omega_z^2 Z^2\right) \\ &\quad + \left(\frac{\mathbf{p}^2}{2\mu} + \frac{1}{2}\mu\omega_x^2 x^2 + \frac{1}{2}\mu\omega_y^2 y^2 + \frac{1}{2}\mu\omega_z^2 z^2\right). \end{aligned} \tag{3.2}$$

Here, $Z = \frac{z_1+z_2}{2}$, $\quad z = z_1 - z_2$, and similarly for x, y direction, $M = 2m$, $\mu = m/2$.

Since the center-of-mass motion energy does not change in the rf transition, only the relative motion part of $H^{(0)}$ needs to be considered, which defined as:

$$H_0 = \frac{\mathbf{p}^2}{2\mu} + \frac{1}{2}\mu\omega_x^2 x^2 + \frac{1}{2}\mu\omega_y^2 y^2 + \frac{1}{2}\mu\omega_z^2 z^2. \tag{3.3}$$

We use pseudo-potential form to describe the short-range s-wave interaction between two atoms [64]

$$V(\mathbf{r})\psi(\mathbf{r}) = \frac{4\pi\hbar^2 a}{m}\,\delta(\mathbf{r})\frac{\partial}{\partial r}[r\psi(\mathbf{r})], \tag{3.4}$$

where $\mathbf{r} = \mathbf{r_1} - \mathbf{r_2}$ and a is the zero-energy s-wave scattering length.

Then the total Hamiltonian for the relative motion of two-atom system is

$$H_{\mathbf{r}} = H_0 + V(\mathbf{r}). \tag{3.5}$$

The next step is to solve the Schrödinger equation. We notice that if we are using a Green's function method to solve the Schrödinger equation, the stationary Green's function is readily determined from the time-dependent Green's function for harmonic confinement. In order to use a time-dependent Green's function, we consider the time-dependent Schrödinger equation

$$[H_0 + V(\mathbf{r})]\,\psi(\mathbf{r},t) = i\hbar\frac{\partial}{\partial t}\psi(\mathbf{r},t), \tag{3.6}$$

or

$$\left[H_0 - i\hbar\frac{\partial}{\partial t}\right]\psi(\mathbf{r},t) = -V(\mathbf{r})\psi(\mathbf{r},t). \tag{3.7}$$

To solve this, we use a time dependent Green's function

$$\left[H_0 - i\hbar\frac{\partial}{\partial t}\right]G(\mathbf{r},\mathbf{r}',t-t') = \delta(t-t')\delta(\mathbf{r}-\mathbf{r}'). \tag{3.8}$$

Then, the solution to equation (3.7) is

$$\psi(\mathbf{r},t) = \psi^{(0)}(\mathbf{r},t) - \int_{-\infty}^{\infty}dt'\int d^3\mathbf{r}'G(\mathbf{r},\mathbf{r}',t-t')V(\mathbf{r}')\psi(\mathbf{r}',t') \tag{3.9}$$

Here, $[H_0 - i\hbar\frac{\partial}{\partial t}]\psi^{(0)}(\mathbf{r},t) = 0$, i.e., $\psi^{(0)}(\mathbf{r},t)$ is the homogeneous solution.

Then, the only thing we need to do is to get the specific form of the Green's function and put it back in equation (3.9).

To obtain a causal Green's function, we add a small decay term ϵ, and solve for the Green's function using

$$\left[H_0(\mathbf{r}) - i\hbar\frac{\partial}{\partial t} - i\hbar\epsilon\right] G(\mathbf{r},\mathbf{r}',t-t') = \delta(t-t')\delta(\mathbf{r}-\mathbf{r}'). \tag{3.10}$$

Since

$$G(\mathbf{r},\mathbf{r}',t-t') = \int_{-\infty}^{\infty} d\omega\, \tilde{G}(\omega,\mathbf{r},\mathbf{r}')\frac{e^{i\omega(t-t')}}{2\pi}, \tag{3.11}$$

Put (3.13) in to (3.10), we have,

$$[H_0(\mathbf{r}) + \hbar\omega - i\hbar\epsilon]\, \tilde{G}(\omega,\mathbf{r},\mathbf{r}') = \delta(\mathbf{r}-\mathbf{r}'), \tag{3.12}$$

$$G(\mathbf{r},\mathbf{r}',t-t') = \int_{-\infty}^{\infty} \frac{d\omega}{2\pi} \frac{e^{i\omega(t-t')}}{H_0 + \hbar\omega - i\hbar\epsilon}\delta(\mathbf{r}-\mathbf{r}'). \tag{3.13}$$

A formal solution for the causal $G(\mathbf{r},\mathbf{r}',t-t')$ can be obtained by doing residue calculus in the complex upper half plane, which is required for convergence when $t > t'$,

$$G(\mathbf{r},\mathbf{r}',t-t') = \frac{2\pi i}{2\pi} \cdot \frac{\omega + \frac{1}{\hbar}H_0 - i\epsilon}{H_0 + \hbar\omega - i\hbar\epsilon} e^{-\frac{i}{\hbar}H_0(\mathbf{r})(t-t')}\delta(\mathbf{r}-\mathbf{r}'). \tag{3.14}$$

For $t < t'$, the lower half plane is required, where there is no pole. Then letting $\epsilon \to 0$, we obtain the causal Green's function

$$G(\mathbf{r},\mathbf{r}',t-t') = \frac{i}{\hbar}\theta(t-t')e^{-\frac{i}{\hbar}H_0(\mathbf{r})(t-t')}\delta(\mathbf{r}-\mathbf{r}'), \tag{3.15}$$

where $\theta(t-t')$ enforces causality and $H_0(\mathbf{r})$ operates on $\delta(\mathbf{r}-\mathbf{r}')$. Since $\delta(\mathbf{r}-\mathbf{r}') = \sum_r \phi_n(\mathbf{r})\phi_n(\mathbf{r}')$, and $H_0(\mathbf{r})\phi_n = E_n\phi_n$, we can write,

$$G(\mathbf{r},\mathbf{r}',t-t') = \frac{i}{\hbar}\theta(t-t')\sum_n e^{-\frac{i}{\hbar}E_n(t-t')}\phi_n(\mathbf{r})\phi_n^*(\mathbf{r}'). \tag{3.16}$$

We notice that the Green's function is symmetric in exchange of $\mathbf{r} \leftrightarrow \mathbf{r}'$. This is an important property we will use later to obtain the correct form of the Green's function.

We can write the Green's function as,

$$G(\mathbf{r},\mathbf{r}',\tau) \equiv \frac{i}{\hbar}\theta(\tau)g(\mathbf{r},\mathbf{r}',\tau). \tag{3.17}$$

$$g(\mathbf{r},\mathbf{r}',\tau) = e^{-\frac{i}{\hbar}H_0(\mathbf{r})\tau}\delta(\mathbf{r}-\mathbf{r}') \tag{3.18}$$

Here $\tau = t - t'$, and $g(\mathbf{r},\mathbf{r}',\tau)$ is the time translation operator in position representation.

Now we can use the Heisenberg operator

$$\mathbf{r}_H(\tau) = e^{\frac{i}{\hbar}H_0(\mathbf{r})\tau}\mathbf{r}e^{-\frac{i}{\hbar}H_0(\mathbf{r})\tau} \tag{3.19}$$

to operate on $g(\mathbf{r},\mathbf{r}',\tau)$ and by solving the form of $\mathbf{r}_H(\tau)$ to calculate the form of $g(\mathbf{r},\mathbf{r}',\tau)$. First, we find the derivative of $\mathbf{r}_H(\tau)$ with respect to τ,

$$\dot{\mathbf{r}}_H(\tau) = e^{\frac{i}{\hbar}H_0(\mathbf{r})\tau}\frac{\mathbf{p}}{\mu}e^{-\frac{i}{\hbar}H_0(\mathbf{r})\tau}. \tag{3.20}$$

Then, we take the derivative again. In the z direction,

$$\begin{aligned}\ddot{\mathbf{z}}_H(\tau) &= e^{\frac{i}{\hbar}H_0(\mathbf{r})\tau}\frac{i}{\hbar}\left[\frac{1}{2}\mu\omega_z^2 z^2, \frac{p_z}{\mu}\right]e^{-\frac{i}{\hbar}H_0(\mathbf{r})\tau} \\ &= -\omega_z^2\mathbf{z}_H(\tau). \end{aligned} \tag{3.21}$$

Since the initial conditions are $\mathbf{z}_H(0) = z$ and $\dot{\mathbf{z}}_H(0) = \frac{p_z}{\mu}$, we have

$$\mathbf{z}_H(\tau) = z\cos(\omega_z\tau) + \frac{p_z}{\mu\omega_z}\sin(\omega_z\tau). \tag{3.22}$$

Similar relations hold for the x and y directions.

Now, we see

$$\mathbf{r}_H(-\tau)g(\mathbf{r},\mathbf{r}',\tau) = \mathbf{r}'g(\mathbf{r},\mathbf{r}',\tau). \tag{3.23}$$

Hence, with $\theta_i = \omega_i\tau$; $i = x, y, z$; $g = g_x(x,x')g_y(y,y')g_z(z,z')$, we obtain for the z direction:

$$\left(cos\theta_z z - \frac{sin\theta_z}{\mu\omega_z}\frac{\hbar}{i}\frac{\partial}{\partial z}\right)g_z(z,z',\tau) = z'g_z(z,z',\tau). \tag{3.24}$$

Hence, we have

$$g_z(z,z',\tau) = C_z e^{\frac{i}{\hbar}\frac{\mu\omega_z}{sin\theta_z}(cos\theta_z\frac{z^2}{2} - zz')}, \tag{3.25}$$

where C_z is a constant. Because the Green's function is symmetric in $z \leftrightarrow z'$ as we mentioned previously, we should write $g_z(z,z',\tau)$ in a symmetric form:

$$g_z(z,z',\tau) = C_z e^{\frac{i}{\hbar}\frac{\mu\omega_z}{sin\theta_z}(cos\theta_z\frac{z^2+z'^2}{2} - zz')}. \tag{3.26}$$

Since $\int d^3\mathbf{r} g^*(\mathbf{r}, \mathbf{r_2}, \tau) g(\mathbf{r}, \mathbf{r_1}, \tau) = \delta(\mathbf{r_2} - \mathbf{r_1})$, we have in the z direction,

$$\begin{aligned}
& \int_{-\infty}^{\infty} dz g_z^*(z, z_2, \tau) g_z(z, z_1, \tau) \\
= & \int_{-\infty}^{\infty} dz C_z^* e^{-\frac{i}{\hbar}\frac{\mu\omega_z}{\sin\theta_z}(\cos\theta_z \frac{z_2^2+z^2}{2} - z_2 z)} C_z e^{\frac{i}{\hbar}\frac{\mu\omega_z}{\sin\theta_z}(\cos\theta_z \frac{z^2+z_1^2}{2} - z_1 z)} \\
= & |C_z|^2 \int_{-\infty}^{\infty} dz e^{\frac{i}{\hbar}\frac{\mu\omega_z \cos\theta_z}{\sin\theta_z}\frac{z_1^2-z_2^2}{2}} e^{\frac{i\mu\omega_z}{\hbar\sin\theta_z}(z_2-z_1)z} \\
= & |C_z|^2 e^{\frac{i}{\hbar}\frac{\mu\omega_z \cos\theta_z}{\sin\theta_z}\frac{z_1^2-z_2^2}{2}} 2\pi\hbar \frac{\sin\theta_z}{\mu\omega_z} \delta(z_2 - z_1) \\
= & \delta(z_2 - z_1). \qquad (3.27)
\end{aligned}$$

Hence we obtain $|C_z| = \sqrt{\frac{\mu\omega_z}{2\pi sin\theta_z \hbar}}$. Then by using $\int_{-\infty}^{\infty} dz g_z(z, z', 0) = 1$, from equation (3.26) we calculate the phase of C_z. If we write $C_z = |C_z| e^{i\phi_z}$,

$$\int_{-\infty}^{\infty} dz g_z(z, z', 0) = \int_{-\infty}^{\infty} \frac{du}{\sqrt{\pi}} e^{iu^2} e^{i\phi_z} = 1, \qquad (3.28)$$

where $u = \sqrt{\frac{\mu\omega_z}{2\sin\theta_z\hbar}}(z - z')$. Since $\int_{-\infty}^{\infty} \frac{du}{\sqrt{\pi}} e^{iu^2} = \sqrt{i}$, $e^{i\phi_z} = \sqrt{-i}$. Then we obtain the form of $g_z(\mathbf{r}, \mathbf{r}', \tau)$

$$g_z(z, z', \tau) = \sqrt{\frac{\mu\omega_z}{2\pi i\hbar sin\theta_z}} e^{\frac{i\mu\omega_z}{\hbar sin\theta_z}[cos\theta_z \frac{z^2+z'^2}{2} - zz']} \qquad (3.29)$$

as well as $g_x(x, x', \tau)$ and $g_y(y, y', \tau)$. Then, put these back in equation (3.17) to obtain the Green's function.

$$
\begin{aligned}
G(\mathbf{r},\mathbf{r}',t-t') \quad = \quad & \frac{i}{\hbar}\theta(t-t')\left[\left(\frac{\mu}{2\pi i\hbar}\right)^3 \frac{\omega_x\omega_y\omega_z}{\sin\theta_x\sin\theta_y\sin\theta_z}\right]^{\frac{1}{2}} \\
& \cdot e^{\frac{i\mu\omega_x}{\hbar\sin\theta_x}\left[\cos\theta_x\frac{x^2+x'^2}{2}-xx'\right]} \\
& \cdot e^{\frac{i\mu\omega_y}{\hbar\sin\theta_y}[\cos\theta_y\frac{y^2+y'^2}{2}-yy']} \\
& \cdot e^{\frac{i\mu\omega_z}{\hbar\sin\theta_z}[\cos\theta_z\frac{z^2+z'^2}{2}-zz']}
\end{aligned}
\tag{3.30}
$$

3.2 Bound state and scattering state wave functions

In radio-frequency spectroscopy experiment, the initial and final states for transitions are either scattering eigenstates or bound eigenstates. By using the Green's function we have obtained, we can determine the eigenstates and dimer binding energies as well as the scattering states.

Based on the solution of Schródinger equation (3.9), for the eigenstate $\psi_E(\mathbf{r})$ that we want to calculate, we have

$$\psi_E(\mathbf{r},t) = e^{-\frac{i}{\hbar}Et}\psi_E(\mathbf{r})$$

$$\psi_E^{(0)}(\mathbf{r},t) = e^{-\frac{i}{\hbar}Et}\psi_E^{(0)}(\mathbf{r}). \tag{3.31}$$

So, we can obtain the eigenstate directly from the time-dependent Green's function,

$$\psi_E(\mathbf{r}) = \psi_E^{(0)}(\mathbf{r}) - \int_{-\infty}^{\infty} dt' \int d^3\mathbf{r}' G(\mathbf{r},\mathbf{r}',t-t')V(\mathbf{r}')e^{\frac{i}{\hbar}E(t-t')}\psi_E(\mathbf{r}') \tag{3.32}$$

From equation (3.32) and (3.17) , we can define a stationary Green's function for an eigenstate.

$$G_E(\mathbf{r}, \mathbf{r}') \equiv \frac{i}{\hbar} \int_0^\infty d\tau e^{\frac{i}{\hbar}E\tau} g(\mathbf{r}, \mathbf{r}', \tau). \tag{3.33}$$

Then we can write down integral equations for the eigenstate wave functions.

For a scattering state,

$$\psi_{E_s}(\mathbf{r}) = \psi_E^{(0)}(\mathbf{r}) - \int d^3\mathbf{r}' G_E(\mathbf{r}, \mathbf{r}') V(\mathbf{r}') \psi_E(\mathbf{r}'), \tag{3.34}$$

where $\psi_E^{(0)}$ is an input plane wave in free space.

For a bound state,

$$\psi_{E_b}(\mathbf{r}) = -\int d^3\mathbf{r}' G_E(\mathbf{r}, \mathbf{r}') V(\mathbf{r}') \psi_E(\mathbf{r}'). \tag{3.35}$$

there is no input and $\psi_E^{(0)} = 0$.

Let's consider the bound state first. By using the pseudo-potential form for $V(\mathbf{r})$ (3.4), we can write the bound state as

$$\begin{aligned} \psi_{E_b}(\mathbf{r}) &= -\frac{4\pi\hbar^2 a}{m} G_{E_b}(\mathbf{r}, 0) \frac{\partial}{\partial r'} [r' \psi_E(\mathbf{r}')] \mid_{r' \to 0} \\ &= -\frac{4\pi\hbar^2 a}{m} G_{E_b}(\mathbf{r}, 0) u_E'(0) \\ &= A G_{E_b}(\mathbf{r}, 0). \end{aligned} \tag{3.36}$$

where G_{E_b} is bound state Green's function, and $\psi_E(\mathbf{r}) \equiv \frac{u_E(r)}{r}$ and $\psi_E^{(0)}(\mathbf{r}) = \frac{u_E^{(0)}(r)}{r}$. Here, $\psi_E(\mathbf{r})$ is proportional to $G_{E_b}(\mathbf{r})$, A is a coefficient. If E has been determined, we can determine the wave function of the corresponding bound state. So, our next goal is to find E.

Hit both sides of (3.36) with $\frac{\partial}{\partial r}[r...]|_{r\to 0}$ to obtain,

$$\begin{aligned} 1 &= -\frac{4\pi\hbar^2 a}{m}\frac{\partial}{\partial r}[rG_{E_b}(\mathbf{r},0)]|_{r\to 0} \\ &= -\frac{4\pi\hbar^2 a}{m}[G_{E_b}(\mathbf{r},0) - G_0(\mathbf{r})]|_{r\to 0} \end{aligned} \tag{3.37}$$

Here $G_0(\mathbf{r})$ is the part of G_{E_b} that is $\propto \frac{1}{r}$. Note that $\frac{\partial}{\partial r}[rG_0(r)] = 0$ and $G_E - G_0$ is regular at $r = 0$. (3.37) is a self consistent equation which we can use to determine E. Let's find the form of $G_0(\mathbf{r})$.

From 3.29 and 3.30, $G_{E_b}(\mathbf{r}, \mathbf{r}' \to 0)$ is

$$\begin{aligned} G_{E_b}(\mathbf{r},0) &= \frac{i}{\hbar}\left(\frac{m}{4\pi i\hbar}\right)^{3/2}\int_0^\infty d\tau e^{\frac{i}{\hbar}E\tau}\left(\frac{\omega_x\omega_y\omega_z}{\sin\theta_x\sin\theta_y\sin\theta_z}\right)^{1/2} \\ &\cdot e^{\frac{im\omega_x}{\hbar\sin\theta_x}\cos\theta_x\frac{x^2}{4}}\cdot e^{\frac{im\omega_y}{\hbar\sin\theta_y}\cos\theta_y\frac{y^2}{4}}\cdot e^{\frac{im\omega_z}{\hbar\sin\theta_z}\cos\theta_z\frac{z^2}{4}}. \end{aligned} \tag{3.38}$$

Set $\xi \equiv \omega_z\tau$, $l_i^2 = \frac{\hbar}{m\omega_i}$, $\beta_i = \frac{\omega_i}{\omega_z}$, $i = x, y, z$, $E_0 = \frac{\hbar\omega_x}{2} + \frac{\hbar\omega_y}{2} + \frac{\hbar\omega_z}{2}$ and $E - E_0 = -E_b$, where the binding energy $E_b = \epsilon_b\hbar\omega_z > 0$. Then,

$$\begin{aligned} G_{E_b}(\mathbf{r},0) &= \frac{1}{4\pi\hbar\omega_z l_x l_y l_z}\int_0^\infty \frac{id\xi}{\sqrt{4\pi}}e^{-i\epsilon_b\xi}\left(\frac{2}{1-e^{-2i\xi}}\right)^{\frac{1}{2}} e^{i\cot\xi(\frac{z}{2l_z})^2} \\ &\cdot\left(\frac{2}{1-e^{-2i\xi\beta_x}}\right)^{\frac{1}{2}} e^{i\cot(\xi\beta_x)(\frac{x}{2l_x})^2} \\ &\cdot\left(\frac{2}{1-e^{-2i\xi\beta_y}}\right)^{\frac{1}{2}} e^{i\cot(\xi\beta_y)(\frac{y}{2l_y})^2}. \end{aligned} \tag{3.39}$$

By changing to real variables $\xi \to -iu$, we get

$$\begin{aligned} G_{E_b}(\mathbf{r},0) &= \frac{1}{4\pi\hbar\omega_z l_z^3}\int_0^\infty \frac{du}{\sqrt{4\pi}} e^{-\epsilon_b u}\left(\frac{2}{1-e^{-2u}}\right)^{\frac{1}{2}} e^{-\coth(u)(\frac{z}{2l_z})^2} \\ &\cdot \left(\frac{2\beta_x}{1-e^{-2u\beta_x}}\right)^{\frac{1}{2}} e^{-\coth(u\beta_x)(\frac{x}{2l_x})^2} \\ &\cdot \left(\frac{2\beta_y}{1-e^{-2u\beta_y}}\right)^{\frac{1}{2}} e^{-\coth(u\beta_y)(\frac{y}{2l_y})^2}. \end{aligned} \tag{3.40}$$

There are three important length scales in the system: r, the distance between the two atoms; a, the s-wave scattering length and the harmonic oscillator length scale in the tight confinement direction, $l_z \equiv \sqrt{\hbar/(m\omega_z)}$. For the limit $r \to 0$, we consider $r \ll a \ll l_z$. So that $\frac{\hbar^2}{mr^2} \gg \frac{\hbar^2}{ma^2} \gg \frac{\hbar^2}{ml_z^2}$ where $\epsilon_b\hbar\omega_z \simeq \frac{\hbar^2}{ma^2}$. Then $\frac{\hbar^2}{mr^2} \gg \epsilon_b\hbar\omega_z \gg \hbar\omega_z$. Since the harmonic confinement has no effect at small r where the kinetic energy dominates, we expect $G_E(\mathbf{r})|_{r\to 0} = G_0(\mathbf{r}) \propto \frac{1}{r}$. But in (3.40), for $\epsilon_b \gg 1$, only terms with small u can survive. So, we can approximately write $\coth(u) \to \frac{1}{u}$, $\frac{2\beta_i}{1-e^{-2u\beta_i}} \to \frac{1}{u}$, $i = x, y, z$ and since $r^2 = x^2 + y^2 + z^2$,

$$G_{E_b}(\mathbf{r}) = \frac{1}{4\pi\hbar\omega_z}\frac{1}{l_z^3}\int_0^\infty \frac{du}{\sqrt{4\pi u^3}} e^{-\epsilon_b u - \frac{r^2}{4ul_z^2}}. \tag{3.41}$$

Let $s^2 = \frac{r^2}{4ul_z^2}$,

$$\begin{aligned} G_{E_b}(\mathbf{r}) &= \frac{m}{4\pi\hbar^2 r}\frac{2}{\sqrt{\pi}}\int_0^\infty ds e^{-s^2 - \left(\frac{-r\sqrt{\epsilon_b/l_z^2}}{2}\right)^2 \frac{1}{s^2}} \\ &= \frac{m}{4\pi\hbar^2 r} e^{-r\sqrt{\epsilon_b/l_z^2}} \end{aligned} \tag{3.42}$$

The 3D molecular dimer binding energy is approximately $\frac{\hbar^2}{ma^2}$ when $l_z \gg a$, where the dimer can barely feel the harmonic trap. Hence,$\epsilon_b \hbar\omega_z \simeq \frac{\hbar^2}{ma^2}$. Then we get

$$G_{E_b}(\mathbf{r}) = \frac{m}{4\pi\hbar^2 r} e^{-r/a}. \tag{3.43}$$

For $r \ll a$, $G_{E_b}(\mathbf{r})$ is the G_0 we are looking for

$$G_0(\mathbf{r}) = \frac{m}{4\pi\hbar^2 r}, \tag{3.44}$$

which is exactly the free-particle Green's function for small r. That means equation (3.41) will turn into G_0's equation as well when $r \ll a \ll l_z$. Hence, we can write

$$G_0(\mathbf{r}) \to \frac{m}{4\pi\hbar^2 l_z} \int_0^\infty \frac{du}{\sqrt{4\pi u^3}} \tag{3.45}$$

This is the form of G_0 we will put back into (3.37) with $G_{E_b}(\mathbf{r})$ from (3.40)

$$G_{E_b}(\mathbf{r}) = \frac{m}{4\pi\hbar^2} \frac{1}{l_z} \int_0^\infty \frac{due^{-\epsilon_b u}}{\sqrt{4\pi u^3}} \prod_j (\frac{2\beta_j u}{1 - e^{-2\beta_j u}})^{1/2} e^{-coth(\beta_j u)(x_j/2l_j)^2}, \tag{3.46}$$

considering $r \to 0$ which makes the last term of G_{E_b} become 1, we have from (3.37)

$$\frac{l_z}{a} = \int_0^\infty \frac{du}{\sqrt{4\pi u^3}} \left[1 - \prod_j \left(\frac{2\beta_j u}{1 - e^{-2\beta_j u}} \right)^{1/2} e^{-\epsilon_b u} \right], \tag{3.47}$$

where we recall $\beta_j = \frac{\omega_j}{\omega_z}$. This is the self-consistent function that we can use to calculate $E_b = \epsilon_b \hbar\omega_z$.

I plot $\epsilon_b = E_b/(h\nu_z)$ versus l_z/a in Figure 3.1. As l_z/a become positive and large, the difference between blue and red lines, which shows the effect of the transverse confinement, is not so important as when l_z/a is small. That's because when l_z/a is big, $a \ll l_z$, $\frac{\hbar^2}{ma^2} \gg h\nu_z$, the dimer is tightly bound and its size is

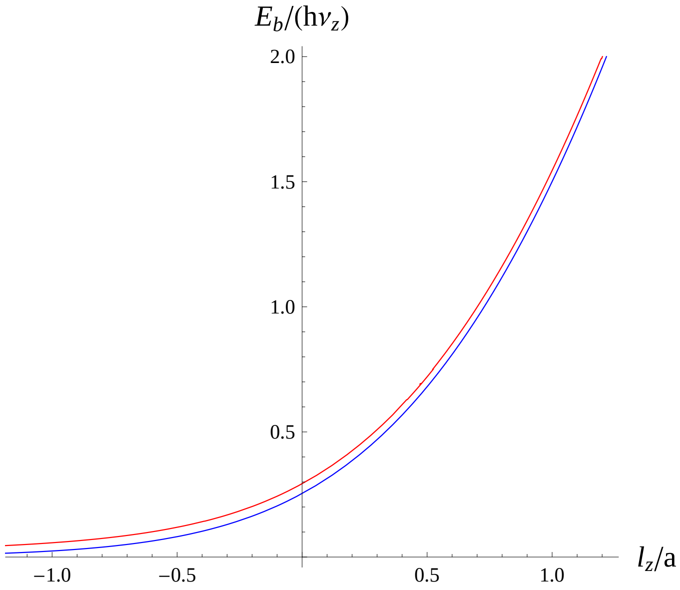

Figure 3.1: $\epsilon_b = E_b/(h\nu_z)$ versus l_z/a. The blue lower line is for $\nu_\perp = 0$ with no transverse confinement. The red upper line is for $\nu_\perp = \nu_z/25$.

very small compared with the harmonic oscillator length scale l_z. So, the shape of the trap would not affect the interaction between the two atoms very much.

Experimentally, we know the magnetic field B and trap frequency ν_z, so we can calculate $l_z = \sqrt{\hbar/(m\omega_z)} = (\sqrt{h/(m\nu_z)})/2\pi$ and s-wave scattering length $a(B)$ from the known Feshbach resonance parameters [29]. Solving the integral equation (3.47), we can get $E_b = \epsilon_b \hbar\omega$. In Figure 3.2, I plot three s-wave scattering lengths a_{12}, a_{13}, a_{23} versus magnetic field [29].

In Figure 3.3, I plot the binding energy E_b for 12, 13 and 23 dimer states as a function of magnetic field. I also show the relative magnitudes by putting them on the same graph (right bottom graph in Figure 3.3). We can see that the 13 binding energy is always smaller than the 12 and 23 binding energy in the region from 690 G to 850 G, where we do the rf spectroscopy experiment. The transverse confinement $\nu_\perp = \nu_z/25$, which we have experimentally, will increase the

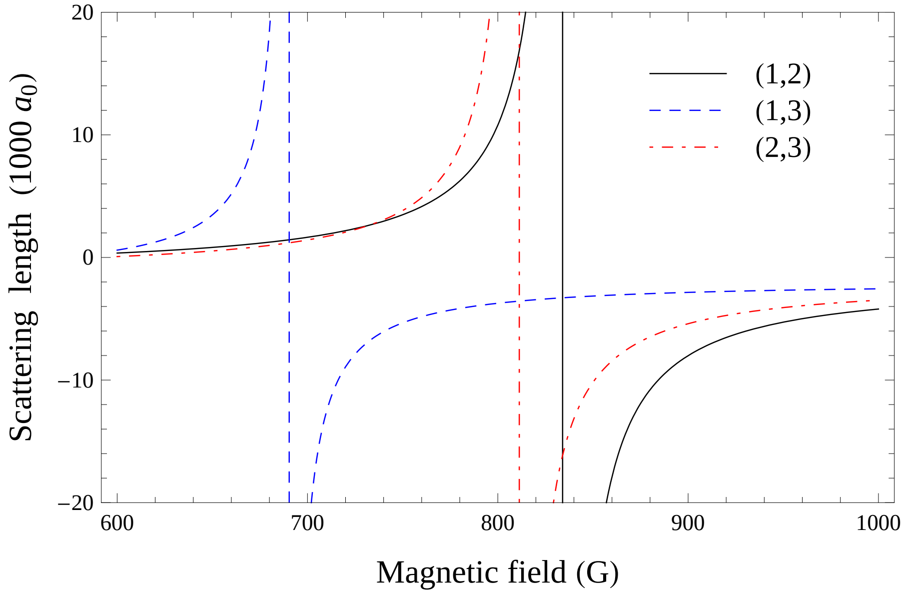

Figure 3.2: S-wave scattering lengthes versus magnetic field for the (1,2), (1,3) and (2,3) scattering channels.

binding energy significantly especially for high magnetic field and small binding energies. Here I list some binding energies which we will use later to compare with experimental data in Table 3.1 and Table 3.2.

Now we can go ahead and calculate the bound state and scattering state wave functions. Since in our system, $\omega_\perp/\omega_z = 1/25$, we use the approximation $\omega_\perp \ll \omega_z$, where $\beta_x, \beta_y \to 0$ while $\beta_z = 1$. Then, in equation (3.46), $\frac{2\beta_x u}{1-e^{-2\beta_x u}} \to 1$, $coth(\beta_x u)\frac{x^2}{4l_x^2} \to \frac{x^2}{\beta_x u 4l_x^2} = (\frac{x}{2l_z})^2\frac{1}{u}$, and similarly for the y direction. In the z direction, $\frac{2\beta_z u}{1-e^{-2\beta_z u}} \to \frac{2u}{1-e^{-2u}}$. So that,

$$G_{E_b}(\mathbf{r}) = \frac{m}{4\pi\hbar^2}\frac{1}{l_z}\int_0^\infty \frac{due^{-\epsilon_b u}}{\sqrt{4\pi u^3}}\left(\frac{2u}{1-e^{-2u}}\right)^{1/2} e^{-\coth u(z/2l_z)^2} e^{-(\frac{\rho}{2l_z})^2\frac{1}{u}}. \qquad (3.48)$$

Here $\rho = \sqrt{x^2+y^2}$. The bound state should be lower than the harmonic trap ground state, but very close to it, when the binding energy is small. The ground

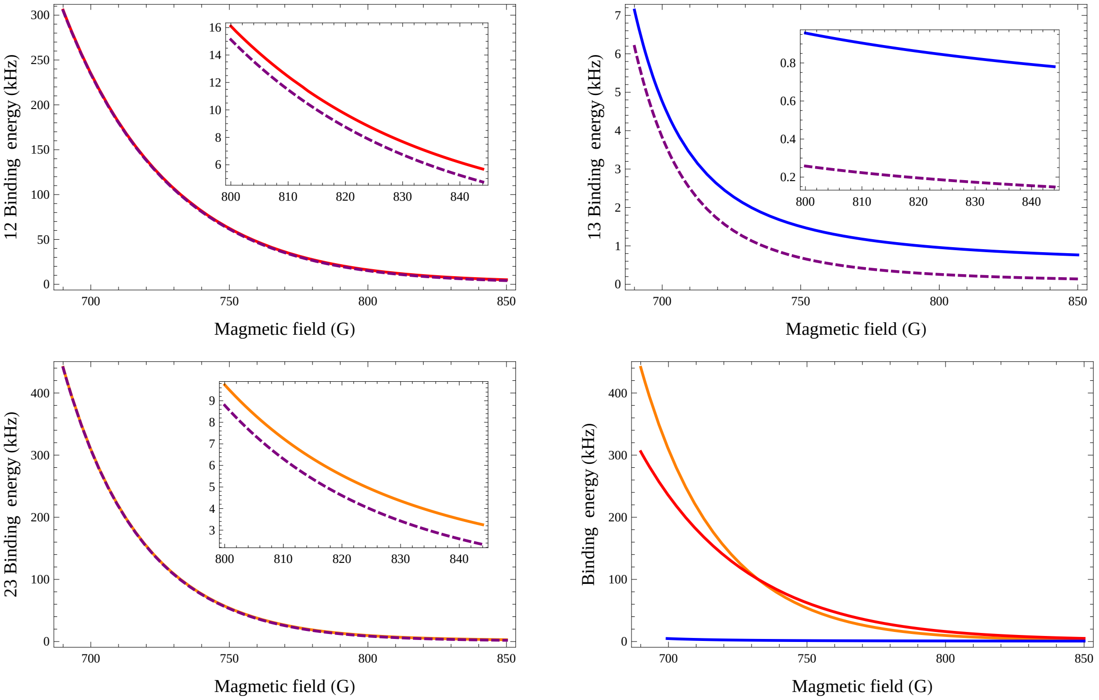

Figure 3.3: Dimer binding energies versus magnetic field when $\nu_z = 24.5$ kHz. The solid red, blue and orange lines are for $\nu_\perp = \nu_z/25$ while the purple dash lines are for $\nu_\perp = 0$ respectively. The graph on the left top shows 12 binding energy. Red line is for $\nu_\perp = \nu_z/25$ and purple dash line is for $\nu_\perp = 0$; The graph on the right top shows 13 binding energy. Blue line is for $\nu_\perp = \nu_z/25$ and purple dash line is for $\nu_\perp = 0$; The graph on the left bottom shows 23 binding energy. Orange line is for $\nu_\perp = \nu_z/25$ and purple dash line is for $\nu_\perp = 0$; The insets of these three graphs are the comparison of $\nu_\perp = \nu_z/25$ and $\nu_\perp = 0$ in high magnetic field where the differences between them are obvious. The graph on the right bottom is the comparison of 12, 13 and 23 binding energy for $\nu_\perp = \nu_z/25$.

Table 3.1: Dimer binding energies for ν_z around 24 kHz. Frequencies and energies are given in units of kHz. E_{b0} is the case for no transverse confinement $\nu_\perp = 0$ while E_b includes the transverse confinement $\nu_\perp = \nu_z/25$.

B(G)	ν_z	E_{b0}^{13}	E_b^{13}	E_{b0}^{12}	E_b^{12}	E_{b0}^{23}	E_b^{23}
688.9	24.5	6.47	7.43	313.9	314.8	458.7	459.7
718.5	26.0	1.95	2.91	144.2	145.3	161.8	162.9
728.5	24.5	1.26	2.13	109.9	110.9	113.4	114.4
748.0	25.0	0.74	1.58	64.90	65.90	56.72	57.82
768.2	24.5	0.45	1.21	36.82	37.80	27.11	28.09
788.5	24.5	0.30	1.03	20.72	21.70	12.98	13.95
808.6	24.0	0.21	0.88	11.63	12.58	6.39	7.33
832.2	24.5	0.17	0.81	6.29	7.25	3.17	4.11
841.7	24.5	0.15	0.78	4.96	5.91	2.15	3.37

state axial wave function is $\phi_0(z) = \phi_0(0)e^{-(\frac{z}{2l_z})^2}$ with $\phi_0(0) = \frac{1}{(2\pi l_z^2)^{1/4}}$. For small ϵ_b, it is reasonable to assume that the primary component of the bound state wave function is the projection onto $\phi_0(z)$.

$$\begin{aligned} I_{E_b}(\rho) &= \int_{-\infty}^{\infty} dz\, G_E(\mathbf{r})\phi_0(z) \\ &= \phi_0(0)\frac{m}{4\pi\hbar^2}\frac{1}{l_z}\int_0^{\infty}\frac{due^{-\epsilon_b u}}{\sqrt{4\pi u^3}}e^{-(\frac{\rho}{2l_z})^2\frac{1}{u}}I_z(u), \end{aligned} \tag{3.49}$$

where

$$\begin{aligned} I_z(u) &= \int_{-\infty}^{\infty} dze^{-(\frac{z}{2l_z})^2(1+cothu)}\left(\frac{2u}{1-e^{-2u}}\right)^{1/2} \\ &= \sqrt{\frac{\pi(2l_z)^2}{1+\coth u}}\left(\frac{2u}{1-e^{-2u}}\right)^{1/2} = \sqrt{4\pi}l_z u^{1/2}. \end{aligned} \tag{3.50}$$

Table 3.2: Dimer binding energies for ν_z around 82 kHz. Frequencies and energies are given in units of kHz. E_{b0} is the case for no transverse confinement $\nu_\perp = 0$ while E_b includes the transverse confinement $\nu_\perp = \nu_z/25$.

B(G)	ν_z	E_{b0}^{13}	E_b^{13}	E_{b0}^{12}	E_b^{12}	E_{b0}^{23}	E_b^{23}
688.9	82.5	21.03	24.26	342.0	345.3	487.0	490.3
718.5	81.5	10.36	13.47	170.2	173.5	188.0	191.2
728.3	82.5	8.82	11.94	137.1	140.4	140.9	144.2
748.0	83.5	6.65	9.75	90.31	93.64	81.78	85.11
767.5	82.5	5.13	8.13	60.80	64.07	49.74	53.01
788.3	82.5	4.17	7.11	41.39	44.66	31.27	34.52
809.5	85.0	3.71	6.69	29.76	33.11	21.40	24.72
832.0	82.0	2.97	5.79	20.64	23.85	14.27	17.44
841.7	82.5	2.84	5.66	18.20	21.41	12.49	15.66

Then,

$$
\begin{aligned}
I_{E_b}(\rho) &= \phi_0(0)\frac{m}{4\pi\hbar^2}\int_0^\infty \frac{du}{u} e^{-\epsilon_b u - \frac{1}{u}\left(\frac{\rho}{2l_z}\right)^2} \\
&= \phi_0(0)\frac{m}{4\pi\hbar^2} 2K_0\left(\frac{\rho\sqrt{\epsilon_b}}{l_z}\right),
\end{aligned}
\tag{3.51}
$$

where K_0 is a modified Bessel function. This is the projection of $G_E(\mathbf{r})$ onto $\phi_0(z)$. Since $\phi_0(0)\frac{m}{2\pi\hbar^2}$ is a coefficient, we can write the bound state wave function as

$$
\psi_{E_b}(\mathbf{r}) = A\phi_0(z)K_0\left(\frac{\sqrt{\epsilon_b}\rho}{l_z}\right). \tag{3.52}
$$

Here A is the normalization coefficient. The normalization gives

$$
\int_{-\infty}^{\infty} dz \int_0^\infty 2\pi\rho d\rho |A|^2 \phi_0^2(z) K_0^2\left(\frac{\sqrt{\epsilon_b}\rho}{l_z}\right) = 1. \tag{3.53}
$$

We can get $A = \frac{\sqrt{\epsilon_b}}{l_z\sqrt{\pi}}$. If we define $\kappa = \sqrt{\epsilon_b}/l_z$, the bound state wave function can be approximately written as

$$\psi_{E_b}(z,\rho) = \frac{\kappa}{\sqrt{\pi}}\phi_0(z)K_0\left(\kappa\rho\right). \tag{3.54}$$

Here we have ignored other components from higher axial states like $\phi_2, \phi_4, ...$ since the binding energy we consider is small compared with $\hbar\omega_z$.

For the scattering state, from (3.34),

$$\psi_{E_s}(\mathbf{r}) = \psi^{(0)}_{E_s}(\mathbf{r}) - \frac{4\pi\hbar^2 a}{m}G_{E_s}(\mathbf{r},0)\frac{\partial}{\partial r'}[r'\psi_{E_s}(\mathbf{r}')]|_{r'\to 0} \tag{3.55}$$

Here the E_s in the subscript means scattering state energy, $E - E_0 = E_s = \epsilon\hbar\omega_z$, $\epsilon > 0$. Assuming that the scattering occurs in the ground axial state, for $E_s < \hbar\omega_z$, we take $E_s = \frac{\hbar^2 k_\perp^2}{m}$, the relative kinetic energy in the transverse direction. As we did for bound state, hit both sides of (3.55) with $\frac{\partial}{\partial r}[r...]$ to obtain,

$$u'_{E_s}(0) = u'^{(0)}_{E_s}(0) - \frac{4\pi\hbar^2 a}{m}\frac{\partial}{\partial r}\left[rG_{E_s}(\mathbf{r})\right]|_{r\to 0}u'_{E_s}(0) \tag{3.56}$$

Here $u_{E_s} = r\psi_{E_s}$, and is regular in the origin. So,

$$u'_{E_s}(0) = \frac{u'^{(0)}_{E_s}(0)}{1 + \frac{4\pi\hbar^2 a}{m}\frac{\partial}{\partial r}\left[rG_{E_s}(\mathbf{r})\right]|_{r\to 0}} \tag{3.57}$$

Since for the bound state we have $1 = -\frac{4\pi\hbar^2 a}{m}\frac{\partial}{\partial r}[rG_{E_b}(\mathbf{r},0)]|_{r\to 0}$ from (3.37), let's replace the 1 in (3.57),

$$u'_{E_s}(0) = \frac{m}{4\pi\hbar^2 a}\frac{u'^{(0)}_{E_s}(0)}{\left\{-\frac{\partial}{\partial r}\left[rG_{E_b}(\mathbf{r})\right]|_{r\to 0} + \frac{\partial}{\partial r}\left[rG_{E_s}(\mathbf{r})\right]|_{r\to 0}\right\}} \tag{3.58}$$

In the denominator, subtraction $\frac{\partial}{\partial r}\left[r(G_{E_s} - G_{E_b})\right]|_{r\to 0}$ cancels out the irregular parts $\propto \frac{1}{r}$ in both Green's functions. And the remaining parts are regular when $r \to 0$. So, we can write $\frac{\partial}{\partial r}\left[r(G_{E_s} - G_{E_b})\right]|_{r\to 0} = (G_{E_s} - G_{E_b})|_{r\to 0}$.

$$u'_{E_s}(0) = \frac{m}{4\pi\hbar^2 a}\frac{u'^{(0)}_{E_s}(0)}{\left[G_{E_s}(\mathbf{r}) - G_{E_b}(\mathbf{r})\right]|_{r\to 0}} \tag{3.59}$$

If we put (3.59) back into (3.55), and consider $u'^{(0)}_{E_s}(0) = \frac{\partial}{\partial r}[r\psi^{(0)}_{E_s}]|_{r\to 0} = \psi^{(0)}_{E_s}(0)$ since the input state is regular at $r = 0$, we obtain the simple form

$$\begin{aligned}\psi_{E_s}(\mathbf{r}) &= \psi^{(0)}_{E_s}(\mathbf{r}) - \frac{G_{E_s}(\mathbf{r})u'^{(0)}_{E_s}(0)}{[G_{E_s}(\mathbf{r}) - G_{E_b}(\mathbf{r})]|_{r\to 0}} \\ &= \psi^{(0)}_{E_s}(\mathbf{r}) - \frac{G_{E_s}(\mathbf{r})\psi^{(0)}_{E_s}(0)}{[G_{E_s}(\mathbf{r}) - G_{E_b}(\mathbf{r})]|_{r\to 0}}.\end{aligned} \tag{3.60}$$

We have already done the projection of the bound state Green's function G_{E_b} onto ϕ_0. In the same way, we can do the projection of the scattering state Green's function G_{E_s} onto ϕ_0. But here we replace E_b by E_s, so we should start from (3.39) and change $\epsilon_b \to -\epsilon$. Again, we can make the same approximations based on $\omega_\perp \ll \omega_z$ and $\beta_x, \beta_y \ll 1$. So, $\frac{2\beta_x}{1-e^{2i\xi\beta_x}} \to \frac{1}{i\xi}$, $\cot(\xi\beta_x)\frac{1}{l_x^2} \to \frac{\xi}{l_z^2}$, and similarly for the y direction. Then, we can write $G_{E_s}(\mathbf{r})$ as,

$$G_{E_s}(\mathbf{r}) = \frac{m}{4\pi\hbar^2}\frac{1}{l_z}\int_0^\infty \frac{d\xi e^{i\epsilon\xi}}{\sqrt{4\pi\xi^2}}\left(\frac{2}{1-e^{-2i\xi}}\right)^{1/2} e^{i\cot\xi(\frac{z}{2l_z})^2 + \frac{i}{\xi}(\frac{\rho^2}{2l_z})} \tag{3.61}$$

Then when we do the projection onto the ground axial state, we have

$$\begin{aligned}I_{E_s}(\rho) &= \int_{-\infty}^{\infty} dz\phi_0(z)G_{E_s}(\mathbf{r}) \\ &= \phi_0(0)\frac{m}{4\pi\hbar^2}\frac{1}{l_z}\int_0^\infty \frac{d\xi e^{-i\epsilon_b\xi}}{\sqrt{4\pi\xi^2}} e^{(\frac{\rho}{2l_z})^2\frac{i}{\xi}} I'_z(\xi)\end{aligned} \tag{3.62}$$

$$
\begin{aligned}
I'_z(\xi) &= \int_{-\infty}^{\infty} dz\, e^{-(\frac{z}{2l_z})^2(1-i\cot\xi)} \left(\frac{2}{1-e^{-2i\xi}}\right)^{1/2} \\
&= \sqrt{\frac{\pi(2l_z)^2}{1-i\cot\xi}} \left(\frac{2}{1-e^{-2i\xi}}\right)^{1/2} = \sqrt{4\pi}\, l_z
\end{aligned}
\tag{3.63}
$$

$$
\begin{aligned}
I_{E_s}(\rho) &= \phi_0(0)\frac{m}{4\pi\hbar^2}\int_0^{\infty}\frac{d\xi}{\xi}e^{-i\epsilon_b\xi+\frac{i}{\xi}(\frac{\rho}{2l_z})^2} \\
&= \phi_0(0)\frac{m}{4\pi\hbar^2}\pi i H_0^{(1)}(k_\perp\rho)
\end{aligned}
\tag{3.64}
$$

here, $k_\perp$ is from $\epsilon = \frac{1}{\hbar\omega_z}\frac{\hbar^2 k_\perp^2}{m}$, the relative kinetic energy in unit of $\hbar\omega_z$, and $H_0^{(1)}$ is a Hankel function.

We know the input wave function for the first term on the right side of (3.60) by considering only the $l = 0$ component of a box-normalized (to area A) plane wave input state $\frac{1}{\sqrt{A}}e^{i\mathbf{k}_\perp\cdot\rho}$ in the transverse direction, i.e.,

$$
\psi_{k_\perp}^{(0)}(\rho) = \frac{1}{\sqrt{A}}J_0(k_\perp\rho). \tag{3.65}
$$

Here, A is the area and J_0 is a Bessel function. In the z direction, we only consider the ground axial state. So the input state is

$$
\psi_{E_s}^{(0)}(\mathbf{r}) = \phi_0(z)\frac{1}{\sqrt{A}}J_0(k_\perp\rho). \tag{3.66}
$$

Then let's put (3.66), (3.61) and (3.64) into (3.60). We obtain the wave function for the scattering state. Since

$$
H_0^{(1)}(x) = J_0(x) + iY_0(x), \tag{3.67}
$$

$$K_0(x) = \frac{i\pi}{2}[J_0(ix) + iY_0(ix)], \tag{3.68}$$

We get

$$\begin{aligned}\psi_{E_s}(\mathbf{r}) &= \phi_0(z)\frac{1}{\sqrt{A}}J_0(k_\perp\rho) \\ &\quad -\frac{\phi_0(z)\phi_0(0)\frac{m}{4\pi\hbar^2}\pi i H_0^{(0)}(k_\perp\rho)\psi_{E>0}^{(0)}(0)}{\phi_0(0)\left[\phi_0(0)\frac{m}{4\pi\hbar^2}\pi i H_0^{(0)}(k_\perp\rho) - \phi_0(0)\frac{m}{4\pi\hbar^2}2K_0(\frac{\rho\sqrt{\epsilon_b}}{l_z})\right]|_{\rho\to 0}}.\end{aligned}$$

Here, $\psi_{E_s}^{(0)}(0) = \phi_0(0)\frac{1}{\sqrt{A}}J_0(0) = \phi_0(0)\frac{1}{\sqrt{A}}$. Using (3.67) and (3.68) in the denominator, we obtain

$$\psi_{E_s}(\mathbf{r}) = \phi_0(z)\frac{1}{\sqrt{A}}\left[J_0(k_\perp\rho) - \frac{\pi i}{\pi i + ln(\frac{\epsilon_b}{\epsilon_\perp})}H_0^{(1)}(k_\perp\rho)\right] \tag{3.69}$$

for a scattering state of relative kinetic energy $\frac{\hbar^2 k_\perp^2}{m} = \epsilon_\perp\hbar\omega_z$.

Equations (3.54) and (3.69) give the wave functions of dimer bound state and scattering state. They can be used as initial and final states to calculate the radio-frequency(rf) transition spectrum in equation (2.74), which we derived using Fermi's Golden rule in Chpter2.

3.2.1 Bound to bound transition

We assume the transition is from ^{6}Li hyperfine states $|1\rangle\,|2\rangle$ pair state to a $|1\rangle\,|3\rangle$ pair state. For a bound to bound transition,

$$
\begin{aligned}
|I\rangle &= \phi_0(z)\psi_{12}(\rho) = \frac{\kappa_{12}}{\sqrt{\pi}}\phi_0(z)K_0\left(\kappa_{12}\rho\right), \\
|F\rangle &= \phi_0(z)\psi_{13}(\rho) = \frac{\kappa_{13}}{\sqrt{\pi}}\phi_0(z)K_0\left(\kappa_{13}\rho\right), \\
\mu &= \frac{m}{2}, \quad E_b^{12} =\frac{\hbar^2\kappa_{12}^2}{m}, \quad E_b^{13} = \frac{\hbar^2\kappa_{13}^2}{m}, \\
\int_0^\infty 2\pi\rho d\rho|\psi_{12}(\rho)|^2 &= \int_0^\infty 2\pi\rho d\rho|\psi_{13}(\rho)|^2 = 1, \quad \int dz|\phi_0(z)|^2 = 1
\end{aligned}
$$

Then the overlap of the initial and final bound states is

$$
\langle F|I\rangle = \int_0^\infty 2\pi\rho d\rho\psi_{12}(\rho)\psi_{13}(\rho) \tag{3.70}
$$

Since

$$
\int_0^\infty \rho d\rho K_0(\kappa_{12}\rho)K_0(\kappa_{13}\rho) = \frac{ln\left(\frac{\kappa_{12}}{\kappa_{13}}\right)}{\kappa_{12}^2-\kappa_{13}^2}, \tag{3.71}
$$

we have

$$
\begin{aligned}
\langle F|I\rangle &= = \frac{2\pi\kappa_{12}\kappa_{13}}{\pi}\frac{ln\left(\frac{\kappa_{12}}{\kappa_{13}}\right)}{\kappa_{12}^2-\kappa_{13}^2} \\
&= \frac{2\sqrt{E_b^{12}E_b^{13}}}{E_b^{12}-E_b^{13}}\,ln\sqrt{\frac{E_b^{12}}{E_b^{13}}} \\
&= \frac{\sqrt{E_b^{12}E_b^{13}}}{E_b^{12}-E_b^{13}}\,ln\left(\frac{E_b^{12}}{E_b^{13}}\right).
\end{aligned} \tag{3.72}
$$

Using this in equation (2.74),

$$\begin{aligned} I_{12b\to 13b}(\omega) &= \sum_F |\langle F|I\rangle|^2\,\hbar\,\delta(E_F - E_I - \hbar\omega) \\ &= \frac{E_b^{12}E_b^{13}}{(E_b^{12}-E_b^{13})^2}\left[ln\left(\frac{E_b^{12}}{E_b^{13}}\right)\right]^2\hbar\,\delta(E_b^{12}-E_b^{13}-\hbar\omega), \qquad (3.73) \end{aligned}$$

where b in the subscript denotes bound state. In order to make the expression more concise, we define

$$q \equiv ln\left(\frac{E_b^{13}}{E_b^{12}}\right), \qquad (3.74)$$

and

$$\epsilon_{bb} \equiv \frac{E_b^{12}E_b^{13}}{(E_b^{12}-E_b^{13})^2}\left[ln\left(\frac{E_b^{12}}{E_b^{13}}\right)\right]^2 = \frac{q^2}{4\sinh^2(q/2)}. \qquad (3.75)$$

Then $I_{12b\to 13b}(\omega)$ can be written as

$$I_{12b\to 13b}(\omega) = \epsilon_{bb}\,\hbar\,\delta\left(\omega - \frac{E_b^{12}-E_b^{13}}{\hbar}\right). \qquad (3.76)$$

In the real experiment, we tend to use Hertz instead of angular frequency. So, it is easier for us to measure the Hertz frequency version for $I_{12b\to 13b}$ in order to compare with experimental results. For a bound to bound transition

$$I_{12b\to 13b}(\nu) = \epsilon_{bb}\,\delta(\nu - \frac{E_b^{12}-E_b^{13}}{h}), \qquad (3.77)$$

$$\int_{-\infty}^{\infty} d\nu I_{12b\to 13b}(\nu) = \epsilon_{bb}. \qquad (3.78)$$

We can see that ϵ_{bb} is the frequency integrated bound to bound transition fraction.

3.2.2 Bound to free transition

For a bound to free transition,

$$
\begin{aligned}
|I\rangle = \phi_0(z)\psi_{12}(\rho) =& \frac{\kappa_{12}}{\sqrt{\pi}}\phi_0(z)K_0\left(\kappa_{12}\rho\right), \\
|F\rangle = \phi_0(z)\psi_{13}(\rho) =& \phi_0(z)\frac{1}{\sqrt{A}}\left[J_0(k_{13\perp}\,\rho) - \frac{\pi i}{\pi i + ln(\frac{E_b^{13}}{E_f^{13}})}H_0^{(1)}(k_{13\perp}\,\rho)\right], \\
\mu = \frac{m}{2},\quad E_b^{12} =& \frac{\hbar^2\kappa_{12}^2}{m},\quad E_b^{13} = \frac{\hbar^2\kappa_{13}^2}{m},\quad E_f^{13} = \frac{\hbar^2 k_{13\perp}^2}{m}, \\
\int dz|\phi_0(z)|^2 = 1&
\end{aligned}
$$

We again calculate the overlap of initial and final states

$$
\langle F|I\rangle = \int_0^\infty 2\pi\rho d\rho\frac{\kappa_{12}}{\sqrt{\pi}}K_0(\kappa_{12}\rho)\frac{1}{\sqrt{A}}\left[J_0(k_{13\perp}\,\rho) - \frac{\pi i}{\pi i + ln(\frac{E_b^{13}}{E_f^{13}})}H_0^{(1)}(k_{13\perp}\,\rho)\right] \tag{3.79}
$$

Since $H_0^{(1)}(k_{13\perp}\,\rho) = J_0(k_{13\perp}\,\rho) + iY_0(k_{13\perp}\,\rho)$, we find

$$
\int_0^\infty \rho d\rho K_0(\kappa_{12}\rho)J_0(k_{13\perp}\,\rho) = \frac{1}{\kappa_{12}^2 + k_{13\perp}^2}, \tag{3.80}
$$

$$
\int_0^\infty \rho d\rho K_0(\kappa_{12}\rho)Y_0(k_{13\perp}\,\rho) = -\frac{2}{\pi}\frac{ln\frac{\kappa_{12}}{k_{13\perp}}}{\kappa_{12}^2 + k_{13\perp}^2}, \tag{3.81}
$$

$$
\begin{aligned}
\int_0^\infty \rho d\rho K_0(\kappa_{12}\rho)H_0^{(1)}(k_{13\perp}\,\rho) =& \frac{1}{\kappa_{12}^2 + k_{13\perp}^2}\left(1 - \frac{2i}{\pi}ln\frac{\kappa_{12}}{k_{13\perp}}\right) \\
=& \frac{1}{\kappa_{12}^2 + k_{13\perp}^2}\left(1 - \frac{i}{\pi}ln\frac{E_b^{12}}{E_f^{13}}\right).
\end{aligned} \tag{3.82}
$$

Then, we sum over all the possible kinetic energies for the free states to get the total transition rate out of the bound state 12 bound:

$$\begin{aligned}
&I_{12b\to13f}(\omega)\\
=&\hbar\int_0^\infty \frac{A}{(2\pi)^2}2\pi k_{13\perp}dk_{13\perp}\left|\int_0^\infty 2\pi\rho d\rho\frac{\kappa_{12}}{\sqrt{\pi}}K_0(\kappa_{12}\rho)\right.\\
&\left.\frac{1}{\sqrt{A}}\left[J_0(k_{13\perp}\,\rho)-\frac{\pi i}{\pi i+ln\left(\frac{E_b^{13}}{E_f^{13}}\right)}H_0^{(1)}(k_{13\perp}\,\rho)\right]\right|^2\delta(E_f^{13}+E_b^{12}-\hbar\omega)\\
=&\hbar\left[ln\left(\frac{E_b^{13}}{E_b^{12}}\right)\right]^2E_b^{12}\int_0^\infty\frac{dE_f^{13}}{(E_b^{12}+E_f^{13})^2}\frac{1}{\left|\pi i+ln\left(\frac{E_b^{13}}{E_f^{13}}\right)\right|^2}\delta(E_f^{13}+E_b^{12}-\hbar\omega)\\
=&\frac{E_b^{12}}{\hbar\omega^2}\left[ln\left(\frac{E_b^{13}}{E_b^{12}}\right)\right]^2\frac{\Theta(\hbar\omega-E_b^{12})}{\left[ln\frac{E_b^{13}}{\hbar\omega-E_b^{12}}\right]^2+\pi^2}. \qquad (3.83)
\end{aligned}$$

We can use the definition of $q = ln(E_b^{13}/E_b^{12})$ to write $I_{12b\to13f}(\omega)$ concisely,

$$I_{12b\to13f}(\omega)=\frac{E_b^{12}}{\hbar\omega^2}\frac{q^2\Theta(\omega-E_b^{12}/\hbar)}{\left[q-ln\left(\frac{\hbar\omega}{E_b^{12}}-1\right)\right]^2+\pi^2}. \qquad (3.84)$$

As I mentioned previously, in order to compare with experimental results, we change the variable from angular frequency into Hertz. Since we defined normalized transition rate I in equation (2.71) as $R_i(\omega) = \frac{\pi}{2}\Omega^2 I(\omega)$ previously, $\int_{-\infty}^{\infty} d\nu I(\nu) = 1$ as well as $\int_{-\infty}^{\infty} d\omega I(\omega) = 1$. We know that $d\omega = 2\pi d\nu$, then $I(\nu) = 2\pi I(\omega)$,

$$I_{12b\to13f}(\nu)=\frac{E_b^{12}}{h\nu^2}\frac{\Theta(\nu-E_b^{12}/h)q^2}{\left[q-ln\left(\frac{h\nu}{E_b^{12}}-1\right)\right]^2+\pi^2} \qquad (3.85)$$

In equation (3.85), the part $\frac{E_b^{12}}{h\nu^2}\Theta(\nu-E_b^{12}/h)$ predicts a threshold spectrum, shown as the blue lines in the top two graphs in Figure 3.4, that would be obtained for

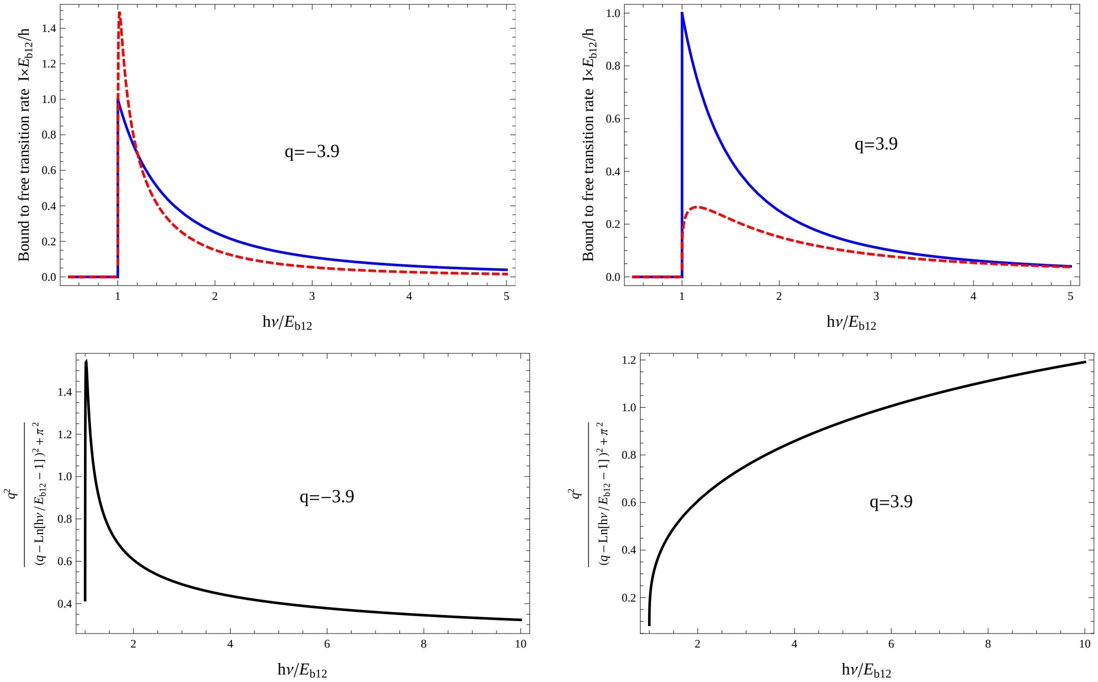

Figure 3.4: Effect of the final state interactions on the bound state to scattering state transition spectrum is shown for different q. In the two graphs on the top, the blue solid lines are the same plot $I(\nu) = \frac{E_b^{12}}{h\nu^2}\Theta(\nu - E_b^{12}/h)$, and the red dash lines show the total transition rate for different q after considering about the logarithm part $I(\nu) = \frac{E_b^{12}}{h\nu^2}\frac{q^2\Theta(\nu - E_b^{12}/h)}{\left[q - ln\left(\frac{h\nu}{E_b^{12}} - 1\right)\right]^2 + \pi^2}$. In the bottom two graphs, the black lines show how the logarithm part of the transition rate vary versus the normalized frequency $h\nu/E_b^{12}$ for plus and minus q. The reason to choose $q = ln\frac{E_b^{13}}{E_b^{12}} \pm 3.9$ is that the q for 2% trap depth at 720G for 12 to 13 transition is about -3.9 and for 13 to 12 transition is about $+3.9$, where we have experimental result to compare with.

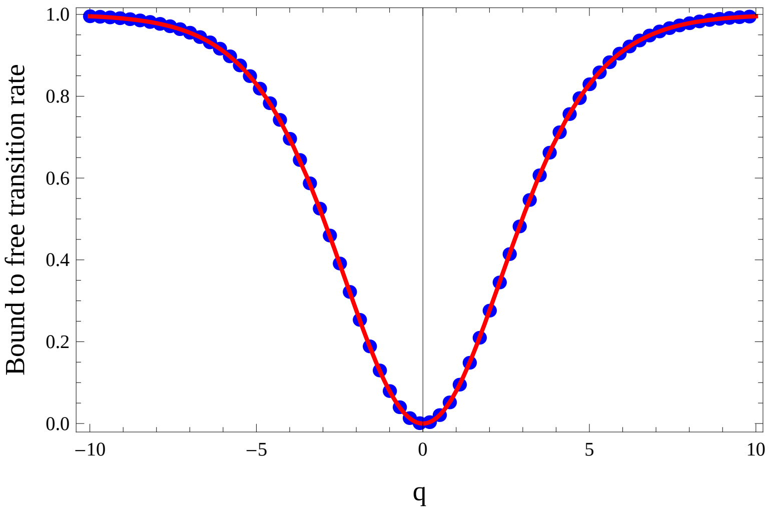

Figure 3.5: $\int_0^\infty d\nu I_{12b\to13f}(\nu) = 1 - \int_0^\infty d\nu I_{12b\to13b}(\nu)$ Frequency integrated bound state to scattering state transition rate $\int_0^\infty d\nu I_{12b\to13f}(\nu)$ in equation (3.85) (Blue dots) compared with $1-\epsilon_{bb}$ (Red line). ϵ_{bb} is the integrated bound to bound transition rate. The exact overlap of blue dots and red line shows that $\int_0^\infty d\nu I_{12b\to13f}(\nu) = 1-\epsilon_{bb} = 1-\frac{q^2}{4\,sinh^2\left(\frac{q}{2}\right)}$

a non-interacting final state, where $E_b^{13}\to 0$ and $q^2\to\infty$. The logarithm part, shown in the bottom two graphs in Figure 3.4, predicts a significant modification of the threshold spectrum, shown as the red dash lines in the upper two graphs.

We can see that for normalized bound state to scattering state transition rate I, the sign of q modifies the shape of the spectrum significantly as shown in Figure 3.4. However, the frequency integrals $\int_0^\infty d\nu I_{12b\to13f}(\nu)$ are the same as long as the magnitude of q is the same, as shown in Figure 3.5, blue dots. These blue dots matches the red line very well. The red line shows 1 minus the integration of bound to bound transition rate $\int_0^\infty d\nu I_{12b\to13b}(\nu)=\epsilon_{bb}$. We expect from (2.75), $\int_{-\infty}^\infty d\nu I(\nu)=1$.

$$\int_0^\infty d\nu I_{12b\to13f}(\nu) = 1-\epsilon_{bb} = 1-\frac{q^2}{4\,sinh^2\left(\frac{q}{2}\right)}, \tag{3.86}$$

This means that the final states including the scattering final states are complete and contain only one bound state which is consistent with our ground axial state assumption.

3.2.3 Summary for the dimer transition rate calculation

In order to compare with the experimental results, we still need to go back to get the real transition rate $R(\nu)$. We know that from equation (2.71) with $I(\nu) = 2\pi I(\omega)$

$$R(\omega) \equiv R(\nu) = \frac{\pi}{2}\Omega_{fi}^2(rad/s)\frac{1}{2\pi}I(\nu). \tag{3.87}$$

Since $\Omega_{fi}(rad/s) = 2\pi\Omega_{fi}(Hz)$, the transition rate in $\sec^{-1}$ as a function of rf frequency in Hz is

$$R(\nu) = \pi^2\Omega_{fi}^2(\mathrm{Hz})I(\nu). \tag{3.88}$$

Then we can use the normalized bound to bound transition rate $I_{12b\to13b}(\nu)$, equation (3.77), and the bound to free transition rate $I_{12b\to13f}(\nu)$, equation (3.85) to get

$$\boxed{R_{12b\to13b}(\nu) = \pi^2\Omega_{fi}^2\epsilon_{bb}\,\delta\left(\nu - \frac{E_b^{12} - E_b^{13}}{h}\right)}, \tag{3.89}$$

$$\boxed{R_{12b\to13f}(\nu) = \pi^2\Omega_{fi}^2\frac{E_b^{12}}{h\nu^2}\frac{q^2\Theta(\nu - E_b^{12}/h)}{\left[q - ln\left(\frac{h\nu}{E_b^{12}} - 1\right)\right]^2 + \pi^2}}. \tag{3.90}$$

Later we will fit them with experimental data.

Chapter 4

Polarons in two dimensions

Besides dimer theory, we also consider many-body physics to explain our experimental results. We notice that zero temperature noninteracting polaron theory in two dimensions can give us resonances positions in rf spectrum that fit our data much better than the dimer predictions. In the regime, where $E_{F\perp} > E_b$, polarons are expected to be energetically more favorable than the corresponding dimers [2,61,62] and arise naturally for the initially empty final state [7]. Here I will describe how we calculate the resonance positions. Later in chapter 6, I will compare these predictions to our data.

4.1 Calculation of polaron binding energy

A polaron is an impurity immersed in a bath of its environment. Here I mean a spin-down impurity surrounded by a cloud of particle-hole pairs in a spin-up

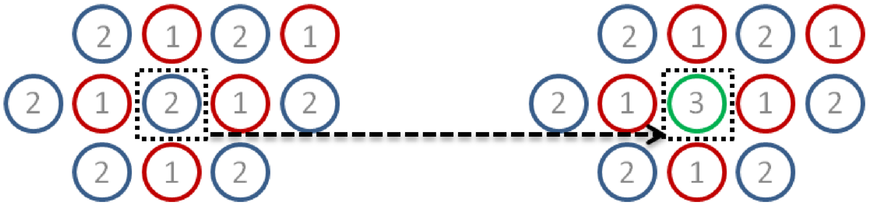

Figure 4.1: Schematic of 12 polaron to 13 polaron transition.

Fermi sea. It arises from collisions between the impurity and atoms in the Fermi sea. Figure 4.1 shows a schematic of 12 polaon to 13 polaron transition. We follow Chevy's three dimensional(3D) calculation of the polaron energy [65] and modify the calculation for a two dimensional(2D) system.

Let's start with the hamiltonian for a dilute two component mixture of fermionic atoms interacting via short range potential $V(\mathbf{r})$. Because of the diluteness of the system, the potential is of short range R compared to the interparticle distance $1/k_F$, we can treat the potential as a δ function as in our treatment of dimers. Then the Fourier transform $V(\mathbf{k})$ of the potential is essentially constant, which we denote here as U_0. In two dimensions, U_0 is the interaction strength, $U_0 = g_0 \frac{\hbar^2}{m}$, where g_0 is dimensionless, so that $\frac{U_0}{A}$ has dimension of energy.

$$H = \sum_{\mathbf{k}_\perp \sigma} \epsilon_{k_\perp} \hat{\mathbf{c}}^\dagger_{\mathbf{k}_\perp \sigma} \hat{\mathbf{c}}_{\mathbf{k}_\perp \sigma} + \frac{U_0}{A} \sum_{\mathbf{k}_{1\perp} \mathbf{k}'_{1\perp} \mathbf{k}_{2\perp} \mathbf{k}'_{2\perp}} \hat{\mathbf{c}}^\dagger_{\mathbf{k}'_{1\perp}\uparrow} \hat{\mathbf{c}}^\dagger_{\mathbf{k}'_{2\perp}\downarrow} \hat{\mathbf{c}}_{\mathbf{k}_{2\perp}\downarrow} \hat{\mathbf{c}}_{\mathbf{k}_{1\perp}\uparrow} \, \delta_{\mathbf{k}_{1\perp}+\mathbf{k}_{2\perp}, \mathbf{k}'{}_{1\perp}+\mathbf{k}'{}_{2\perp}}. \tag{4.1}$$

The first part of the hamiltonian is the total kinetic energy of the individual atom and the second term describes collisions of two atoms with initial momentum $\mathbf{k}_{1\perp} + \mathbf{k}_{2\perp}$ and final momentum $\mathbf{k}'_{1\perp} + \mathbf{k}'_{2\perp}$. The label $\sigma = \uparrow, \downarrow$ denotes the spin states. A is the quantization area of the 2D system for box normalized states and $\mathbf{c}^\dagger$, $\mathbf{c}$ are the usual creation and annihilation operators for fermions with momentum $\mathbf{k}_\perp$ and spin σ.

In this hamiltonian itself, we don't have any information about the polaron. It only describes a system with many-body effects. Chevy proposed a trial wave function for the Fermi polaron with *zero* momentum that captures the essential properties of the polaron [65]. By this polaron state and the Hamiltonian, we can understand the behavior of the polaron. Here is the 2D version polaron state for one impurity spin ↓ atom in a Fermi sea of spin ↑ atoms,

$$|E_{\downarrow}\rangle = \varphi_0|0\rangle_{\downarrow}|FS\rangle_{\uparrow} + \sum_{q_{\perp}<k_{F\perp}<k_{\perp}} \varphi_{\,\mathbf{k}_{\perp}\mathbf{q}_{\perp}}|\mathbf{q}_{\perp} - \mathbf{k}_{\perp}\rangle_{\downarrow}\hat{\mathbf{c}}^{+}_{\mathbf{k}_{\perp}\uparrow}\hat{\mathbf{c}}_{\mathbf{q}_{\perp}\uparrow}|FS\rangle_{\uparrow}. \tag{4.2}$$

In the first term, $|0\rangle_{\downarrow}$ is a spin ↓ impurity with zero momentum, and $|FS\rangle_{\uparrow}$ is Fermi sea state which also have zero momentum. The second term describes a simple interaction between the impurity and the Fermi sea. The impurity knocks a particle with momentum $q_{\perp}$ out of the Fermi sea and creates a hole. At the same time it creates a particle with momentum $\mathbf{k}_{\perp}$ above the Fermi momentum $K_{F\perp}$. This particle-hole pair Fermi sea has momentum $\mathbf{P}_{FS\uparrow} = \mathbf{k}_{\perp} - \mathbf{q}_{\perp}$ and the impurity has momentum $\mathbf{P}_{\perp\downarrow} = \mathbf{q}_{\perp} - \mathbf{k}_{\perp}$ which makes the net momentum of the system is still zero. This state is not the exact eigenstate for a single polaron since it only contains one simple interaction, however it is a good approximation.

In order to find the polaron eigenstate $|E_{\downarrow} \rightarrow$ with energy $E_{\downarrow}$, the expectation value of energy is minimized under variation of the parameters φ_0 and $\varphi_{\,\mathbf{k}_{\perp}\mathbf{q}_{\perp}}$ with the constraint of a constant norm

$$\langle E|E\rangle = |\varphi_0|^2 + \sum_{q_{\perp}<k_{F\perp}<k_{\perp}} |\varphi_{\,\mathbf{k}_{\perp}\mathbf{q}_{\perp}}|^2 = 1. \tag{4.3}$$

The quantity to minimize is $\langle E_{\downarrow}|H|E_{\downarrow}\rangle - E_{\downarrow}\langle E|E\rangle$. The derivation can be found in Chevy's paper [65]. Here we just use his result for the 3D case and transfer it into 2D case by changing the volume of the system V into the area A,

$$E_{\downarrow} = \frac{1}{A}\sum_{q_{\perp}<k_{F\perp}} f(E_{\downarrow}, \mathbf{q}_{\perp}). \tag{4.4}$$

Here

$$f^{-1}(E_{\downarrow}, \mathbf{q}_{\perp}) = \frac{1}{U_0} + \frac{1}{A}\sum_{k_{\perp}>k_{F\perp}} \frac{1}{\epsilon_{\mathbf{k}_{\perp}} - \epsilon_{\mathbf{q}_{\perp}} + \epsilon_{\mathbf{q}_{\perp}-\mathbf{k}_{\perp}} - E}, \tag{4.5}$$

where the bare interaction strength $U_0 = g_0\hbar^2/m$ and g_0 is dimensionless and $\epsilon_{k\perp} = \frac{\hbar^2}{2m}k_{\perp}^2$. We can renormalize the $1/U_0$ using

$$\frac{1}{U_0} = \frac{1}{T_{2B}(k_{\perp 0})} - \frac{1}{2A}\sum_{k_{\perp}} \frac{1}{\epsilon_{\mathbf{k}_{\perp}} - \epsilon_{\mathbf{k}_{\perp 0}}}. \tag{4.6}$$

Here, T_{2B} is physical two dimensional T-Matrix element, obtained from our dimer scattering states

$$T_{2B}(k_{\perp 0}) = \frac{4\pi\hbar^2}{m}\frac{1}{\pi i + \ln(\epsilon_b/\epsilon_{\perp 0})}, \tag{4.7}$$

and $\epsilon_{\perp 0} \equiv 2\frac{\hbar^2}{2m}k_{\perp 0}^2 = 2\epsilon_{k_{\perp 0}}$ is the relative kinetic energy of a colliding atom-pair. We can separate the sum of $k_{\perp}$ in equation 4.6 into two parts $\sum_{k_{\perp}} = \sum_{k_{\perp}<k_{F\perp}} + \sum_{k_{\perp}>k_{F\perp}}$. The $\sum_{k_{\perp}>k_{F\perp}}$ part can combine with the second term in equation 4.5 and the $\sum_{k_{\perp}<k_{F\perp}}$ part can be written as $\frac{1}{A}\sum_{k_{\perp}<k_{F\perp}} \to \frac{1}{A}\frac{A}{(2\pi)^2}k_{\perp}dk_{\perp}d\phi$,

$$\begin{aligned} \frac{1}{2A}\sum_{k_{\perp}<k_{F_{\perp}}} \frac{1}{\epsilon_{\mathbf{k}_{\perp}} - \epsilon_{\mathbf{k}_{\perp 0}}} &= \frac{1}{2A}\frac{A}{(2\pi)^2}\int_0^{k_{F_{\perp}}} \frac{dk_{\perp}k_{\perp}(2\pi)}{\frac{\hbar^2}{2m}(k_{\perp}^2 - k_{\perp 0}^2)} \\ &= \frac{m}{2\pi\hbar^2}\int_0^{k_{F_{\perp}}} \frac{dk_{\perp}k_{\perp}}{k_{\perp}^2 - k_{\perp 0}^2} \\ &= \frac{m}{4\pi\hbar^2} ln\left(\frac{k_{F_{\perp}}^2 - k_{\perp 0}^2}{-k_{\perp 0}^2}\right). \end{aligned} \tag{4.8}$$

Then using equation (4.8) in equation (4.5), we get

$$\begin{aligned} f^{-1}(E,\mathbf{q}_\perp) =& \frac{m}{4\pi\hbar^2}\left[\pi i + \ln\left(\frac{\epsilon_b}{\epsilon_{\perp 0}}\right) - \ln\left(\frac{k_{F_\perp}^2 - k_{\perp 0}^2}{-k_{\perp 0}^2}\right)\right] \\ &+ \frac{1}{A}\sum_{k_\perp > k_{F_\perp}}\left[\frac{1}{\epsilon_{k_\perp} - \epsilon_{q_\perp} + \epsilon_{\mathbf{q}_\perp - \mathbf{k}_\perp} - E} - \frac{1}{2(\epsilon_{k_\perp} - \epsilon_{k_{\perp 0}})}\right] \end{aligned} \tag{4.9}$$

Since $\epsilon_{k_\perp} - \epsilon_{q_\perp} + \epsilon_{\mathbf{q}_\perp - \mathbf{k}_\perp} = \epsilon_{k_\perp} - \epsilon_{q_\perp} + \frac{\hbar^2}{2m}(q_\perp^2 + k_\perp^2 - 2\mathbf{q}_\perp \cdot \mathbf{k}_\perp) = 2\epsilon_{k_\perp} - \frac{\hbar^2}{m}q_\perp k_\perp \cos\phi$ and U_0 should be real, we choose $\ln(-1) = -\pi i$ to cancel the πi term in the first part of f^{-1}

$$\begin{aligned} f^{-1}(E,\mathbf{q}_\perp) =& \frac{m}{4\pi\hbar^2}\left[\pi i + \ln\left(\frac{\epsilon_b}{\epsilon_{\perp 0}}\right) - \pi i - \ln\left(\frac{2\epsilon_{F_\perp} - \epsilon_{\perp 0}}{2\epsilon_{\perp 0}}\right)\right] \\ &+ \frac{1}{(2\pi)^2}\int_{k_{F_\perp}}^{\infty} dk_\perp k_\perp \int_0^{2\pi} d\phi \left[\frac{1}{2\epsilon_{\epsilon_{k_\perp}} - \frac{\hbar^2}{m}q_\perp k_\perp \cos\phi - E} - \frac{1}{2(\epsilon_{k_\perp} - \epsilon_{k_{\perp 0}})}\right] \end{aligned} \tag{4.10}$$

For the first part in the right side of equation (4.10)

$$\ln\left(\frac{\epsilon_b}{\epsilon_{\perp 0}}\right) - \ln\left(\frac{2\epsilon_{F_\perp} - \epsilon_{\perp 0}}{\epsilon_{\perp 0}}\right) = \ln\left(\frac{\epsilon_b}{2\epsilon_{F_\perp}}\right) - \ln\left(\frac{2\epsilon_{F_\perp} - \epsilon_{\perp 0}}{2\epsilon_{F_\perp}}\right). \tag{4.11}$$

We have

$$\begin{aligned} f^{-1}(E,\mathbf{q}_\perp) &= \frac{m}{4\pi\hbar^2}\left\{\ln\left(\frac{\epsilon_b}{2\epsilon_{F_\perp}}\right) - \ln\left(1 - \frac{k_{\perp 0}^2}{k_{F_\perp}^2}\right)\right. \\ &\quad + \frac{4\pi\hbar^2}{m}\frac{1}{(2\pi)^2}\int_{k_{F_\perp}}^{\infty} dk_\perp k_\perp \int_0^{2\pi} d\phi \cdot \\ &\quad \left.\cdot\left[\frac{1}{\frac{\hbar^2}{m}(k_\perp^2 - q_\perp k_\perp \cos\phi - \frac{m}{\hbar^2}E)} - \frac{1}{\frac{\hbar^2}{m}(k_\perp^2 - k_{\perp 0}^2)}\right]\right\} \\ &= \frac{m}{4\pi\hbar^2}\left[\ln\left(\frac{\epsilon_b}{2\epsilon_{F_\perp}}\right) - \ln\left(1 - \frac{k_{\perp 0}^2}{k_{F_\perp}^2}\right) + I\right]. \end{aligned} \tag{4.12}$$

Here

$$I = \frac{1}{\pi} \int_{k_{F_\perp}}^{\infty} dk_\perp k_\perp \left[\int_0^{2\pi} \frac{d\phi}{k_\perp^2 - q_\perp k_\perp \cos\phi - \frac{m}{\hbar^2} E} - \frac{2\pi}{k_\perp^2 - k_{\perp 0}^2} \right]. \tag{4.13}$$

If we let $k_\perp = x k_{F_\perp}$ and $y = q_\perp / k_{F_\perp}$

$$I = \frac{1}{\pi} \int_1^{\infty} dx x \left[\int_0^{2\pi} \frac{d\phi}{x^2 - xy\cos\phi - \frac{E}{2\epsilon_{F_\perp}}} - \frac{2\pi}{x^2 - k_{\perp 0}^2 / k_{F_\perp}^2} \right]. \tag{4.14}$$

Since $\int_0^\pi \frac{du}{1 + a\cos u} = \frac{\pi}{\sqrt{1-a^2}}$; $a^2 < 1$ and $\epsilon \equiv \frac{E}{\epsilon_{F_\perp}}$, $\epsilon < 0$ is the dimensionless polaron binding energy,

$$\begin{aligned} I &= \frac{1}{\pi} \int_1^{\infty} dx x \left[\int_0^{2\pi} \frac{d\phi}{(x^2 - \frac{\epsilon}{2}) - xy\cos\phi} - \frac{2\pi}{x^2 - k_{\perp 0}^2 / k_{F_\perp}^2} \right] \\ &= \frac{2\pi}{\pi} \int_1^{\infty} dx x \left[\frac{1}{\sqrt{(x^2 - \epsilon/2)^2 - x^2 y^2}} - \frac{1}{x^2 - k_{\perp 0}^2 / k_{F_\perp}^2} \right]. \end{aligned}$$

If we let $u = x^2$, $du = 2x\,dx$,

$$I = \int_1^{\infty} du \left[\frac{1}{\sqrt{(u - \epsilon/2)^2 - u y^2}} - \frac{1}{u - k_{\perp 0}^2 / k_{F_\perp}^2} \right]. \tag{4.15}$$

Since $(u - \frac{\epsilon}{2})^2 - uy^2 = (u - \frac{\epsilon}{2} - \frac{y^2}{2})^2 - \frac{\epsilon}{2} y^2 - \frac{y^4}{4}$, let $V = u - \epsilon/2 - y^2/2$ and $G = \frac{\epsilon}{2} y^2 + \frac{y^4}{4}$,

$$I = \int_{1 - \frac{\epsilon}{2} - \frac{y^2}{2}}^{\infty} dV \left[\frac{1}{\sqrt{V^2 - G}} - \frac{1}{V + \frac{\epsilon}{2} + \frac{y^2}{2} - k_{\perp 0}^2 / k_{F_\perp}^2} \right]. \tag{4.16}$$

Since we know $\int \frac{dx}{\sqrt{R}} = \frac{1}{\sqrt{c}} \ln(2\sqrt{cR} + 2cx + b)$ for $R \equiv a + bx + cx^2$, the first part of I can be treated for R with $a = -G$, $b = 0$, $c = 1$, $x = V$. So, $\int \frac{dV}{\sqrt{V^2 - G}} =$

$\ln(2\sqrt{V^2 - G} + 2V)$. Then,

$$\begin{aligned}
I =& \left\{ \ln\left[2\sqrt{V^2-G}+2V\right] - \ln\left[V + \frac{\epsilon}{2} + \frac{y^2}{2} - \frac{k_{\perp 0}^2}{k_{F_\perp}^2}\right]\right\}\Bigg|_{V=1-\frac{\epsilon}{2}-\frac{y^2}{2}}^{\infty} \\
=& \ln(4V) - \ln(V) - \ln(2) \\
&- \ln\left[\sqrt{\left(1-\frac{\epsilon}{2}-\frac{y^2}{2}\right)^2 - \frac{\epsilon}{2}y^2 - \frac{y^4}{4}} + \left(1-\frac{\epsilon}{2}-\frac{y^2}{2}\right)\right] + \ln\left(1-\frac{k_{\perp 0}^2}{k_{F_\perp}^2}\right) \\
=& \ln(2) + \ln\left(1-\frac{k_{\perp 0}^2}{k_{F_\perp}^2}\right) - \ln\left[\sqrt{\left(1-\frac{\epsilon}{2}\right)^2 - y^2} + \left(1-\frac{\epsilon}{2}-\frac{y^2}{2}\right)\right] \qquad (4.17)
\end{aligned}$$

Since $y = q_\perp/k_{F_\perp}$, $\epsilon = E/\epsilon_{F\perp}$,we put I in equation (4.17) back into f^{-1} in equation (4.10) and get

$$f^{-1}(E, q_\perp) = \frac{m}{4\pi\hbar^2}\left\{\ln\left(\frac{\epsilon_b}{\epsilon_{F_\perp}}\right) - \ln\left[\sqrt{\left(1-\frac{\epsilon}{2}\right)^2 - y^2} + \left(1-\frac{\epsilon}{2}-\frac{y^2}{2}\right)\right]\right\}. \qquad (4.18)$$

We can see that f^{-1} is independent of $k_{F_\perp}$ as it should be. Then let's go back to equation (4.4) to calculate the polaron binding energy,

$$\begin{aligned}
E_\downarrow =& \frac{1}{A}\frac{A}{(2\pi)^2}\int_0^{k_{F_\perp}} dq_\perp 2\pi q_\perp f(E_\downarrow, q_\perp) \\
=& \frac{1}{2\pi}\int_0^{k_{F_\perp}} dq_\perp q_\perp f(E_\downarrow, q_\perp) \\
=& \frac{k_{F_\perp}^2}{2\pi}\int_0^1 dy\, y f\left(\epsilon = \frac{E_\perp}{\epsilon_{F_\perp}}, y\right) \\
=& \frac{k_{F_\perp}^2}{2\pi}\frac{4\pi\hbar^2}{m}\int_0^1 \frac{dy\, y}{\ln\left(\frac{\epsilon_b}{\epsilon_{F_\perp}}\right) - \ln\left[\sqrt{\left(1-\frac{\epsilon}{2}\right)^2 - y^2} + \left(1-\frac{\epsilon}{2}-\frac{y^2}{2}\right)\right]}. \qquad (4.19)
\end{aligned}$$

If we set $u = y^2$, we can get a dimensionless expression of polaron binding energy

$\epsilon = \frac{E_\perp}{E_{F_\perp}}$,

$$\boxed{\epsilon \equiv \Sigma(\epsilon) = -2\int_0^1 \frac{du}{-\ln\left(\frac{E_b}{E_{F_\perp}}\right) + \ln\left[\sqrt{\left(1-\frac{\epsilon}{2}\right)^2 - u} + \left(1 - \frac{\epsilon}{2} - \frac{u}{2}\right)\right]}.} \tag{4.20}$$

This equation will determine the zero momentum polaron energy, where E_b is the corresponding dimer binding energy and $E_{F_\perp}$ is the *local* Fermi energy, which is different from the ideal gas Fermi energy that we can determine experimentally from the number of atoms and trap harmonic oscillator frequencies.

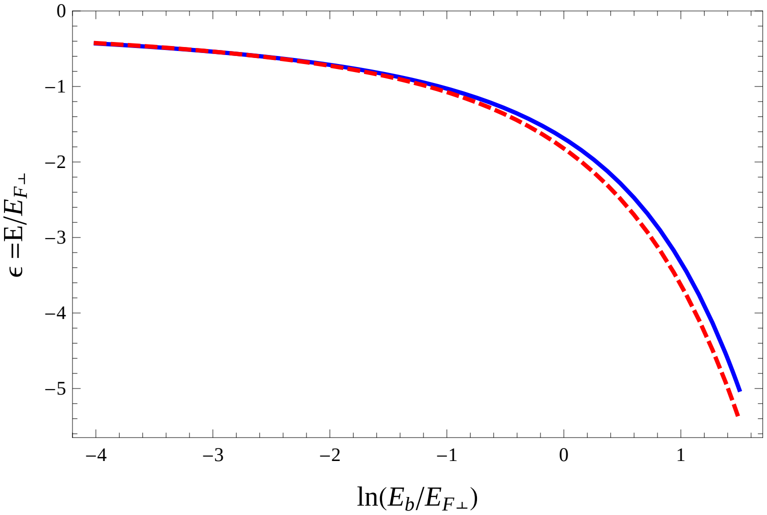

Figure 4.2: Polaron binding energy. Dimensionless $\epsilon = E/E_{F_\perp}$ versus $\ln(E_b/E_{F_\perp})$ where E_b is the dimer binding energy and $E_{F_\perp}$ is the local Fermi energy. The blue solid line is plotted based on equation 4.20 and the red dashed line is based on the approximate expression given in the paper [66] $E_p = \frac{-2E_{F_\perp}}{\ln\left[1+2\frac{E_{F_\perp}}{|E_b|}\right]}$.

4.2 Approximate equation for polaron binding energy and quasiparticle weight

In Figure 4.2, ϵ versus $\ln(E_b/E_{F_\perp})$ is plotted as a blue solid line based on equation (4.20). In paper [66], an approximate equation for the polaron binding energy and $E_b/E_{F_\perp}$ is given, which has simple form,

$$E_p = \frac{-2E_{F_\perp}}{\ln\left[1 + 2\frac{E_{F_\perp}}{|E_b|}\right]}. \tag{4.21}$$

Here, E_p is the polaron binding energy. I also draw it in Figure 4.2 by using red dashed line.

From the figure, we can see that where $\ln(E_b/E_{F_\perp})$ is less than 0, ϵ calculated from equation (4.20) and equation (4.21) are very close. In Table 4.1 and Table 4.2, I list the dimer binding energy E_b and polaron binding energy E_p we calculated for 12 and 13 mixtures for different magnetic fields. When the magnetic field is around 834 G which corresponds to Feshbach resonance of 12 mixture, both $\ln(E_b^{12}/E_{F_\perp})$ and $\ln(E_b^{13}/E_{F_\perp})$ are indeed less than 0. So, the approximate analytical form of polaron binding energy, equation (4.21) is precise enough to be used around 834 G and it has relatively concise form, which can help us understand how polaron binding energy E_p affected by other parameters easier. In equation (4.21), when $E_{F_\perp} \ll |E_b|$, $E_p \to -E_b$. We can see the same trend as E_b becomes bigger in Table 4.1 and Table 4.2. Physically, when the dimer binding energy is so big that the two atoms involved in the interaction can not see the interactions with other atoms very well, the polaron binding energy tends to become the dimer binding energy and many body effects are surpressed. So, the dimer

Table 4.1: Polaron binding energy for ν_z around 24 kHz. Frequencies and energies are given in units of kHz. E_p is a polaron binding energy while E_b is the corresponding dimer binding energy. $E_{F_\perp}$ is the local Fermi energy here. We assume $E_{F_\perp} = \lambda_1 \cdot E_{F_{meas}}$ while $E_{F_{meas}} = h\nu_\perp \sqrt{N}$ is the ideal gas global Fermi energy we determine from the total number of atoms N_{atom} and the trap oscillation frequency $\nu_\perp$. Here $\lambda_1 = 0.67$.

B(G)	ν_z	$E_{F_\perp}$	E_b^{12}	$\ln\left(\frac{E_b^{12}}{E_{F_\perp}}\right)$	E_p^{12}	E_b^{13}	$\ln\left(\frac{E_b^{13}}{E_{F_\perp}}\right)$	E_p^{13}	$E_b^{12} - E_b^{13}$	$E_p^{12} - E_p^{13}$
718.5	26.0	26.2	145.3	1.71	158.4	2.91	-2.19	17.6	142.3	140.8
728.5	24.5	24.6	110.8	1.50	124.0	2.13	-2.45	15.4	108.7	108.6
748.0	25.0	29.8	65.9	0.79	84.7	1.58	-2.94	16.3	64.3	68.4
768.2	24.5	25.7	37.8	0.39	55.0	1.21	-3.05	13.7	36.6	41.3
788.5	24.5	27.5	21.7	-0.24	40.7	1.03	-3.29	13.8	20.7	26.8
808.6	24.0	29.6	12.6	-0.86	32.4	0.88	-3.52	14.1	11.7	18.3
832.2	24.5	27.5	7.25	-1.33	24.7	0.81	-3.52	13.1	6.44	11.6
841.7	24.5	25.8	5.91	-1.47	22.0	0.78	-3.49	12.4	5.13	9.65

binding energy should be the limit of polaron binding energy when $E_{F_\perp} \ll |E_b|$. In Table 4.1 and Table 4.2, we can not measure local Fermi energy $E_{F_\perp}$ directly. We just assume $E_{F_\perp} = \lambda_1 \cdot E_{F_{meas}}$ where $E_{F_{meas}} = h\nu_\perp \sqrt{N}$ is the ideal gas global Fermi energy we can measure in the center of the gas. λ_1 is a single parameter which we use to fit our data by using the polaron binding energy. As you can see in the experimental chapter, this single parameter fitting works very well around the 12 Feshbach resonance when we choose λ_1 to be 0.67.

Another thing which is worth mentioning is the polaron quasiparticle weight:

$$Z \equiv |\varphi_0|^2 = \left[1 - \frac{\partial \Sigma(\epsilon)}{\partial \epsilon}\right]^{-1}_{\epsilon = \frac{E_\downarrow}{E_{F_\perp}}} \tag{4.22}$$

For rf transitions between impurity states 2 to 3 in a bath of atoms in state 1, the momentum of the impurity does not change. We therefore assume the coherent

Table 4.2: Polaron binding energy for ν_z around 82.5 kHz. Frequencies and energies are given in units of kHz. E_p is a polaron binding energy while E_b is the corresponding dimer binding energy. $E_{F_\perp}$ is the local Fermi energy here. We assume $E_{F_\perp} = \lambda_1 \cdot E_{F_{meas}}$ while $E_{F_{meas}} = h\nu_\perp\sqrt{N}$ is the ideal gas global Fermi energy we determine from the total number of atoms N_{atom} and the trap oscillation frequency $\nu_\perp$. Here $\lambda_1 = 0.67$.

B(G)	ν_z	$E_{F_\perp}$	E_b^{12}	$\ln\left(\frac{E_b^{12}}{E_{F_\perp}}\right)$	E_p^{12}	E_b^{13}	$\ln\left(\frac{E_b^{13}}{E_{F_\perp}}\right)$	E_p^{13}	$E_b^{12} - E_b^{13}$	$E_p^{12} - E_p^{13}$
688.9	82.5	75.7	345.3	1.52	385.5	24.3	-1.14	73.6	321.0	311.9
718.5	81.5	80.5	173.4	0.77	224.5	13.5	-1.79	61.6	160.0	163.0
728.5	82.5	79.8	140.4	0.56	192.7	11.9	-1.90	58.8	128.5	133.9
748.0	83.5	81.4	93.6	0.14	149.2	9.75	-2.12	55.9	83.9	93.3
768.2	82.5	97.1	64.1	-0.42	130.8	8.13	-2.48	60.1	55.9	70.7
788.5	82.5	99.1	44.7	-0.80	111.3	7.11	-2.63	58.8	37.5	52.5
808.6	85.0	79.9	33.1	-0.88	86.5	6.69	-2.48	49.4	26.4	37.0
832.2	82.0	88.7	23.7	-1.31	80.4	5.79	-2.73	51.3	18.1	29.1
841.7	82.5	92.6	21.4	-1.46	79.4	5.66	-2.79	52.6	15.8	26.7

part of the spectrum is given by

$$I(\hbar\omega) = Z_2 Z_3\, \delta[\hbar\omega - E_{p3} + E_{p2}], \tag{4.23}$$

Where $Z_2 Z_3 = |\varphi_{03}^* \varphi_{02}|^2$ is the square of the overlap integral between the part of the initial and final polaron states that yields the coherent part of the spectrum. The product of the quasiparticle weights for the 1-2 and 1-3 polarons determine the strength of the transition. Figure 4.3 shows the quasiparticle weight Z versus $\ln(E_b/E_{F_\perp})$. As I mentioned previously, we are working in the region where $\ln(E_b/E_{F_\perp})$ is smaller than 0. Z in this region is quite large. Especially, around 834 G, we find both Z_2 and Z_3 are close to unity based on the data in Table 4.1 and Table 4.2. Hence, we expect that the overlap between the initial and final polaron states is strong and that transitions between polaron states should make an important contribution to the spectrum.

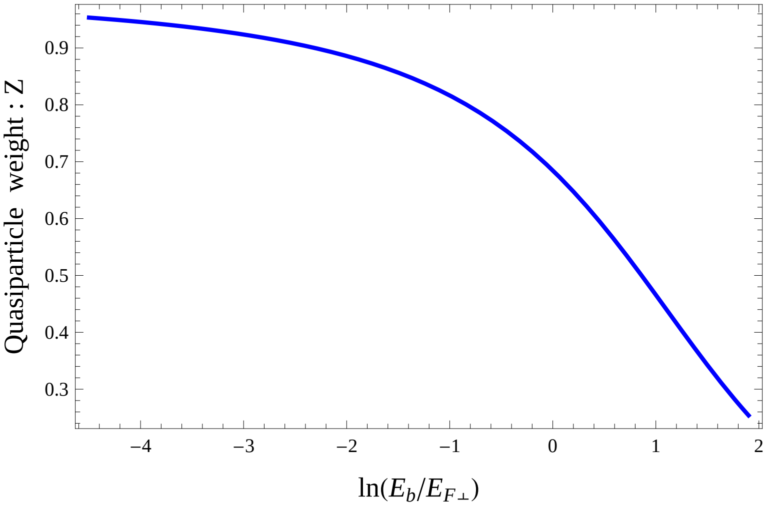

Figure 4.3: Polaron quasiparticle weight versus $\ln(E_b/E_{F_\perp})$ where E_b is the dimer binding energy and $E_{F_\perp}$ is the local Fermi energy.

Chapter 5

Experimental Methods

In this chapter, I first talk about my understanding of the basic experimental methods. Then I introduce what is new in setup of quasi-two dimensional optical traps. Last but not least, I will talk about the method of measuring experimental parameters. Some interesting results of the parametric resonance experiment would be shown as well.

5.1 Basic experimental procedure

Since we do experimental physics, the most important thing for us is to find a way to realize our plans in the lab which includes setting up and manipulating the apparatus. Understanding the methods and principles of the experiment is the key point to do trouble shooting on a daily basis and making the whole system work reliably.

Simply speaking, all the experiments we are doing in the lab require three steps: atom sample preparation, designed experimental probing and resulting signal collection. We use computers to control the whole process automatically. One cycle of an experiment can be done within one minute. We can repeat the same experiment or change parameters for each cycle easily. The short time scale of one cycle also allows us to finish a set of experiment cycles within a reasonable time over which the experimental environment does not change too much.

The atom sample preparation and resulting signal collection are usually the same or very similar for different experiments, while the experimental probings are quite different. I will introduce basic experimental methods and techniques along with each of them and list some experiments I have been done to show the versatility and limitations of our system.

5.1.1 Atom sample preparation

The atom sample preparation requires: producing a hot atom beam from an atom source, and cooling down and trapping atom samples.

Since the Fermi atom we are using, ^{6}Li, is solid in the room temperature, we can safely keep it inside the vacuum system when it is not in use. We connect a little thumb sized oven bucket to the vacuum system which holds about 2 grams of lithium. A little bit goes a long way. This amount can last for more than 4 years of everyday use. When we need to use the atoms, we make them evaporate into a gas by heating the bucket up to about $400°C$. The hot gas will go through a small hole on the side of the bucket, which connects to a long stainless metal tube nozzle to form a hot atom beam moving toward the main chamber where we trap atoms.

Our ultimate goal is to decelerate the fast moving atoms and make them stand still in the main chamber area in order to realize cooling and trapping. We use three steps to reach that goal. First, along the direction that the hot atoms fly, we have a Zeeman slower, which can significantly decelerate atoms (2×10^6 m/s^2) in the direction along the nozzle to the main chamber area and make them slow enough to be trapped in the magneto-optical-trap (MOT), which is our second step. The MOT is located in the center of main chamber area and is formed by a pair of anti-Helmholtz coils and six laser beams red detuned with respect to D2 line of ^{6}Li. It slows down atoms in all directions to the Doppler limit of 140 μK as they enter the MOT area. A MOT slows and traps atoms in a manner similar to molasses. We have "optical' molasses here. Consult previous dissertations in this group for more details about Zeeman slower and MOT [67, 68]. Although slowed in the optical molasses, the atoms still have an opportunity to walk away from the MOT area by random walking. And due to the existence of Doppler limit, we need to cool them down much further to reach degeneracy. So next, we let atoms collide and evaporate in a container formed by an optical trap, which is our third step. The collision interaction between atoms makes some of them have higher energy than the others. In the evaporation, atoms with energy higher than the container's edge escape from the trap, leaving atoms with lower energies trapped inside the container. The optical trap which we use as the container is formed by focusing a powerful CO_2 laser beam and the focal point is located inside the MOT. We call it far off-resonance dipole trap (FORT). Here we use a Feshbach resonance to increase the interaction between atoms to enhance collisions, which makes the evaporation more efficient. We artificially lower the edge of the container to let more atoms with relatively higher energies escape. We call this method forced evaporation. After evaporation, the atoms can be cooled down to the order of 10 to 100 nK.

When we are working with 1-2 mixture, we normally do evaporation at the Feshbach resonance around 834 G where atoms have a very strong interactions. Then we smoothly shift magnetic field to wherever we want the experiment to take place. By using this method, we can get reasonably cold samples for a magnetic field range from 720 G up to 1200 G for 1-2 mixtures. Actually, when we switch the magnetic field to the BEC region after evaporation, we see a heating of the atoms. The lower magnetic field we switch to, the bigger the heating effect can be. If we go lower than 720 G the heating is so serious that atom sample can not be used for cold experiment any more. 1200 G is the upper limit of our high field magnet system, which is formed by a pair of water-cooled coils. For the experiments that need to be done in a lower magnetic field, like 528 G, where the s-wave scattering length of 12 mixture is zero, and the interaction between atoms is zero, we do the evaporation at around 300 G, where there are interactions between atoms, and then move upward to 528 G to avoid heating. There is a narrow Feshbach resonance for 1-2 mixture around 544 G [69], which we normally avoid when shifting the magnetic field after evaporation, since that also causes heating.

If we do experiments with 1-3 mixtures, we also start with a 1-2 mixture sample. Instead of doing evaporation in the 1-2 mixture, we use rf transitions to transfer all the atoms in state 2 into state 3 around 528 G and then do evaporation around the Feshbach resonance of the 13 mixture at 690 G to cool down the sample.

After these three steps of cooling and magnetic field shift, we end up with cold degenerate atom samples in the magnetic field where we want to do the experiment.

The all-optical approach we used in our experiments is ideally suited to exploring atomic gases with magnetically tunable interactions. We use two kinds of laser beams to realize cooling and trapping. One is a resonant red beam $\lambda = 671nm$ for

Zeeman slowing and for the MOT. The other is an infrared beam of the far off-resonance optical trap(FORT). The red beams are from a single dye laser, which has output power around 800 mW. This is a multi-purpose beam. We split its output into several pieces to form the MOT, to serve as the beam going through Zeeman slower, which we call the slowing beam, and the beam to create absorbing imaging, which we call the camera beam. The infrared beam is from a very powerful CO_2 laser, which is more than 50 W when it reaches the main chamber. We only use these two lasers to complete all steps of a typical experiment. This makes our experimental setup very simple. However, both of the lasers have some disadvantages. Although the dye laser is powerful enough for everything we need, it is not very stable, since it is very sensitive to the change of room temperature and vibrations. Relocking the dye laser during the day several times is inevitable. The CO_2 laser is invisible and quite strong, so that it can easily burn a person's hand when the size of the beam is small. That makes the alignment of the CO_2 laser is very challenging.

5.1.2 Designing experimental probes

After preparing the cold atom sample, we can start doing the real experiment. This part of the cycle is the most exciting and creative one, since for different experiments we need to come up with different plans to realize our measurement and modify software and hardware to physically make the cycle run correctly and smoothly. Let's take a look at some simple experimental sequences after sample preparation.

For rf spectroscopy experiments, we use one digital signal to trigger an rf function generater and send a pulse through an antenna inside the vacuum chamber to excite rf transitions. As I mentioned earlier, the pure transition between two hyperfine energy levels is used to calibrate the magnetic field. And the transitions in ultracold atom mixtures give us very interesting spectra, which I discuss in this dissertation.

For parametric resonance experiments, we add perturbation oscillation frequency (order of kHz) from a function generater to the CO_2 laser amplitude in order to modulate the optical bowl holding the atoms. When the oscillation frequency matches twice the internal frequency of the trap, the resonance will continuously excite the atoms to higher energy levels and the heating effect is seen by monitoring the width of the atom cloud. A digital signal is used as a trigger signal to control when and how long the perturbation is added. We use this experiment to characterize the optical trap.

For breathing mode experiments, CO_2 laser amplitude will be decreased quickly and then reincreased to the original level to excite the internal frequencies of the trapped cloud. This is another experiment we use to get the oscillation frequencies of atoms in the trap. The amplitude change accomplished with an analog signal and generated by a function generator, triggered by a digital signal. Each of these three experiments can be used as one part of more complicated experiments as far as we organize the time sequence well.

So, the control of our system is actually a number of digital and analog signals organized by following a certain time sequence. These signals are applied to different parts of the system. In our lab, we control the system from a computer by sending digital and analog commands. There are many different ways to realize this kind of control as long as the speed and amplitude of the command signal is good enough. In my lab, we use a 32 digital channel computer card, multiplexer, GPIB controls and fast digital delay/ pulse generators to reach the goal. I describe these briefly:

(1) 32 digital channels. The signal directly come from computer through a 32 channel digital card. The digital card can produce either 0 or 5V voltage for each channel. Since the channels are directly powered from the computer, they can not supply high current. We use some of the channels directly as switches and trigger signals in the system. The others are used to select the output of a multiplexer, which controls red laser beam intensities and frequencies. The signal timing accuracy of the 32 channels is 100 μs.

(2) Multiplexer. We are using a home made multiplexer to send most analog signals we need to the system, as well as some digital signal with large current. As I mentioned, some of the 32 digital channels will serve as selection signals to choose an output from several analog and digital input signals of the multiplexer. That means we turn some of the digital commands into analog commands by using the multiplexer. The multiplexer has external power, therefore it can provide large current. Since it is controlled by 32 digital channel, it has the same timing accuracy of 100 μs.

(3) GPIB controls. By using GPIB connecting cord, we directly send analog signals, in addition to the ones from the multiplexer, to the equipment that supports GPIB controls. For example, when we try to lower the trap depth of the CO_2 laser beam in order to increase the efficiency of evaporation, we use GPIB control to send a lowering curve to the function generator, which controls the amplitude of the laser. How fast the GPIB board can transfer data depends on the amount of information we send. It can reach several Mega Bytes per second.

(4) Fast digital delay/ pulse generators. We use several DG535 digital de-

lay/pulse generator from Stanford Research Systems. They have tens of ps delay resolution from channel to channel, which is much better than what we need (around $1\mu s$). We use these to control the parts of time sequence that need high accuracy in the experiment, like absorption imaging.

Our group also has another lab using an upgraded 24 digital channel computer card which is faster, 8 analog channels and GPIB controls to control the experiments. Although the equipment is different, the principles for the control are the same.

The software program I have been using to compile the commands in the computer is Labview, while the other lab in our group is now using Matlab. For different experiments, we change the time sequences for each signal channel directly in the computer and use software program to compile the information and send it to the 32 channel computer card and GPIB control system.

5.1.3 Signal collection

For almost all of our experiments, we use a CCD camera to take absorption images of the atom cloud for data collection. At the end of the experiment, we turn off the trap and let the atom cloud expand for a short time in order to reach a size that is large enough to be taken by our camera system. A small portion of red beam from dye laser is used as the so called camera beam that will shine directly on to the camera through the atom cloud. The camera takes a shadow image of the atom cloud. And at the same time, atoms absorb photons from the beam and gain energy to fly away. We take one shot immediately after the camera beam is shined on the cloud, which contains the shadow of atoms and the background. Then we wait until the atoms disappear ($30ms$) to take another shot of only the reference beam. Subtraction of these two images is the raw image of atoms. Our CCD detector consists of a 1024 × 1024 array of high resolution pixels measuring 13 μm on each side. But the real resolution of our image depends on the lens system in front of the CCD detector which we are trying to improve. Hopefully in the near future, we will use increased resolution to take in situ images for a 2D system.

The imaging part is the same for different experiments. Then we analyze data images by using the software program Igor to fit the column density and determine the information we want. Normally, we want to monitor either the shape change of the atom cloud or the change of the atom number. For example, in the rf spectroscopy experiments, we monitor atom number in a certain hyperfine state and the largest change of atom number corresponds to the resonant rf frequency. For parametric resonance experiments, we monitor the width of atom cloud in a certain direction after excitation and the largest width corresponds to a perturbation frequency which is resonant.

5.2 Quasi-2D optical trap set up

The uniqueness about my work is that the system is quasi-two dimensional. In order to create quasi-two dimensional Fermi gas, we modify the optical layout of CO_2 laser beam in two places labeled in Figure 5.1. Figure 5.1 is the optical layout for generating a three dimensional CO_2 laser optical trap, which can be found in Bason's dissertation [70], who built our lab with Le [71]. The names of optics have been labeled in the figure and all optics in the CO_2 laser path are made out of zinc-selenide.

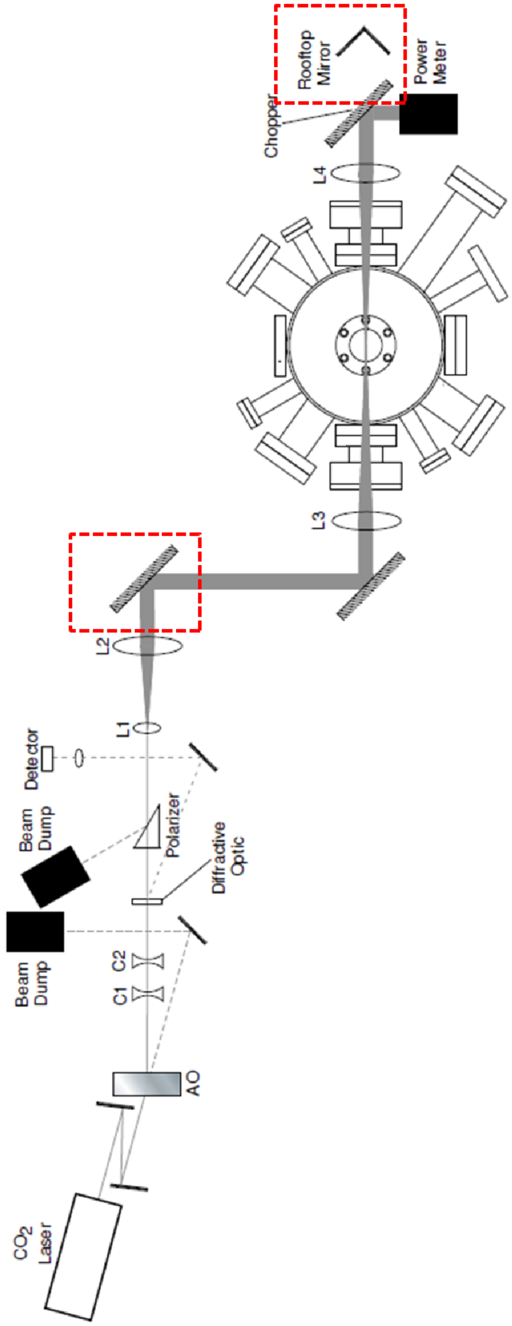

Figure 5.1: Optical layout for generating the CO$_2$ laser beams. In order to realize quasi-two dimensional trap, we make two changes in the optical layout for three dimensional trap highlighted by using red dash squares. The original layout is from Bason's dissertation [70].

In the layout of three dimensional optical trap, after coming out of the laser source, the CO_2 laser beam goes through an acousto-optic modulator(AO) which can fast shift light frequency using sound waves, at the same time shift the direction of propagation by a small angle to the first order of the beam from the original direction which is the zero order. By changing the amplitude of the sound waves, we can control the amplitude of the laser beam in the first order. Then, the vertical and horizontal curvatures of the first order laser beam would be adjusted to the same by using two cylindrical lenses, C_1 and C_2 in Figure 5.1. Before expanding through a telescope formed by lenses L_1 and L_2, the laser beam would go through a thin film polarizer. This polarizer is used to protect the laser source by reflecting the back going laser beam to a beam dump. The polarization of this back going beam has been rotated by 90 degree using a rooftop mirror on another side of the chamber.

In quasi-two dimensional trap layout, we create CO_2 laser standing wave by reflecting beam directly back without changing polarization by using a mirror instead of the rooftop mirror. We still need to protect the laser source by reflecting the back-going beam out to the beam dump. Therefore, we replace one of the big mirror in the beam path into a special mirror with $\lambda/4$ phase retarding coating which can rotate light polarization by 45 degree with plane polarized light at 45 degree to the plane of incidence. The beam polarization would be rotate once again to the same direction 45 degree when it goes back, which add up to 90 degree to be reflected out to the beam dump by the thin film polarizer.

To align the backing going CO_2 laser beam perfectly match the incoming beam and make the standing wave trap stable in a big challenge. In Figure 5.2, the 3D and 2D trap shapes are shown. We measure the axial trap frequency in the

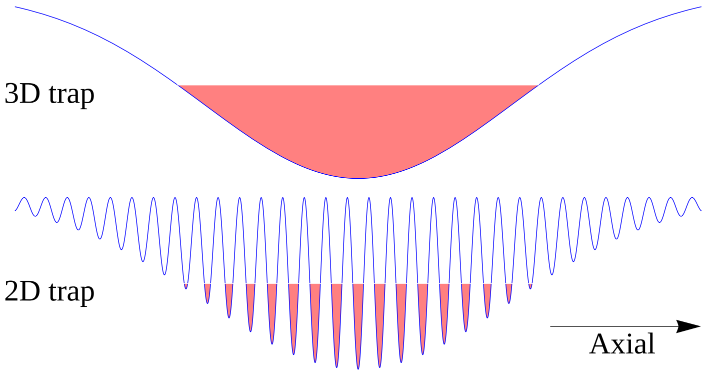

Figure 5.2: Schematic of 3D and 2D traps along axial direction. Radial direction is perpendicular to axial direction. Here I use blue curve to show the potential shapes and pink area to show how atoms fill in the potentials.

quasi-two dimensional traps after alignment, which is supposed to be twice as the radial trap frequency in the single beam trap, by using parametric resonance which I will talk later. In our case, the ratio can be more than 1.9, which shows a very good alignment considering the energy loss in the beam path.

5.3 Measurement of experimental parameters

I want to mention other experiments we need to do along with the radio frequency spectroscopy experiment in order to get the information we need to complete our research. Some of the experiments I have already mentioned previously in this dissertation, like magnetic field calibration and Rabi frequency measurement. Here I will emphasis the reason we do them once again.

5.3.1 Magnetic field calibration

As we mentioned in the end of subsection 2.2.2, we can accurately calibrate the magnetic field of the system by using radio frequency spectroscopy. This is the experiment we need to do daily and with any other experiments in different magnetic field, since it can give us the accurate magnetic field to calculate parameters we need in the data analysis.

5.3.2 Rabi frequency measurement

I also mentioned Rabi frequency measurement in the same chapter, subsection 2.2.1. This is another important experiment we need to do in advance. Comparing with calibration of magnetic field, we do not need to check Rabi frequency every day as long as the setup is the same. The Rabi frequency will help us decide the time duration and intensity of the radio frequency pulse we should use in the experiment.

5.3.3 Trap frequency measurement : Parametric resonance

To characterize the trap, we precisely measure the harmonic oscillation frequencies each day, since they may change slightly from day to day based on the CO_2 laser alignment and power. There are several ways to get the trap frequencies. We normally use parametric resonance [68].

We know that there should be three different resonant frequencies for the x, y, z axes of the trap. In our quasi-2D trap, the axial direction (z direction) is tightly confined and the radial direction, x, y directions, are symmetric and relatively loosely confined as shown in Figure 5.2.

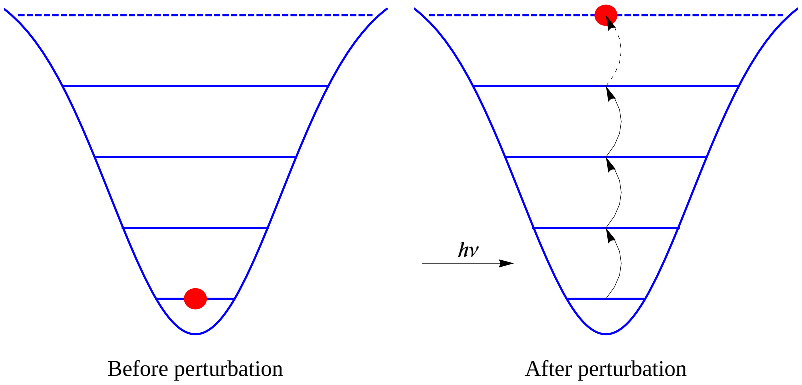

Figure 5.3: Principle of parametric resonance. The red disk represents one atom. Before the perturbation, it is sitting in the ground state of a certain direction. When the perturbation $h\nu$ matches the energy level spacing, the atom can continuously absorb photons and jump to higher energy level.

The experimental procedure is as follows. After preparing the sample of ultracold atoms, we add a perturbation with frequency ν into the trapping CO_2 laser intensity in order to excite the trap resonant frequencies. It normally in the order of kHz which is very small compared with the CO_2 laser frequency (28.3 THz). When we scan ν, if ν matches one of the trap parametric resonant frequencies, the atoms in the trap will be excited and continuously jump to the higher energy level in that direction as Figure 5.3 shows. We can easily observe this kind of excitation by measuring the width increases of the atomic cloud in that direction after turning off the CO_2 trap, since the width of the cloud is determined by the atom energy in that direction. This is the principle of parametric resonance.

In our quasi-2D system, the expansion of the axial direction for each pancake is very fast and impossible to see, since the axial width is much smaller than $1\mu m$. But as long as interaction between atoms in the sample is large enough, the energy excitation in one direction can be transferred to other directions by

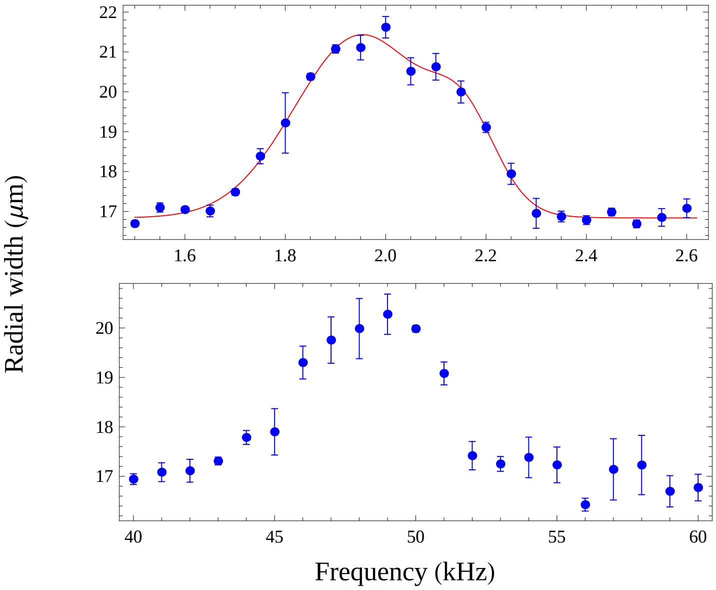

Figure 5.4: Radial and axial parametric resonance for quasi 2D 1-2 mixture at 300G with trap depth $h\nu_z = 25$ kHz. The clouds are allowed to expand ballistically to a bigger size at 528 G in order to take the image of the densiy profile. The red solid line is the fit using two Gaussian profiles $f(x) = y_0 + A_1 e^{\frac{-(x-x_1)^2}{{w_1}^2}} + A_2 e^{\frac{-(x-x_2)^2}{{w_2}^2}}$ with $w_1 = 187.65$ Hz, $w_2 = 91.75$ Hz.

collisions. So, we can observe the expansion in radial direction as well when ν matches the resonant frequency in axial direction. In Figure 5.4, we have 50-50 1-2 mixture atom sample and both radial and axial parametric resonance are observed by measuring the radial width change of atom cloud at around 300 G.

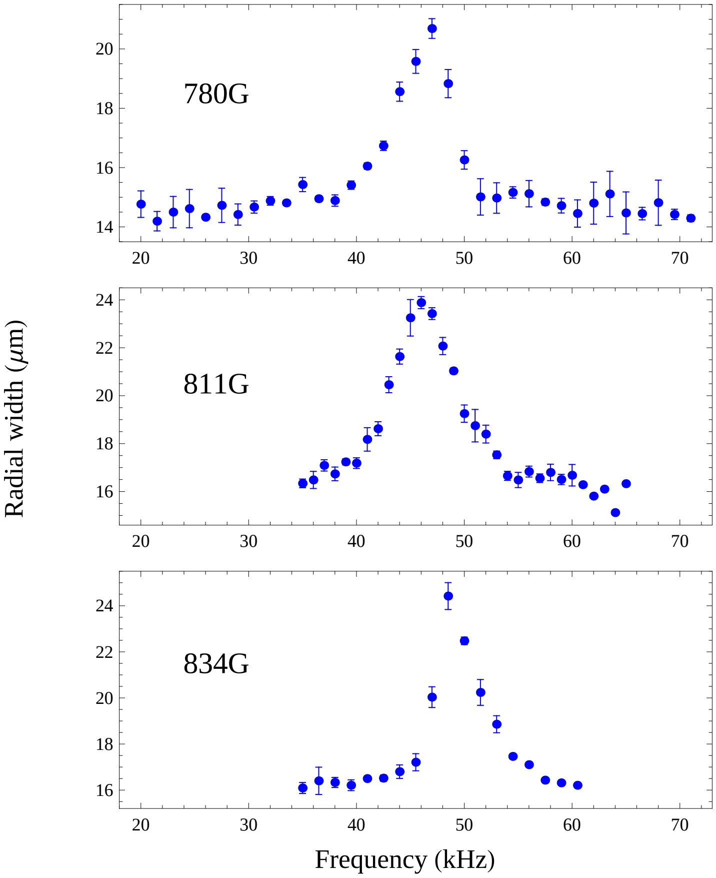

Figure 5.5: Axial parametric resonance for quasi 2D 12 mixture observed through radial width expansion for 780G, 811G and 834G at 2% trap depth. The clouds are allowed to expand to a bigger size at the corresponding magnetic field in order to take picture. We notice significant change of the peak shapes for different magnetic fields.

The parametric resonance is a quite interesting experiment itself. We do the same experiment for 50-50 1-2 mixture at different magnetic field and notice the shape of the resonance peak varies with change of magnetic field. In Figure 5.5, I show three axial parametric resonance data in different magnetic fields from BEC region to around Feshbach resonance. We notice significant change of the peak shapes. The 780 G one has a sharp edge on the right side while the 834 G one has a sharp edge on the opposite side. We still do not yet understand the mechanism of this shape change.

5.3.4 Determining the bare atomic transition frequency

As I mentioned previously, we need to determine the bare atomic transition frequency while we do the rf spectroscopy experiments for a certain magnetic field. We need to check for mean field shift in its location.

Let's take a 12 to 13 rf transition experiment for example. We measured the pure 2 to 3 transition without atoms in state 1 in advance to determine where is the real atomic transition frequency without mean field shift. This is actually the magnetic field calibration. We also do the 12 to 13 transition in a hot mixture of 1-2 atoms where there are almost no atom pairs and we should only see the bare atomic transition peak in the spectrum. We also change the trap depth of the system from 2% (ν_z =24 kHz) to 100%(ν_z =180 kHz) in 12 to 13 rf transition experiments for shift in the location of the atomic transition peak in the spectrum. We notice that the atomic transition frequency lines up with the left side peak in the spectra and there is almost no change for different trap depth and temperature. Figure 5.6 and 5.7 are the data for different trap depth. Hence for our experiments, we conclude that the mean field shift of the bare-atom transition frequency is negligible. So we can use it as a reference point.

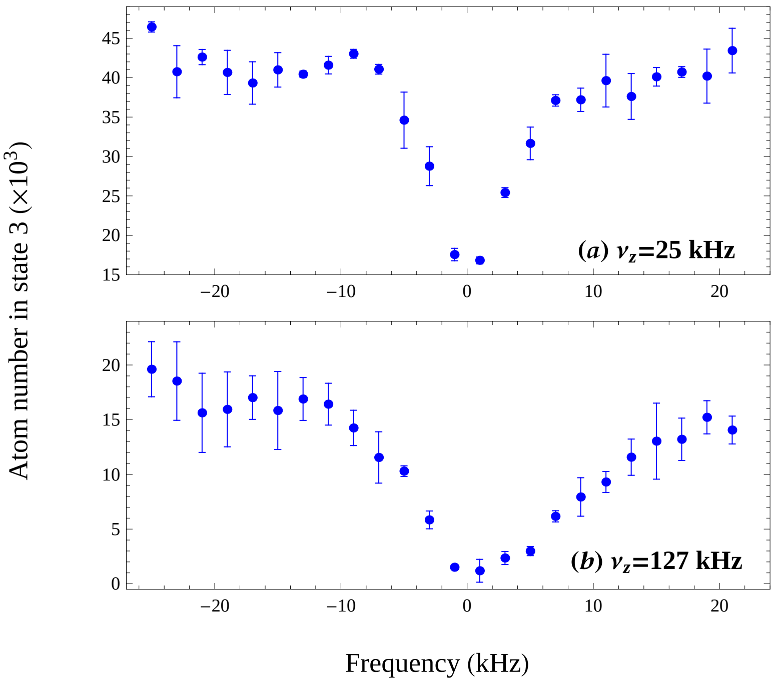

Figure 5.6: Atomic transition peaks from 1-3 to 1-2 in different trap depth at 720 G. Origin of x axis is 82.475 MHz.

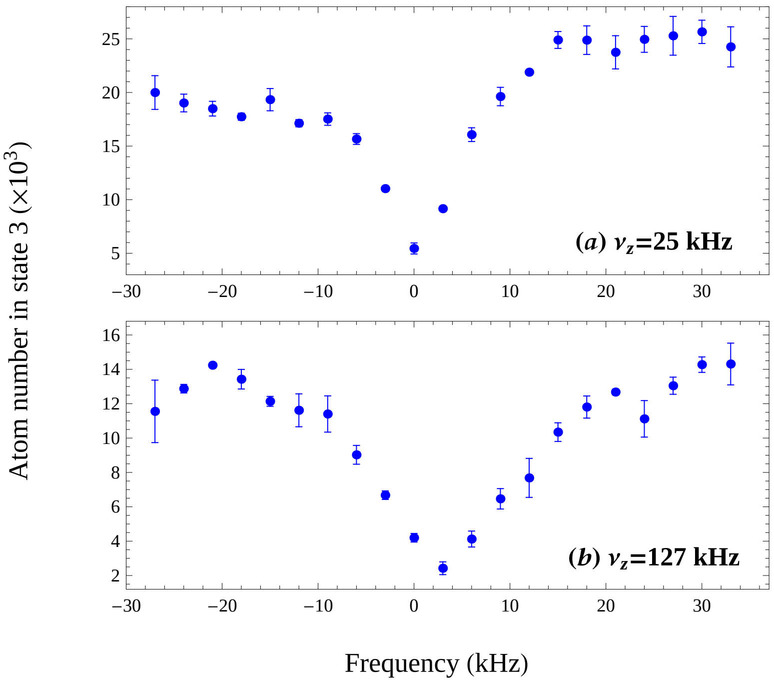

Figure 5.7: Atomic transition peaks from 1-3 to 1-2 in different trap depth at 690 G. Origin of x axis is 82.717 MHz.

Chapter 6

Radio Frequency Experiment

In this chapter I will present all the rf experimental data and compare to the theoretical spectra based on dimer and polaron transitions theories respectively.

We will see that dimer transition theory can not perfectly explain our experimental data. However, we notice that it dose give a reasonable approximation to experimental data when the dimer binding energy is much more bigger than 2D Fermi energy of the system.

For the polaron theory fits, we use the ratio of the local Fermi energy to the ideal gas global Fermi energy in the center of the trap as the only fitting parameter λ_1. This produces us a nice fit to all of the data for a single value of λ_1 $\lambda 1$.

By doing the fitting to the data we can tell which effect dominate our system.

6.1 Dimer transition spectra

We will discuss the fits based on dimer transition theory first. Before we show experimental data, I want to use a set of schematics for transitions among the two-atom energy levels, to show what types of resonances we expect to see in the rf spectra for different experiments. In Figure 6.1, on the left side, single-atom and two-atom energy levels are shown with all the possible rf transitions between

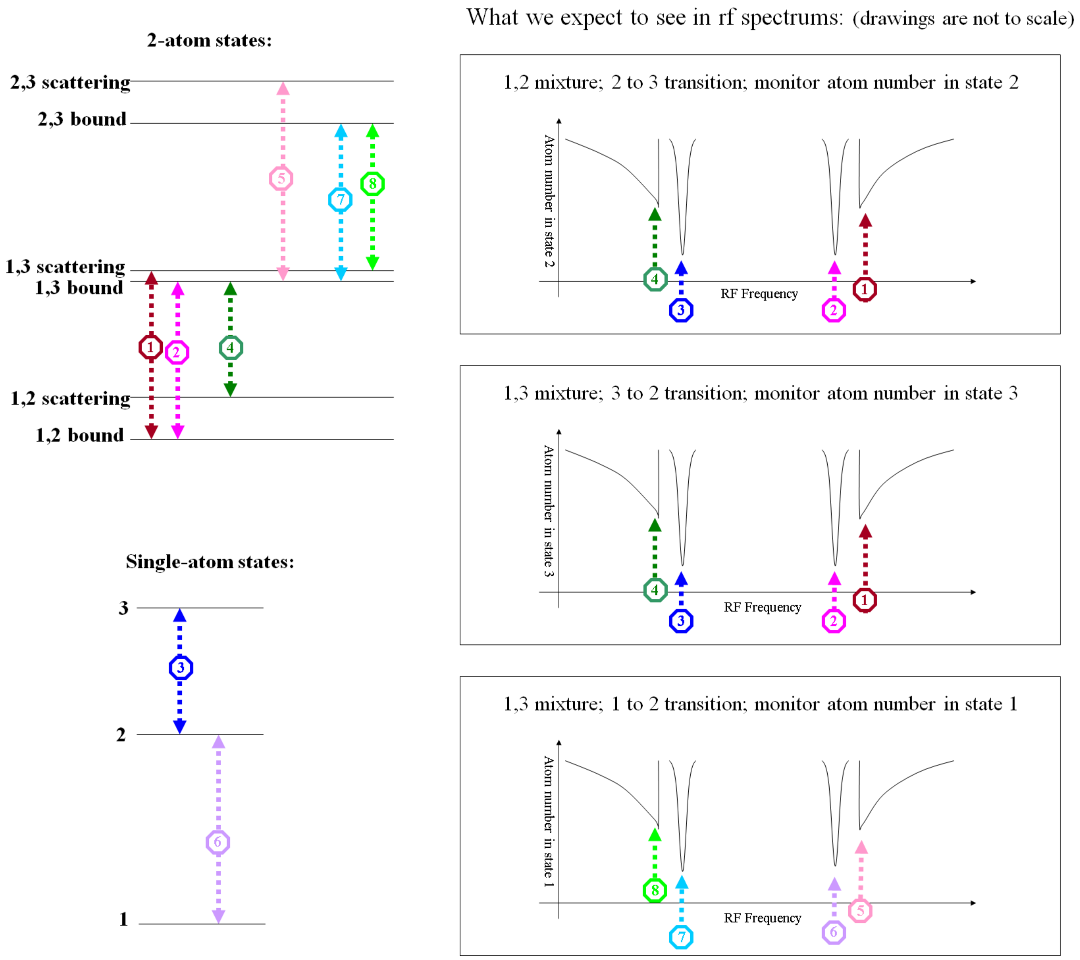

Figure 6.1: Rf transitions between two-atom energy levels. The labeled transitions on the left side correspond to the resonances on the spectra shown on the right side. Here the spectra only show the shapes and relative positions of the resonances. Drawings are not to scale.

them. Here, bare atomic transitions are our references in the spectra. On the right side, I listed three different rf spectra corresponding three different transition sets. In the first spectrum on the top, the rf spectrum for transition from states 1-2 to states 1-3 are shown as the depletion of state 2. Experimentally, we can achieve that by scanning rf frequency near the bare 2 to 3 atomic transition frequency (transition frequency ③ in Figure 6.1). When the rf signal is a π pulse for the coherent case or is much stronger and longer that the time over which become incoherent, we should see resonances (The maximum atom loss) on the spectrum corresponding to transitions between energy levels.

The bare atomic transition resonance is around $70 \sim 85$ MHz. If there is mechanism for bound states to exist, we should see additional resonances for bound states in the spectrum. I label rf transitions on the left and the corresponding spectra on the right side by using arrows and numbers with the same colors. For the second and third spectra, the experiments start from a 1-3 atom pair. And the rf frequency range we use are around 3 to 2 atomic transition resonant frequency (transition frequency ③ in Figure 6.1) for the second spectrum and around 1 to 2 atomic transition resonant frequency (transition frequency ⑥ in Figure 6.1) for the third spectrum. The drawings of spectra are not to scale. I only use it to show the shapes and relative position of each peak based on dimer transition theory. As we mentioned in the dimer theory, the bound to scattering state transition resonance should have a threshold shape and a long tail caused by kinetic energies, while the bound to bound transition resonance should be quite symmetric.

Based on the schematics, it seems that the shapes of all three spectra are similar. But in the real experimental results they are quite different. Since the transition strengths are different for different transitions, the relative amplitudes of the resonances vary significantly, which will change the shape of the spectrum. Further, in the real experiments, dimer transitions may not dominate and we need to consider other interactions to explain the spectrum, like polaron transition.

Now, let's move on to the real data for all these three experiments and compare with the theoretical predictions initially using dimer theory. For experiments in a 1-2 mixture, we have data range from 720 G to 844 G, while for experiments with a 1-3 mixture, the data range from 670 G to 720 G. I want to group them separately, since for different mixtures, the atoms have quite different initial and final state interactions.

6.1.1 Dimer fits for experiments in 1-2 mixtures

The Feshbach resonance for a 1-2 mixture is around 834 G. We cool down the atoms in the strong interacting region around 834 G by doing evaporation and shift the magnetic field to wherever we need to do the experiment. Below 834 G, on the BEC side, the system can have tightly bound molecular dimers, while around the resonance and even above the resonance the dimer binding energy is quite small compared to the Fermi energy in 2D, as we have seen in Figure 3.3. For example, consider 2% trap depth ($\nu_z = 24.5$ kHz), the 1-2 dimer binding energy vary from around 150 kHz at 720 G to around 5 kHz at 844 G. However, the 2D Fermi energy in our system is nominally the same $E_{F\perp} = 1.5h\nu_z$ while dimer binding energy changes with the magnetic field. This gives us two extreme conditions on the two ends of the magnetic field range we use, from 720 G to 844 G. Around 720 G, the dimer binding energy, E_b^{12}=145.25 kHz, is much larger than the Fermi energy, 38.93 kHz. Around 842 G, the dimer binding energy, E_b^{12}=5.91

kHz, is much smaller than the Fermi energy, 38.52 kHz.

We did not go below 720 G since the heating is serious when shift the magnetic field from 834 G. Although we can go further up into the BCS region, the 2D dimer binding energy for magnetic field higher than 844 G is too small to be resolved in the spectrum.

Tightly bound dimers at 720 G

Let's look at the 720G data first. In Figure 6.2, 6.3 and 6.4, I show two theoretical fits for each of the three different trap depths data, 2%, 20% and 50%, respectively. Since the dimer binding energy is much larger than our 2D Fermi energy, especially for low trap depth, we believe dimer theory should work very well here. The predicted dimer transition spectra we derive in Chapter 3, equation (3.89), (3.90),

$$R_{12b\rightarrow 13b}(\nu) = \pi^2\Omega_{fi}^2\epsilon_{bb}\,\delta\left(\nu - \frac{E_b^{12} - E_b^{13}}{h}\right), \tag{6.1}$$

$$R_{12b\rightarrow 13f}(\nu) = \pi^2\Omega_{fi}^2\frac{E_b^{12}}{h\nu^2}\frac{q^2\Theta(\nu - E_b^{12}/h)}{\left[q - ln\left(\frac{h\nu}{E_b^{12}} - 1\right)\right]^2 + \pi^2}, \tag{6.2}$$

and the bound to bound transition fraction, (3.75)

$$\epsilon_{bb} = \frac{E_b^{12}E_b^{13}}{(E_b^{12} - E_b^{13})^2}\left[ln\left(\frac{E_b^{12}}{E_b^{13}}\right)\right]^2 = \frac{q^2}{4\sinh^2(q/2)}. \tag{6.3}$$

are used to fit the data. Here $q = ln\left(\frac{E_b^{13}}{E_b^{12}}\right)$

For 2% trap depth data, we notice the bound to bound transition fraction $\epsilon_{bb} = 0.27$, and bound to scattering state transition should dominate. If we only include the bound to scattering state transition in the fitting, the theoretically predicted spectrum matches the real spectrum quite well as shown by the red solid line in

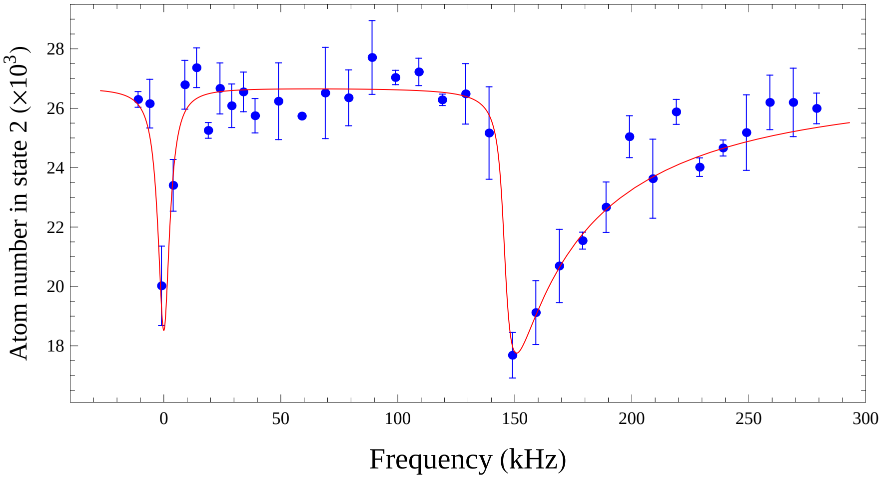

(a) Fit to the data contains only dimer bound state to scattering state transition. The broadening of the resonance on the right is as small as the broadening of the atomic transition resonance on the left.

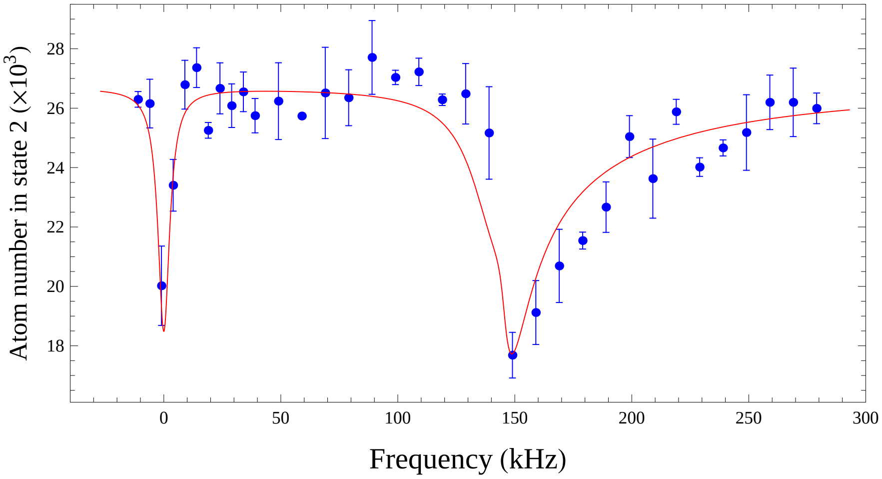

(b) Fit to the data contains both dimer bound state to scattering state transition and bound to bound transition. Bound to bound transition fraction $\epsilon_{bb} = 0.27$.

Figure 6.2: Dimer theory fits of 12 to 13 rf transition spectrum at 718.5 G for 2% trap depth with $\nu_z = 24.5$ kHz (red curves). The origin of the x axis corresponds to the bare 2 to 3 atomic transition frequency for 718.5 G, 82.472 MHz.

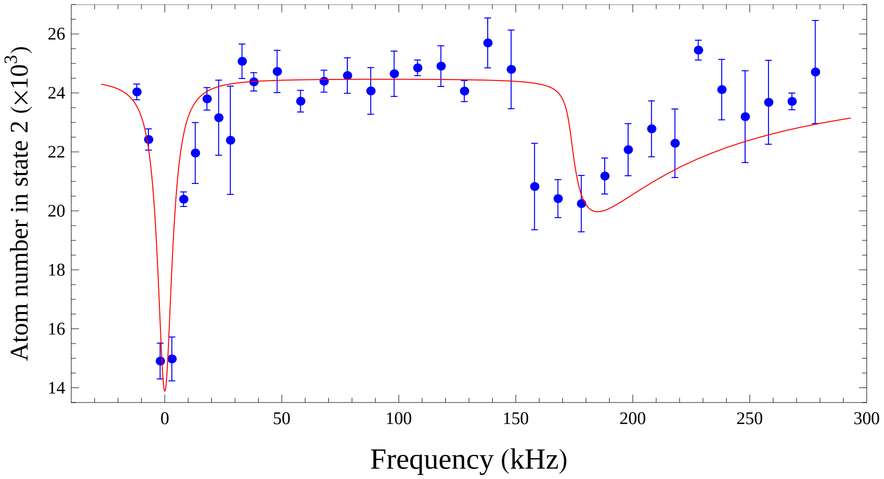

(a) Fit to the data contains only dimer bound state to scattering state transition. The broadening of the resonance on the right is as small as the broadening of the atomic transition resonance on the left.

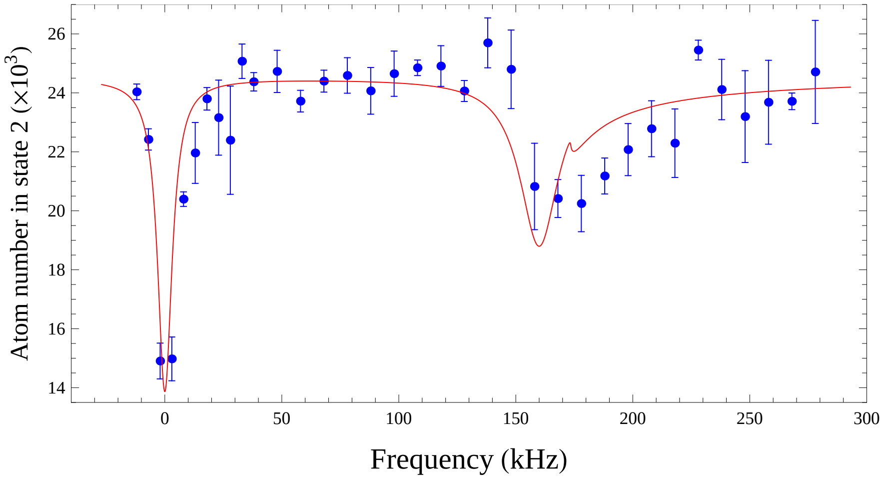

(b) Fit to the data contains both dimer bound state to scattering state transition and bound to bound transition. Bound to bound transition fraction $\epsilon_{bb} = 0.60$.

Figure 6.3: Dimer theory fits of 12 to 13 rf transition spectrum at 718.5 G for 20% trap depth with $\nu_z = 82.5$ kHz (red curves). The origin of the x axis corresponds to the bare 2 to 3 atomic transition frequency for 718.5 G, 82.472 MHz.

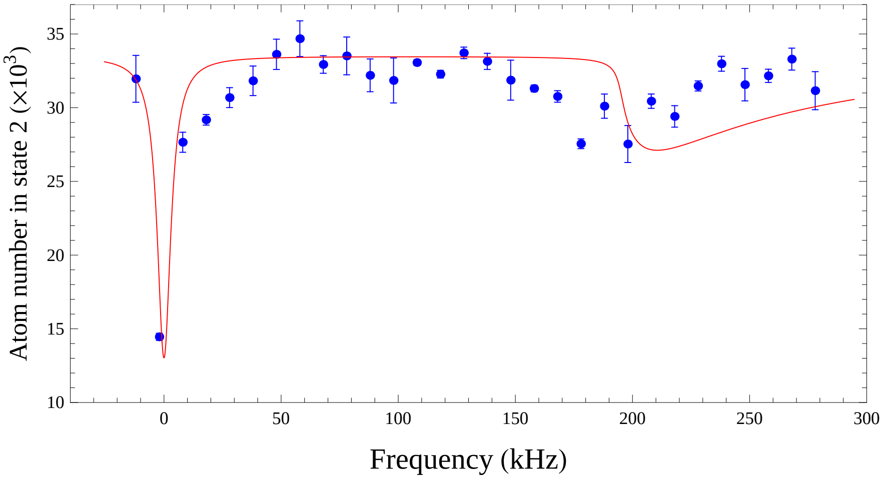

(a) Fit to the data contains only dimer bound state to scattering state transition. The broadening of the resonance on the right is as small as the broadening of the atomic transition resonance on the left.

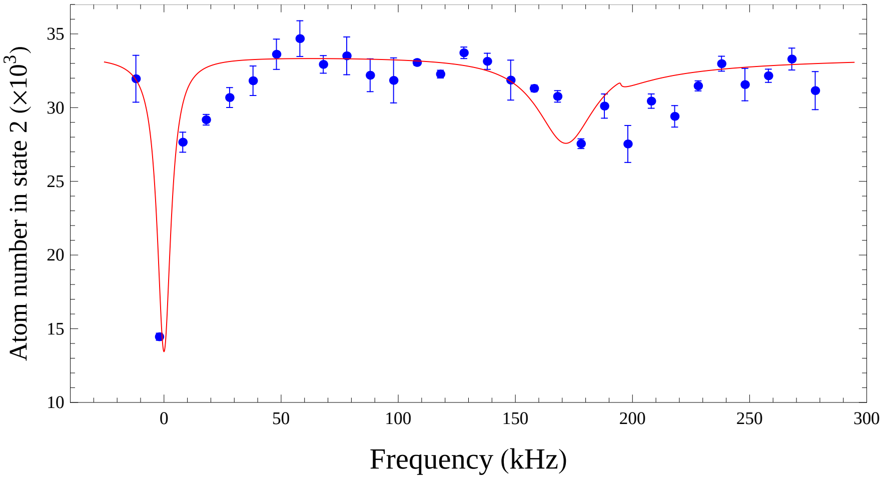

(b) Fit to the data contains both dimer bound state to scattering state transition and bound to bound transition. Bound to bound transition fraction $\epsilon_{bb} = 0.70$.

Figure 6.4: Dimer theory fits of 12 to 13 rf transition spectrum at 718.7 G for 50% trap depth with ν_z = 135 kHz (red curves). The origin of the x axis corresponds to the bare 2 to 3 atomic transition frequency for 718.7 G, 82.470 MHz.

Figure 6.2 (a). However, after including the bound to bound transition based on the bound to bound transition fraction ϵ_{bb}, the predicted spectrum does not give the right shape of the peak any more as shown in Figure 6.2 (b). For 20% and 50% data in Figure 6.3 and 6.4, I try to draw the same predicted spectra by including only bound to scattering state transition for in subfigure(a) and including both bound to scattering state and bound to bound transitions in subfigure(b). We notice that for each trap depth, neither of these two fits matches the experimental data very well, but the bound to bound transition part gives a better fit in the threshold region for the 20% trap depth, where we expect a large bound to bound transition fraction ($\epsilon_{bb} = 0.60$).

Dimer spectra near the Feshbach resonance, around 834 G

We notice around Feshbach resonance, the spectra show the similar shapes and behavior as shown in Figure 6.6, 6.7 and 6.8. So, I want to show the comparison between the theory and the data in this area by using a representative one, spectra at 832 G where we have data for four different trap depths, 2%, 20%, 50% and 100%. At 832 G, the bound to bound transition should dominate because of the big transition fraction ϵ_{bb} as I label in Figure 6.5. I plot the whole spectra predicted by dimer theory on the top of 832 G data including only bound to bound transition in red dashed lines while the red solid lines include both bound to bound and bound to scattering state transitions as shown in Figure 6.5. For each spectrum data shown as blue dots, we can see two major resonances. The left ones correspond to bare atomic transitions from state 2 to 3. The broader one on the right side should correspond to dimer transitions. The shape of the broader resonance is quite symmetric which is consistent with the shape of bound

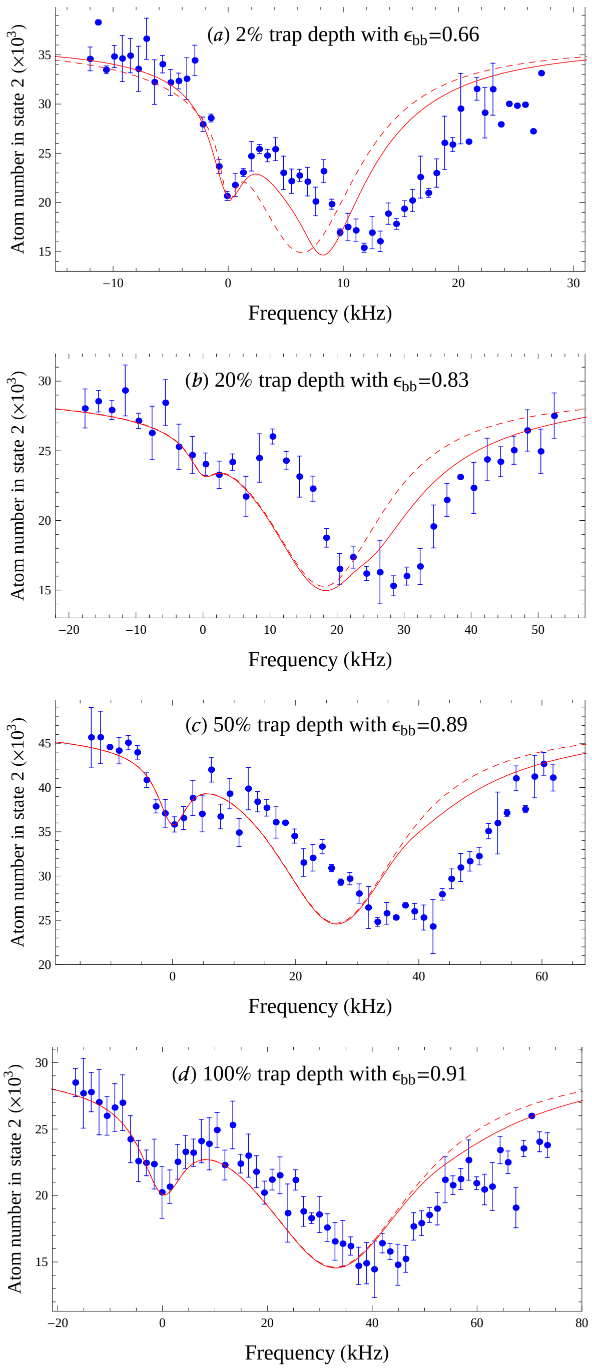

Figure 6.5: Dimer theory fits of 12 to 13 rf transition spectra at 832 G. The origin of the x axis corresponds to the bare 2 to 3 atomic transition frequency 81.708 MHz, dashed red curves are fits containing only bound to bound transition, while solid red curves are the fits containing both bound state to scattering state transition and bound to bound transition.

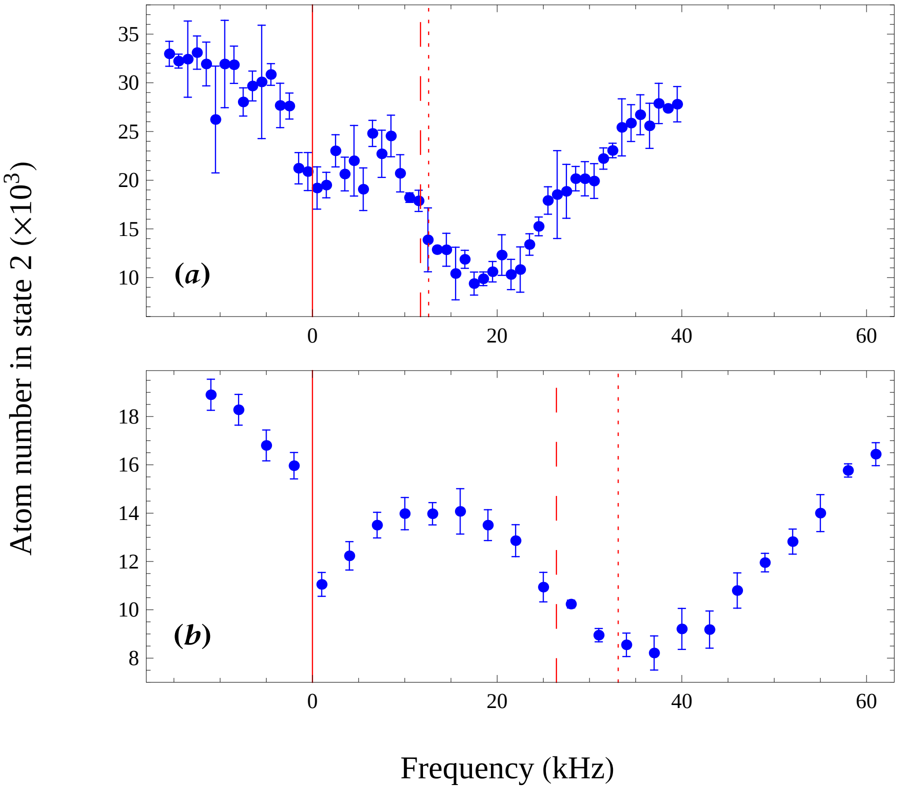

Figure 6.6: Positions of resonances predicted by dimer theory compare with 12 to 13 rf transition spectra around 810 G for different trap depths. The origin of x axis shown as red solid lines corresponds to the bare 2 to 3 atomic transition frequency, while the red dotted lines show the calculated positions of dimer bound state to scattering state transitions and the red dashed lines show the calculated positions of dimer bound to bound transitions. (a) 808.6 G (81.8455 MHz),$\nu_z = 24.5$ kHz, 2% trap depth; (b) 809.5 G (81.84 MHz), $\nu_z = 82.5$ kHz, 20% trap depth.

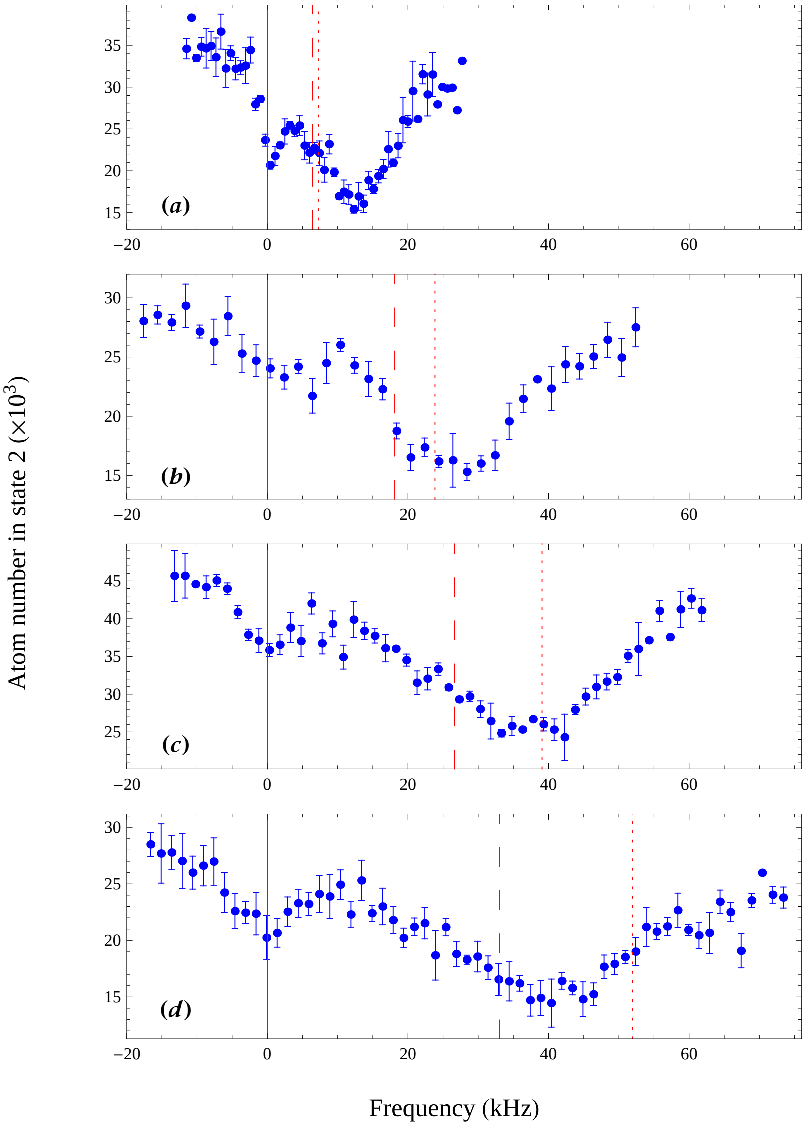

Figure 6.7: Positions of resonances predicted by dimer theory compare with 12 to 13 rf transition spectra around 832 G for different trap depths. The origin of x axis shown as red solid lines corresponds to the bare 2 to 3 atomic transition frequency, while the red dotted lines show the calculated positions of dimer bound state to scattering state transitions and the red dashed lines show the calculated positions of dimer bound to bound transitions. (a) 832.2 G (81.7065 MHz), $\nu_z = 24.5$ kHz, 2% trap depth; (b) 832.0 G (81.7076 MHz), $\nu_z = 82.5$ kHz, 20% trap depth; (c) 831.9 G (81.7082 MHz), $\nu_z = 135$ kHz, 50% trap; (d) 831.3 G (81.7116 MHz), $\nu_z = 179$ kHz, 100% trap depth.

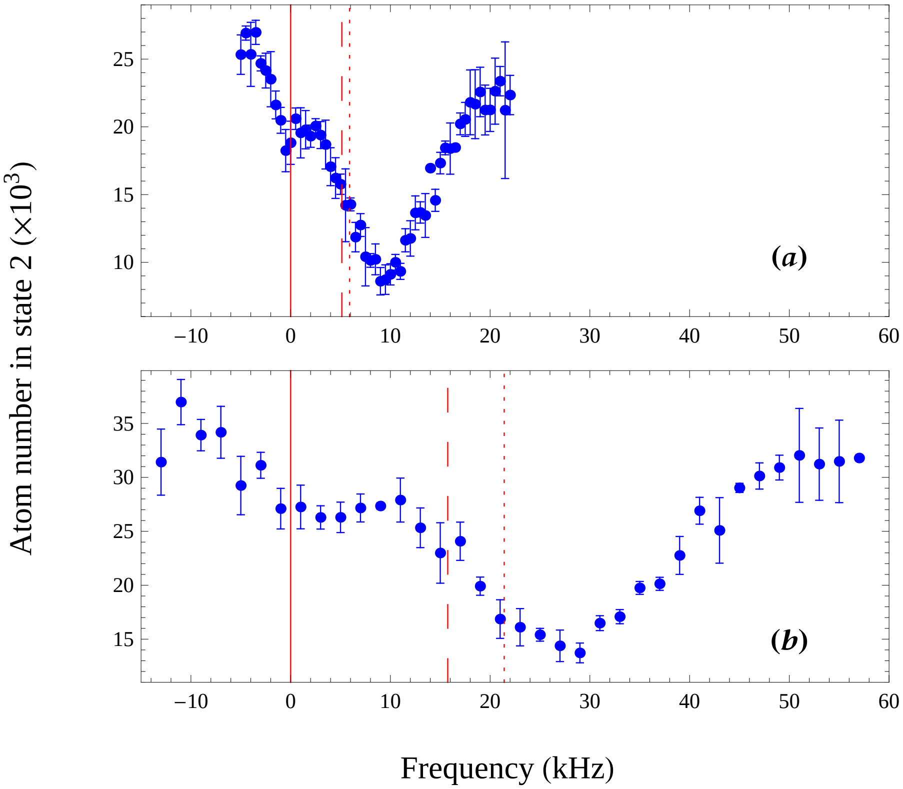

Figure 6.8: Positions of resonances predicted by dimer theory compare with 12 to 13 rf transition spectra at 841.7 G for different trap depths. The origin of x axis shown as red solid lines corresponds to the bare 2 to 3 atomic transition frequency (81.653 MHz), while the red dotted lines show the calculated positions of dimer bound state to scattering state transitions and the red dashed lines show the calculated positions of dimer bound to bound transitions. $(a)\nu_z = 24.5$ kHz, 2% trap depth; $(b)\nu_z = 82.5$ kHz, 20% trap depth.

to bound transition resonance, which should dominate. However, neither the red solid lines nor the red dashed lines match the data.

We also saw the disagreement of dimer theory prediction in the data fitting with other magnetic fields around Feshbach resonance.

In Figure 6.6, 6.7 and 6.8, I list data at three magnetic fields: 811 G, 832 G and 842 G for different trap depth. For each set of data, I put data in different trap depths in the same scale for x axis in order to compare the relative positions and separation between resonances. Instead of plotting the whole spectrum like at 832G, I just labeled the resonace positions of theoretical prediction based on dimer theory. We can see the obvious disagreements in this way. The red solid lines are the bare atomic transition from 2 to 3, which are the references. I use red dotted lines to show position of dimer bound to scattering state transition resonances and red dashed lines to show the bound to bound transition resonances. I plot the 832 G data once again here in order to compare with other two data sets.

Dimer spectra between 720 G and 811 G

From 720 G, where the 12 dimer binding energy is much larger than the transverse Fermi energy, to 842 G, where the 12 dimer binding energy is much smaller than the transverse Fermi energy, it seems that the dimer transition theory show more disagreement with the data. Around Feshbach resonance, no matter how we do the fitting, the prediction can not explain the data. Although at 720 G for 2% trap depth, the bound state to scattering state transition part can fit the data quite well, the full spectrum predicted by the theory has different shape from the data.

If we take a look at the dimer theory predictions of the resonance positions

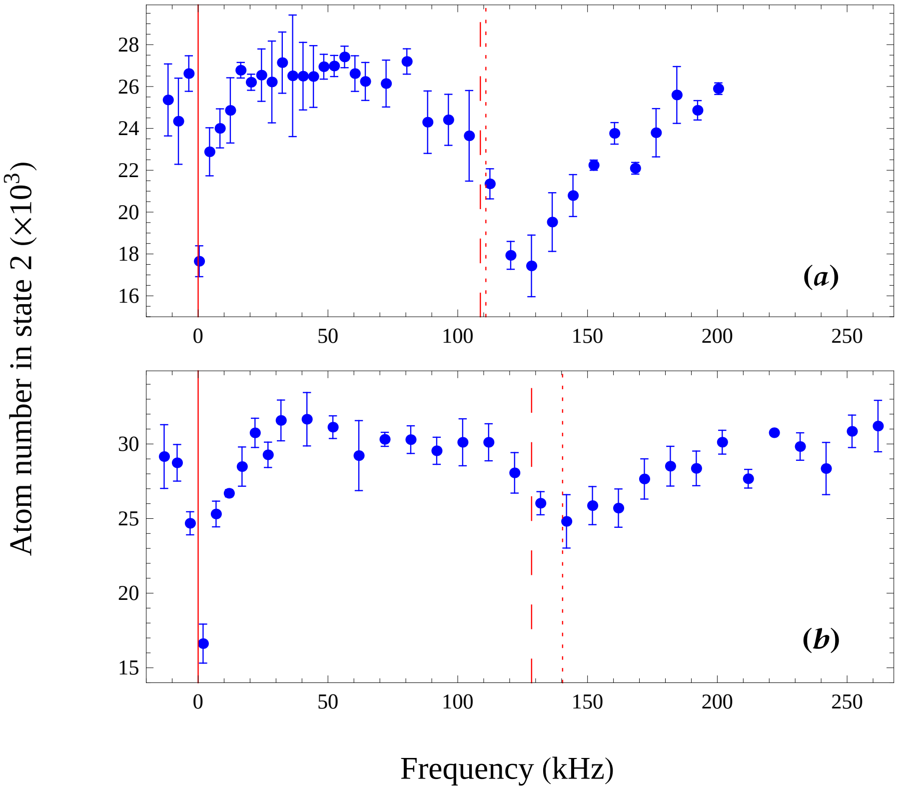

Figure 6.9: Positions of resonances predicted by dimer theory compare with 12 to 13 rf transition spectra around 730 G for different trap depths. The origin of x axis shown as red solid lines corresponds to the bare 2 to 3 atomic transition frequency, while the red dotted lines show the calculated positions of dimer bound state to scattering state transitions and the red dashed lines show the calculated positions of dimer bound to bound transitions. (a) 728.5 G (82.3939 MHz),$\nu_z = 24.5$ kHz, 2% trap depth; (b) 728.3 G (82.3954 MHz),$\nu_z = 82.5$ kHz, 20% trap depth.

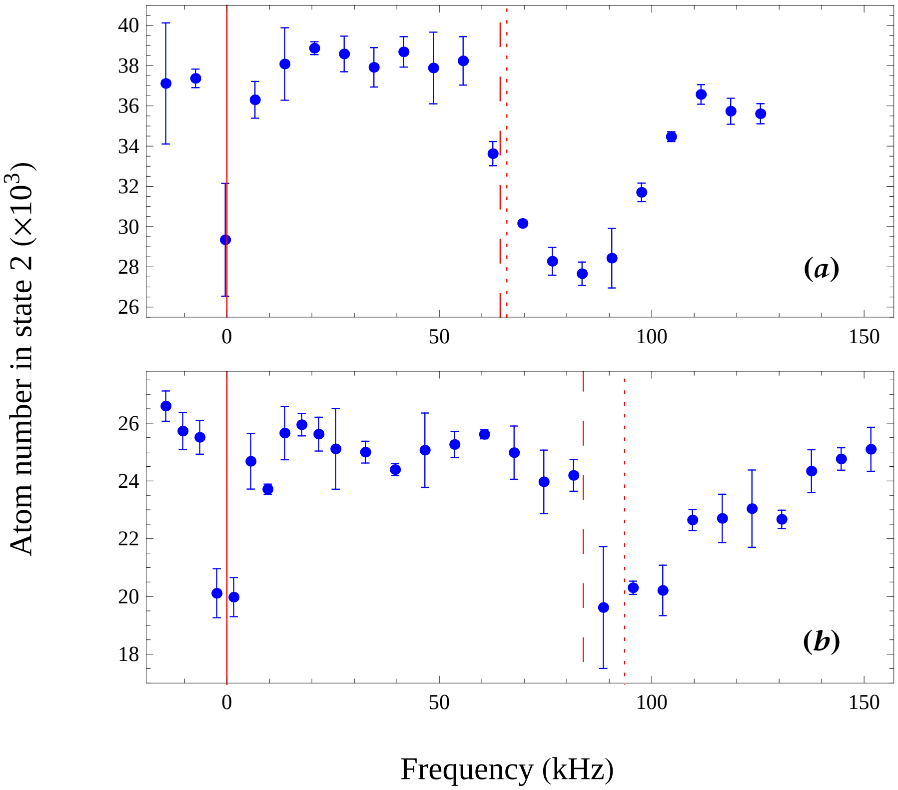

Figure 6.10: Positions of resonances predicted by dimer theory compare with 12 to 13 rf transition spectra at 748.0 G for different trap depths. The origin of x axis shown as red solid lines corresponds to the bare 2 to 3 atomic transition frequency (82.2482 MHz), while red dotted lines show the calculated position of dimer bound to scattering state transition and red dashed lines show the calculated position of dimer bound to bound transition. $(a)\nu_z = 24.5$ kHz, 2% trap depth; $(b)\nu_z = 82.5$ kHz, 20% trap depth.

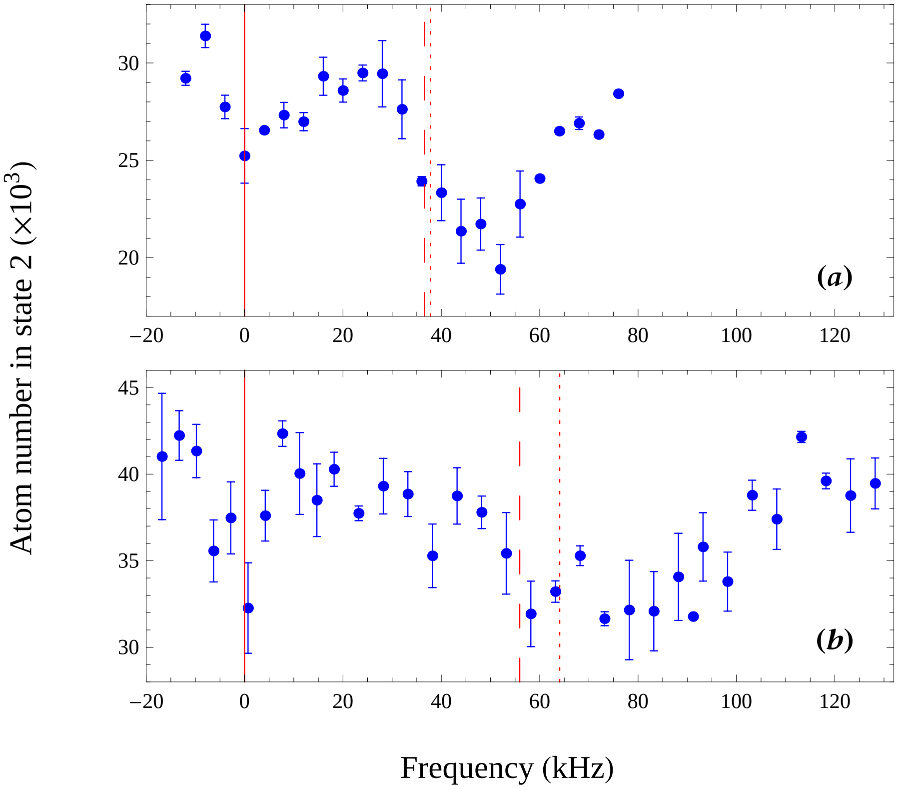

Figure 6.11: Positions of resonances predicted by dimer theory compare with 12 to 13 rf transition spectra around 770 G for different trap depths. The origin of x axis shown as red solid lines corresponds to the bare 2 to 3 atomic transition frequency, while the red dotted lines show the calculated positions of dimer bound state to scattering state transitions and the red dashed lines show the calculated positions of dimer bound to bound transitions. (a) 768.2 G (82.106 MHz), $\nu_z = 24.5$ kHz, 2% trap depth; (b) 767.5 G (82.1108 MHz), $\nu_z = 82.5$ kHz, 20% trap depth.

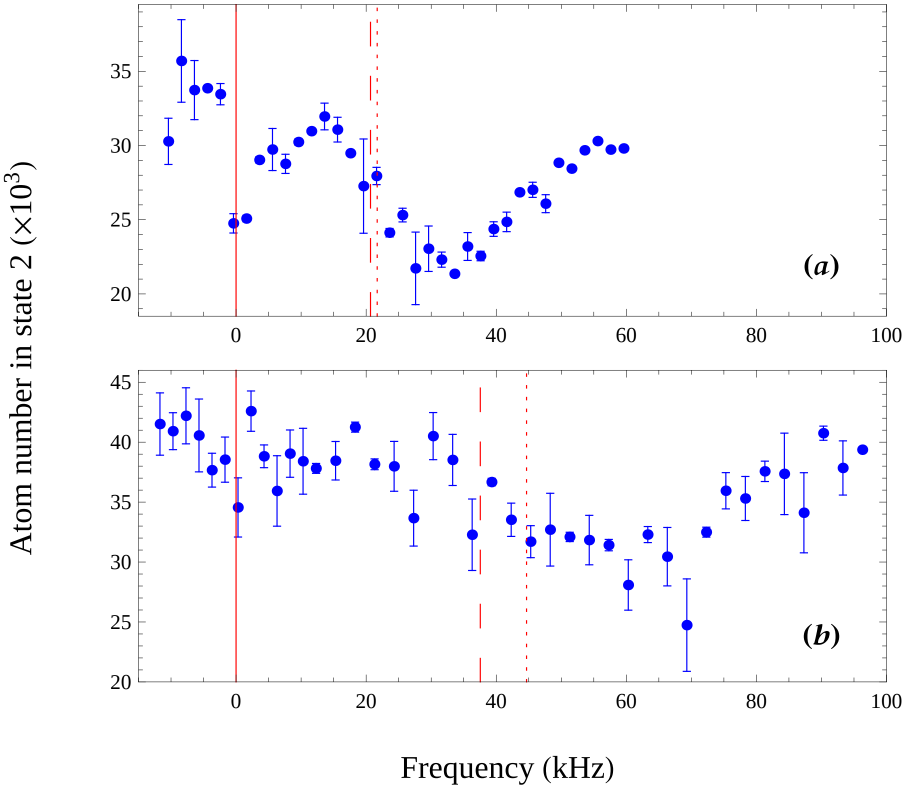

Figure 6.12: Positions of resonances predicted by dimer theory compare with 12 to 13 rf transition spectra around 790 G for different trap depths. The origin of x axis shown as red solid lines corresponds to the bare 2 to 3 atomic transition frequency, while the red dotted lines show the calculated positions of dimer bound state to scattering state transitions and the red dashed lines show the calculated positions of dimer bound to bound transitions. (a) 788.5 G (81.9714 MHz), $\nu_z =$ 24.5 kHz, 2% trap depth; (b)788.3 G (81.9727 MHz), $\nu_z =$ 82.5 kHz, 20% trap depth.

between 720 G to 811 G, we can see the trend that the fit is getting worse as the magnetic field increases. Here I list the data for 730 G, 750 G, 770 G and 790 G in the Figure 6.9, 6.10, 6.11 and 6.12.

6.1.2 Dimer fits for experiments in 1-3 mixtures

For experiment starting from 13 mixture, we also start by preparing 50-50 1-2 mixture. After having the balanced 1-2 mixture in the standing wave trap of inferred CO_2 laser beam directly transferred from MOT, we turn on the high magnetic field and set it to be about 528G, where the 1-2 s-wave scattering length is around zero and there is no interactions between atoms in state 1 and 2. Then we cut down the backgoing CO_2 laser beam in the non-interacting region and try to avoid heating which may happen in other magnetic fields. Then we start sending a rf pulse with a frequency sweep(10 ms, 10 kHz) to completely transfer atoms from state 2 to state 3. Then we shift the magnetic field from 528 G to 690 G where is the Feshbach resonance of 1-3 mixture to do evaporation. After evaporation, we will have cold enough atoms for our experiments. We measured that the ratio of atom numbers in state 1 and 3 is about 1 : 0.95, which is good enough for requirement of balanced mixture. Then we switch magnetic field from 690G to anywhere we want to do experiment. Then the standing wave will be turned on for the quasi 2D experiments.

Here I want to mention that in the preparation of 1-3 mixture, we did not use π pulse of rf signal. Because this way requires very high stability of the system magnetic field in order to stabilize the transition frequency (within 1kHz), which is too challenging to us right now. Maybe after building up the magnetic field stabilization system, we can try this method one more time.

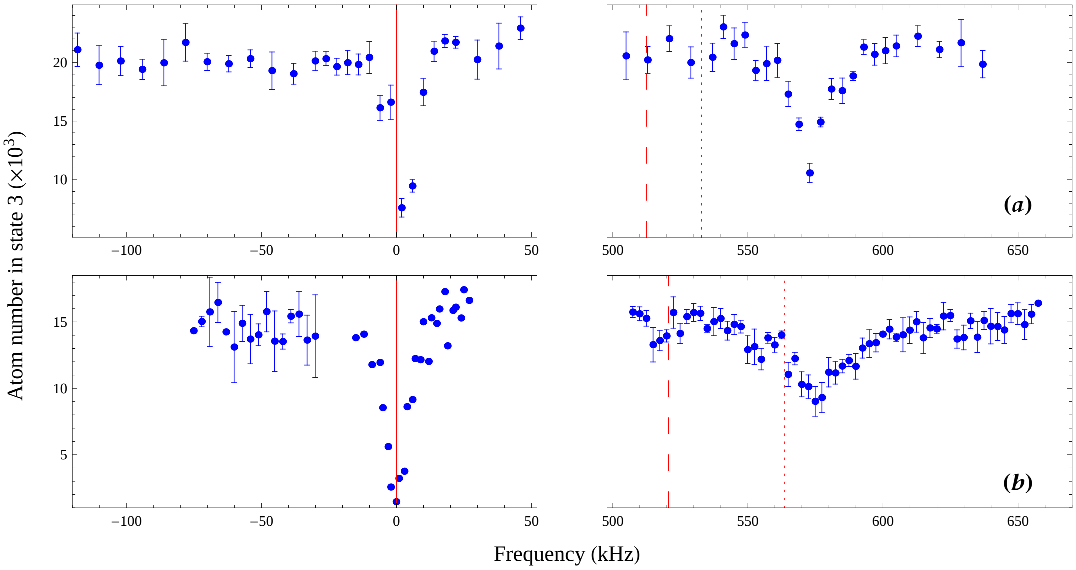

Figure 6.13: Positions of resonances predicted by dimer theory compare with 13 to 12 rf transition spectra at 669.2 G for different trap depths. The origin of x axis shown as red solid lines corresponds to the bare 3 to 2 atomic transition frequency for 669.2 G, 82.895 MHz, while red dotted lines show the calculated positions of dimer bound state to scattering state transitions and red dashed lines show the calculated positions of dimer bound to bound transitions. (a) $\nu_z = 24.5$ kHz, 2% trap depth; $(b)\nu_z = 82.5$ kHz, 20% trap depth.

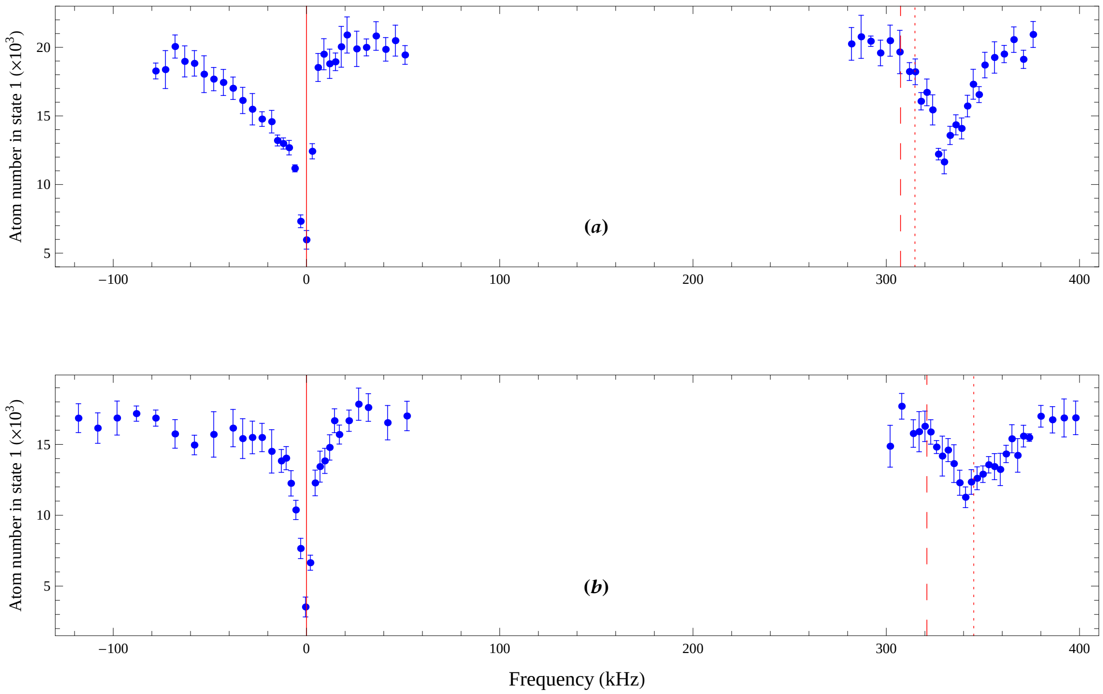

Figure 6.14: Positions of resonances predicted by dimer theory compare with 13 to 12 rf transition spectra at 688.9 G for different trap depths. The origin of x axis shown as red solid lines corresponds to the bare 3 to 2 atomic transition frequency for 688.9G, 82.718MHz, while red dotted lines show the calculated positions of dimer bound state to scattering state transitions and red dashed lines show the calculated positions of dimer bound to bound transitions. (a) $\nu_z = 24.5$ kHz, 2% trap depth; $(b)\nu_z = 82.5$ kHz, 20% trap depth.

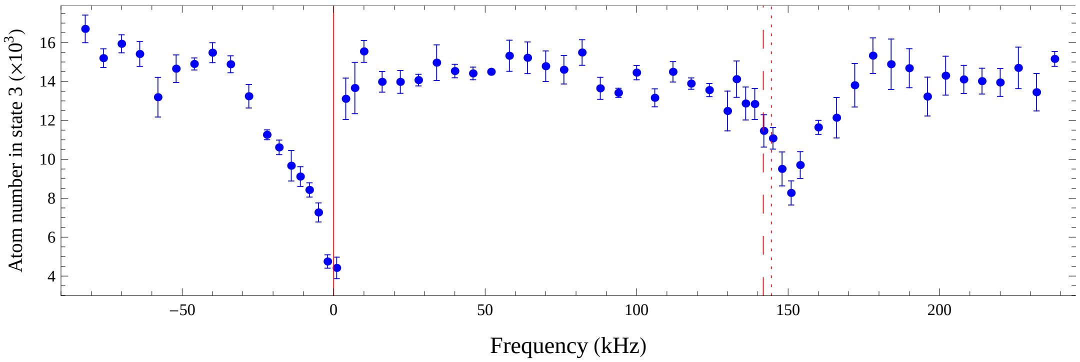

Figure 6.15: Position of resonance predicted by dimer theory compares with 13 to 12 rf transition spectrum at 718.5 G, 2% trap depth, $\nu_z = 24.5$ kHz. The origin of x axis shown as red solid line corresponds to the bare 3 to 2 atomic transition frequency for 718.5G, 82.472MHz, while red dotted line shows the calculated position of dimer bound state to scattering state transition and red dashed line shows the calculated position of dimer bound to bound transition.

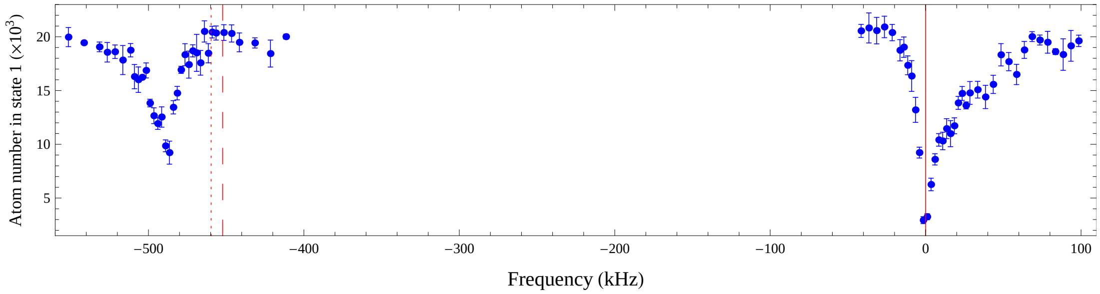

Figure 6.16: Positions of resonances predicted by dimer theory compare with 13 to 23 rf transition spectra at 688.9 G, 2% trap depth, $\nu_z = 24.5$ kHz. The origin of x axis shown as red solid line corresponds to the bare 1 to 2 atomic transition frequency for 688.9 G, 76.032 MHz, while red dotted line shows the calculated position of dimer scattering state to bound state transition and red dashed line shows the calculated position of dimer bound to bound transition.

In terms of the dimer theory fits for rf transition in 1-3 mixture, I list the 1-3 to 1-2 transition spectra for 670 G, 690 G and 720 G and mark the predicted resonance positions based on dimer theory on top of them in Figure 6.13, 6.14 and 6.15. And the 1-3 to 2-3 transition spectrum for 690 G data in Figure 6.16. We can see that there are still disagreements. But since the dimer binding energy for these data are much larger than the 1-2 mixture case, the relative discrepancy is not that much.

For 720G, we have data start from both 1-2 mixture and 1-3 mixture, and at different trap depths. I put them together in Figure 6.17 and make the x axis scale the same in order to compare. We can see that the positions of resonances in Figure 6.17 (a) and (b) are almost in the same place, but the shapes of spectra are quite different.

By changing the magnetic field and mixture of initial states, we obtain different combination of initial and final dimer binding energies for different rf transition experiments. We notice that the dimer transition theory can not explain these spectra very well, especially for cases with small initial dimer binding energies. For experiments start from 50-50 1-2 mixture, around 1-2 Feshbach resonance, some of the distances between resonances in the data are almost twice as much as the prediction.

Besides using the subtraction of dimer binding energy, like $E_b^{12} - E_b^{13}$, to compare with the data, we also try to add some scale factors in the subtraction, like trying to fit $\lambda_{12} E_b^{12} - \lambda_{13} E_b^{13}$ to the data by changing λ_{12} and λ_{13}. However, we can not find any fixed scale factors.

In order to find a more reasonable explanation for these spectra, we considered about other interactions between atoms. In the next section I will show you the fits based on polaron transition theory.

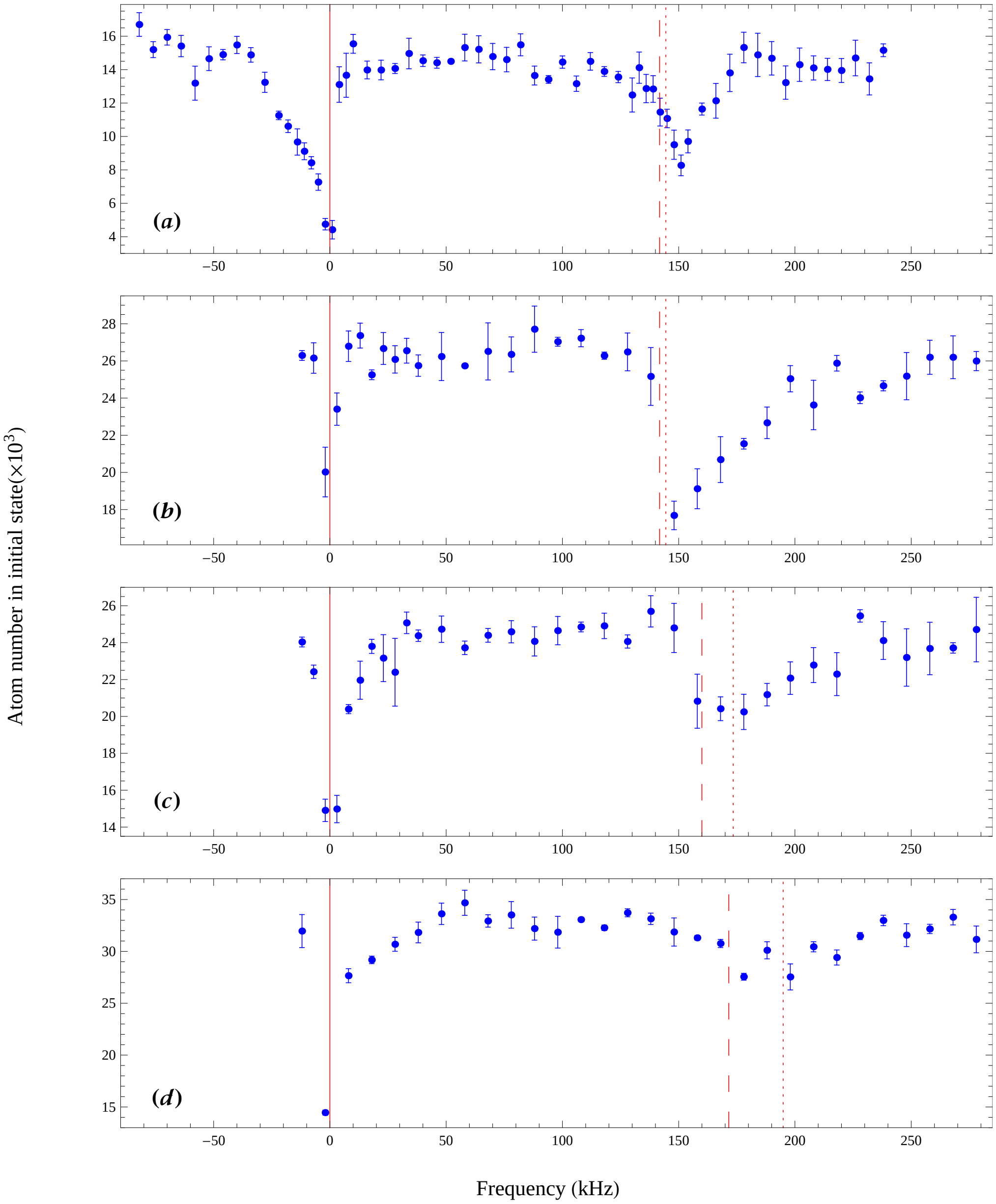

Figure 6.17: Positions of resonances predicted by dimer theory compare with rf transition spectra at 718.5 G for different trap depth. The origin of x axis shown as red solid lines corresponds to the bare atomic transition frequency between state 2 and 3 for 718.5 G, 82.472 MHz, while red dotted lines show the calculated positions of dimer bound state to scattering state transitions and red dashed lines show the calculated positions of dimer bound to bound transitions. (a) 13 to 12 transition for 2% trap depth, $\nu_z = 24.5$ kHz; (b) 12 to 13 transition for 2% trap depth, $\nu_z = 24.5$ kHz; (c) 12 to 13 transition for 20% trap depth, $\nu_z = 82.5$ kHz; (d) 12 to 13 transition for 50% trap depth, $\nu_z = 127.5$ kHz.

6.2 Polaron transition spectra

When the transverse Fermi energy is larger than the dimer binding energy, $E_{F\perp} > E_b$, the interparticle spacing is comparable to the dimer size and many-body effect should show up. In our rf spectroscopy experiments around 1-2 Feshbach resonance at 834 G, $E_{F\perp} > E_b^{12} > E_b^{13}$.

We consider two dimensional non-interacting polaron as the many-body effect and notice that the polaron binding energy, E_p, is much larger than the corresponding dimer binding energy E_b. That means polarons are expected to be energetically more favorable than the corresponding dimers.

Since we have 50-50 balanced 1-2 mixture to start with in the rf transition, we only assume final states to be 1-3 polaron states and keep the initial states to be dimer bound states or scattering states. Here 1-3 polaron is an atom in state 3 surrounded by a cloud of particle-hole pairs in state 1. However, since 1-3 polaron binding energy is so large that $E_b^{12} - E_p^{13}$ is negative and it predicts the additional resonance on the left side of the atomic transition resonance, which is not what we observe on the spectra. We are forced to treat the initial state to be polaron as well.

We calculate the polaron binding energy by using equation (4.20), which I derived in Chapter 4. Here, the polaron binding energy is a function of the 2D local Fermi energy $E_{F\,\mathrm{local}}$ and the dimer binding energy E_b

$$\epsilon \equiv \Sigma(\epsilon) = -2\int_0^1 \frac{du}{-\ln\left(\frac{E_b}{E_{F_\perp}}\right) + \ln\left[\sqrt{\left(1-\frac{\epsilon}{2}\right)^2 - u} + \left(1 - \frac{\epsilon}{2} - \frac{u}{2}\right)\right]}. \tag{6.4}$$

Since we don't know the 2D local Fermi energy, we assume that the average local Fermi energy is proportional to the ideal gas global Fermi energy

$$E_{F\,(\text{2D local})} = \lambda_1 E_{F\,(\text{2D ideal gas})} \tag{6.5}$$

which we can determine experimentally by measuring the total atom number per pancake in the quasi-two dimensional trap, $E_{F(\text{2D ideal gas})} = \sqrt{N_{perpancake}}\, h\, \nu_\perp$, where $\nu_\perp = \sqrt{\nu_x \cdot \nu_y}$. The proportional parameter λ_1 is the only fitting parameter. We find that by using one value of λ_1, $\lambda_1 = 0.67$, the predictions of broad resonance positions based on polaron transitions match with the resonance position on all the 12 to 13 transition spectra at 810 G, 832 G and 842 G for different trap depths as shown as thick red dashed lines in Figures 6.18, 6.19 and 6.20.

6.2.1 Data fitting to extract resonance separations

In order to compare the subtraction of polaron binding energy $E_p^{12} - E_p^{13}$ with the data, we need to extract resonance separations from the data by fitting them to a two peak function. Here I will give some details about how we choose the two peak function.

In Figures 6.18, 6.19 and 6.20, I list all the spectra fits we have for the comparison. The positions of the bare atomic transition resonances are labeled as vertical red solid lines on the spectra. They are determined from the bare atomic rf transition experiment from state 2 to 3 without any atom in state 1. We also measure the atomic transition resonance positions in different trap depths and different temperatures for transitions from 1-2 mixture to 1-3 mixture. We notice that the bare atomic transition resonances are in the same place no matter how we change the parameters.

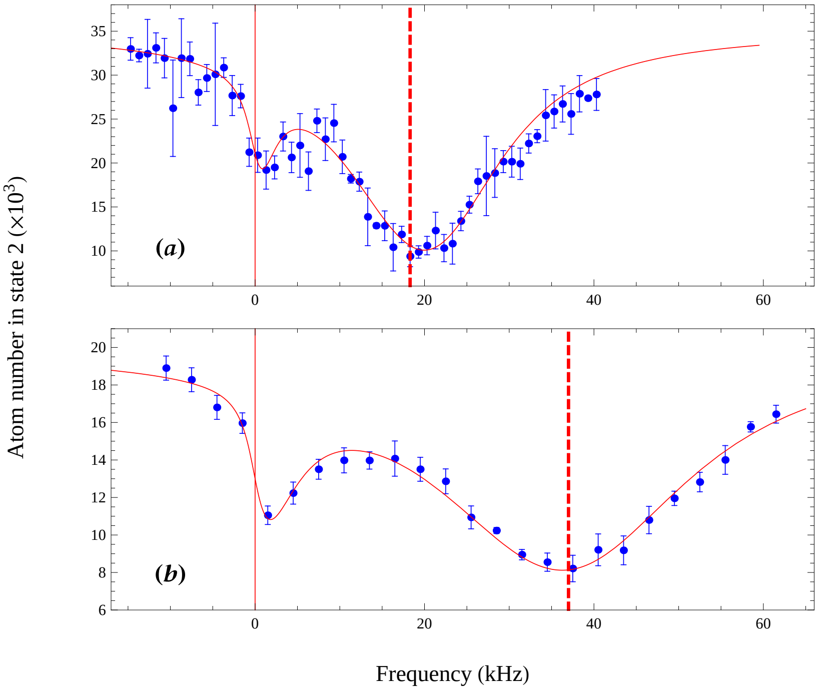

Figure 6.18: Fits of the rf spectra around 811G to extract resonance separation and polaron transition predictions. The vertical red solid lines mark the bare atomic transition resonances. Red solid curve along the data (blue dots) are the fits based on the equation (6.7) and (6.12). The thick red dashed lines are the predicted broad resonance positions based on polaron transitions. (a) 808.6G (81.8455MHz),$\nu_z = 24.5$ kHz, 2% trap depth; (b) 809.5G (81.84MHz), $\nu_z = 82.5$ kHz, 20% trap depth.

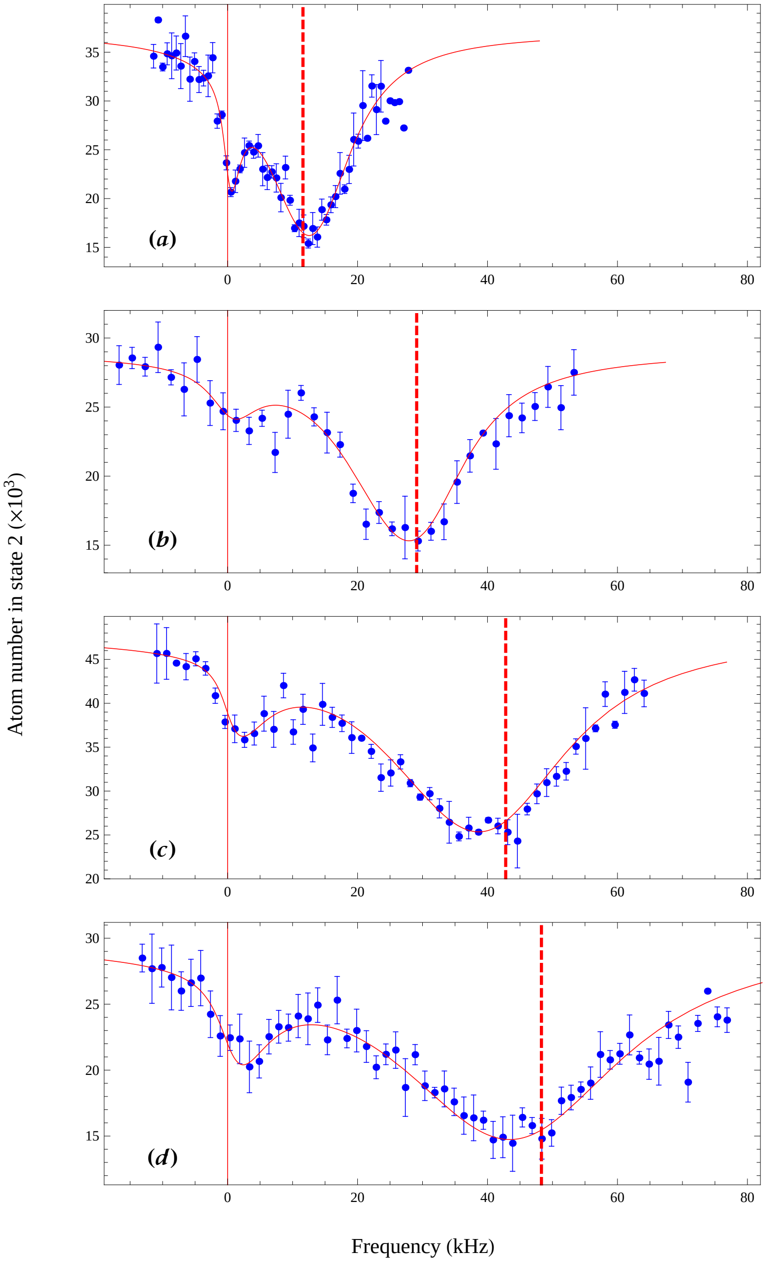

Figure 6.19: Fits of the rf spectra around 832G to extract resonance separation and polaron transition predictions. The vertical red solid lines mark the bare atomic transition resonances. Red solid curve along the data (blue dots) are the fits based on the equation (6.7) and (6.12). The thick red dashed lines are the predicted broad resonance positions based on polaron transitions. (*a*) 832.2 G (81.7065 MHz), $\nu_z = 24.5$ kHz, 2% trap depth; (*b*) 832.0 G (81.7076 MHz),$\nu_z = 82.5$ kHz, 20% trap depth; (*c*) 831.9 G (81.7082 MHz), $\nu_z = 135$ kHz, 50% trap; (*d*) 831.3 G (81.7116 MHz),$\nu_z = 179$ kHz, 100% trap depth depth.

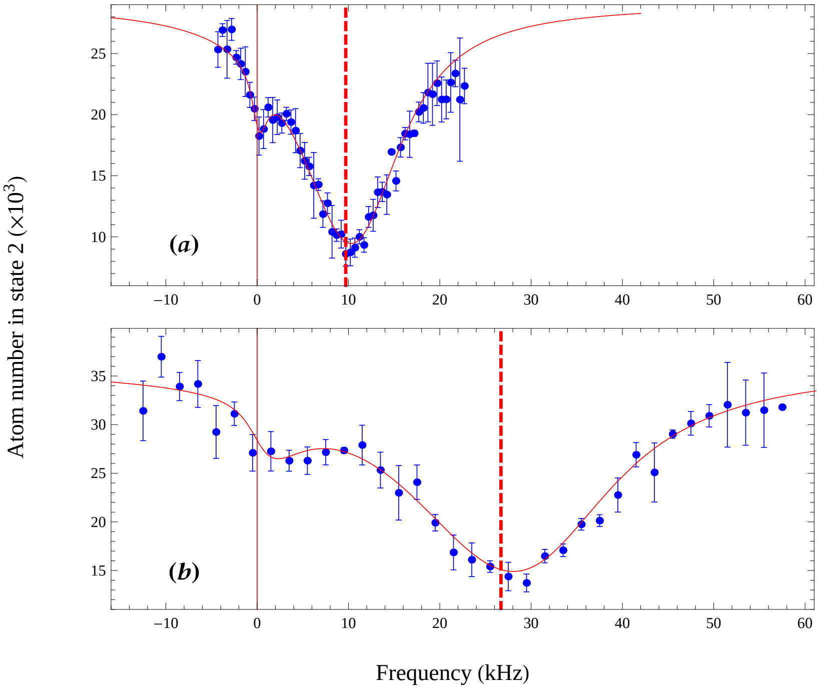

Figure 6.20: Fits of the rf spectra at 841.7G to extract resonance separation and polaron transition predictions. The vertical red solid lines mark the bare atomic transition resonances (81.653 MHz). Red solid curve along the data (blue dots) are the fits based on the equation (6.7) and (6.12). The thick red dashed lines are the predicted broad resonance positions based on polaron transitions. $(a)\nu_z = 24.5$ kHz, 2% trap depth; $(b)\nu_z = 82.5$ kHz, 20% trap depth.

For the bare atomic transition resonances, we notice that most of them exhibit a fast rise and a tail toward higher frequency. We believe this shape is caused by the mean-field shift and should be fitted using a threshold function. The broad resonances on the right side of the spectra are quite symmetric. A symmetric peak function should be used to fit it. The combination of these two functions will serve as the two peak function for the whole spectrum fitting.

In this dissertation, I simply choose half of a Lorentzian function

$$f(x) = \Theta(\nu_a) \frac{w/2}{(x - \nu_a)^2 + (w/2)^2} \tag{6.6}$$

to be the the threshold function for the atomic transition resonances. Here $\Theta(\nu_a)$ is a step function and ν_a is the atomic transition frequency. w is the width of the Lorentzian shape. Then broaden it in a convolution,

$$I_1(\nu) \propto \int_0^\infty dx \frac{f(x)}{\pi} \frac{w'/2}{(x - \nu)^2 + (w'/2)^2}. \tag{6.7}$$

where w' is the width of the broadening.

The polaron binding energy E_p is different in different places of the atom cloud because of the different local Fermi energies $E_{F\,(\text{2D local})}$. I integrate $E_p^{12} - E_p^{13}$ in a two dimension plane to serve as the symmetric peak function for the fits of the broad resonances on the right side of the spectra. To simplify the expression of polaron binding energy, I use the approximate function (4.21) instead of the exact funciton (4.20). I can get $E_p^{12} - E_p^{13}$ for a certain local Fermi energy $E_{F\,(\text{2D local})}$,

$$\nu_0(E_F) = \frac{1}{h} \left[\frac{2E_F(n_\perp)}{ln(1 + \frac{2E_F}{E_b^{12}})} - \frac{2E_F(n_\perp)}{ln(1 + \frac{2E_F}{E_b^{13}})} \right]. \tag{6.8}$$

Then I integrate over the 2D atomic density distribution $n_\perp(\rho)$ to get the total spectrum.

$$I_2(\nu) = \frac{1}{N}\int_0^{\sigma_F} 2\pi\rho\, d\rho\, n_\perp(\rho)\frac{1}{\pi}\frac{w''/2}{[\nu-\nu_0(E_F)]^2+(w''/2)^2}, \tag{6.9}$$

where

$$E_F = \frac{\hbar^2}{m}2\pi n_\perp\ ,\ n_\perp = n_0\left(1-\frac{\rho^2}{\sigma_F^2}\right). \tag{6.10}$$

Here N is the 2D total atom number, σ_F is the Fermi radius of the 2D system and w'' is the full width of broadening Lorentzian lineshape. Then

$$E_F(\rho) = E_F(0)\left(1-\frac{\rho^2}{\sigma_F^2}\right)\ \ ,\ dE_F = -2\rho d\rho\left(\frac{E_F(0)}{\sigma_F^2}\right) \tag{6.11}$$

We can write the spectrum (6.9) as

$$I_2(\nu) \propto \int_0^{E_F(0)} dE_F E_F\frac{1}{\pi}\frac{w''/2}{[\nu-\nu_0(E_F)]^2+(w'/2)^2} \tag{6.12}$$

Since I do not know the maximum local Fermi energy $E_F(0)$, I just assume it is proportional to the ideal gas Fermi energy we can measure experimentally, $E_F(0) = \lambda_2 E_{F\,\text{ideal gas 2D}}$. $E_{F\ \text{ideal gas 2D}} = \sqrt{N_{persite}}\,h\,\nu_\perp$, where $\nu_\perp = \sqrt{\nu_x\cdot\nu_y}$, λ_2 is a fitting parameter. The function $I_1(\nu)+I_2(\nu)$ is the two peak function I use in Figures 6.18, 6.19 and 6.20 to fit the spectra. The fits can tell us the peak frequencies of the broad resonances. By subtracting the bare atomic transition frequencies we measured experimentally, we extract the resonance separations.

In our paper [4], we used another two peak function to fit the data. A threshold function was derived from the mean field shift,

$$I(\nu) = \frac{1}{2\left(\frac{1}{L_{13}} - \frac{1}{L_{13}+q}\right)\left(1 + \frac{1}{L_{13}} + \frac{1}{L_{13}+q}\right)}, \tag{6.13}$$

where

$$\frac{2qe^{-L_{13}}}{L_{13}(L_{13}+q)} - \frac{h(\nu - \nu_a)}{E_b^{13}} = 0 \ , \ q = ln\left(\frac{\epsilon_b^{13}}{\epsilon_b^{12}}\right). \tag{6.14}$$

Here, ν_a is the bare atomic transition frequency. And a simple Lorentzian function, which is symmetric, was used to fit the broad resonance. Although different fitting functions are used, the separations between resonances we extract from the data are very similar as shown in Table 6.1.

The fact that we can use two different fitting functions to extract almost the same resonance separations shows that the separations are reliable for next step comparison with polaron theory.

6.2.2 Polaron transition prediction

In Table 6.1, I list the measured frequency shifts based on both the fits we use in our paper as $\Delta\nu_{meas1}$ and the fits I show in Figures 6.19, 6.18 and 6.20 as $\Delta\nu_{meas2}$. These two frequency shifts are consistent with each other although from different fits. Then we can compare the measured frequency shifts with the calculated results based on the accurate polaron binding energy function (4.20), which we obtain in Chapter4. I list the accurate calculation result as $\Delta\nu_{polaron1}$ with $\lambda_1 = 0.67$ in Table 6.1. Here, λ_1 is the only fitting parameter compared with the measured value. And for all of the eight sets of data around Feshbach resonance, the prediction based polaron-polaron transition match the frequency

Table 6.1: Frequency shift $\Delta\nu$ from the bare atomic transition frequencies to the second resonances on the 12 to 13 rf spectra near 12 Feshbach resonance. The corresponding axial trap frequency is ν_z. Two measured values of $\Delta\nu$ based on two fits are compared to the values calculated assuming a transition from a 1-2 polaron to a 1-3 polaron. $\Delta\nu_{meas1}$ corresponds to the fit in our paper [4] and $\Delta\nu_{meas2}$ corresponds to the fit I use in this dissertation. $\Delta\nu_{polaron1}$ is calculated from polaron binding energy function (4.20) with $\lambda_1 = 0.67$ while $\Delta\nu_{polaron2}$ is from the approximate function (4.21) with $\lambda_1 = 0.54$.

B(G)	ν_z(kHz)	$\Delta\nu_{meas1}$(kHz)	$\Delta\nu_{meas2}$(kHz)	$\Delta\nu_{polaron1}$(kHz)	$\Delta\nu_{polaron2}$(kHz)
809	24.0	18.7	20.0	18.3	18.6
810	85.0	37.1	36.4	37.0	38.3
842	24.5	10.1	10.3	9.7	9.5
842	82.5	27.2	28.1	26.7	26.8
832	24.5	12.3	12.6	11.6	11.6
832	82.0	28.3	28.0	29.1	29.5
832	135	38.8	38.8	42.8	43.4
831	179	44.5	43.6	48.3	49.8

shifts quite good. We believe the polaron transition should play an important part in the spectrum.

I also list the calculation result based on the approximated polaron binding energy function (4.21) as $\Delta\nu_{polaron2}$ in the table with $\lambda_1 = 0.54$. Although here the λ_1 is different, we can see that $\Delta\nu_{polaron1}$ and $\Delta\nu_{polaron2}$ are quite close. That means the subtraction of the polaron binding energies given by the approximated function is very close to the accurate calculation, although there should be noticeable difference from the accurate calculation for the polaron binding energy itself.

6.3 Spectra for different temperatures and atom numbers

Besides changing magnetic field and trap depth, we also change other parameters in the quasi 2D rf spectroscopy experiment to see how spectrum change accordingly. Here I will show you the spectra for different temperatures and atom numbers of the system.

6.3.1 Spectra for different temperatures

We change the temperature of the system before we apply rf pulse to make the transitions. In Figure 6.21, we have two 12 to 13 transition spectra at 832 G. For spectrum in Figure 6.21 (a), it is colder compared with 6.21 (b) while other parameters are nominally the same. We can see that the second resonance on the right side is more obvious when the system is colder. I list the positions of the polaron transition peaks in purple dot-dashed lines and the dimer transition peaks in red dotted and dashed lines. We can see that when system temperature is low, the broad resonance position match with the polaron transition resonance very well. However, when the system temperature become higher, the broad resonance position moves to the left a little bit. And in the place where the dimer transition should be, there is a abrupt shape change of the spectrum.

We also have the experimental data for different temperatures at 842G for both 2% and 20% trap depths. In Figure 6.22, we can see that the spectrum has the similar change as in 832G data when system temperature increases. And in Figure 6.23 where I list three different temperatures, we can see the change of spectrum shape more clearly.

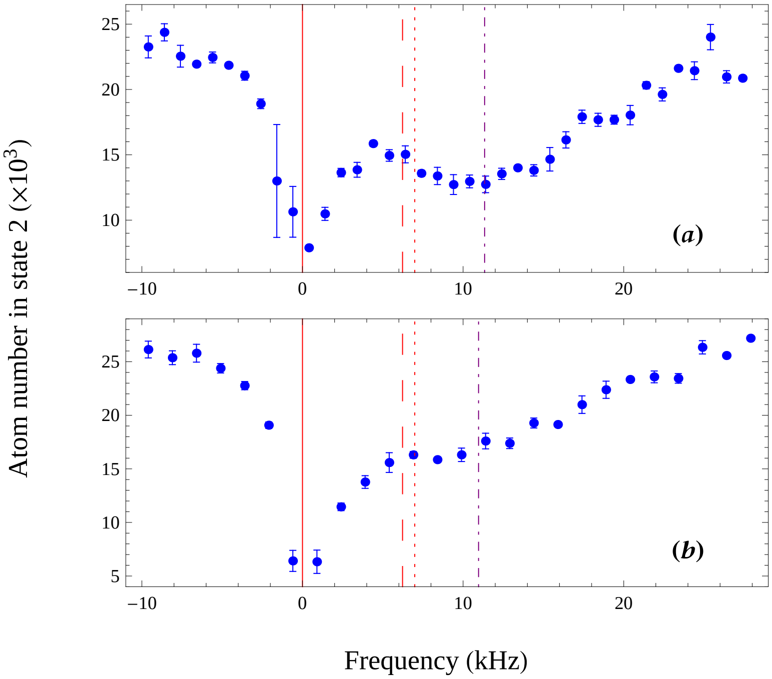

a	N_{site}	1657
	E_F	26.7kHz
	E_{p12}	23.96kHz
	E_{p13}	12.62kHz
b	N_{site}	1420
	E_F	24.7kHz
	E_{p12}	22.85kHz
	E_{p13}	11.89kHz

Figure 6.21: 12 to 13 rf spectra for different temperatures at 832 G, 2% trap depth, $\nu_z = 24.5$ kHz. Temperature of the system in (a) is lower than that in (b). We set the origin of x axis to be 81.7076 MHz corresponding the bare 2 to 3 atomic transition frequency shown as red solid lines. Red dotted lines are the calculated positions of dimer bound state to scattering state transition resonance while red dashed lines correspond dimer bound to bound transition resonance. Positions of polaron transition resonances are shown as purple dot-dashed lines.

I need to mention that for these rf spectra taken around 1-2 Feshbach resonance, the dimer transition predict same resonance positions for different spectra, as long as the optical trap depths are the same. However, the polaron transition resonance position would vary since it depends on atom number per site in the 2D system which is different for different cases. So, In Figure 6.21, 6.22 and 6.23, for one set of data, the red lines are always line up in different subfigures while the position of purple dot-dashed lines are slightly different.

We also turn the temperature knob around 1-3 mixture Feshbach resonance around 690 G for 1-3 to 1-2 rf transition. In Figure 6.24, I show two spectra

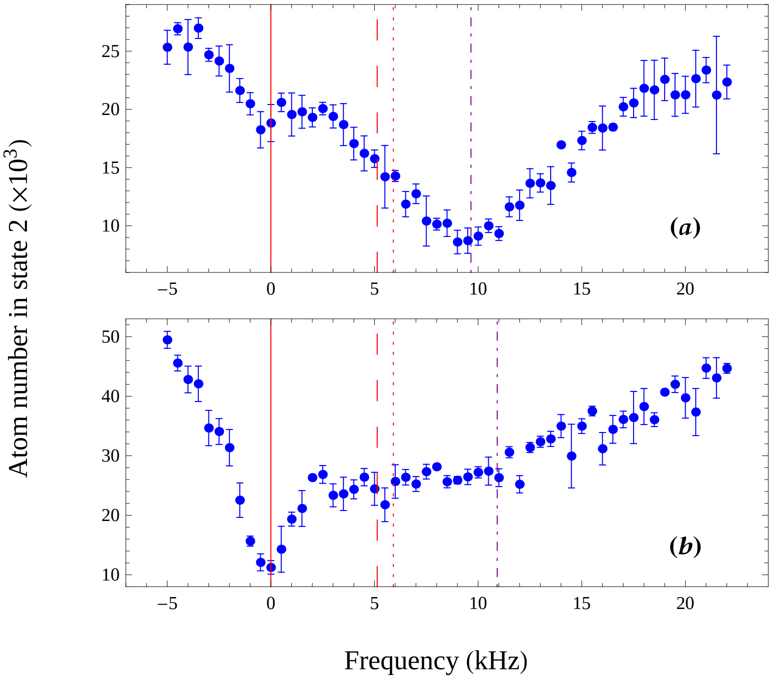

a	N_{site}	1420
	E_F	25.8kHz
	E_{p12}	22.01kHz
	E_{p13}	12.36kHz
b	N_{site}	2403
	E_F	33.5kHz
	E_{p12}	26.10kHz
	E_{p13}	15.18kHz

Figure 6.22: 12 to 13 rf spectra for different temperatures at 841.7 G, 2% trap depth, $\nu_z = 24.5$ kHz. Temperature of the system in (a) is lower than that in (b). We set the origin of x axis to be 81.653 MHz corresponding the bare 2 to 3 atom transition frequency shown as red solid lines. Red dotted lines are the calculated positions of dimer bound state to scattering state transition resonance while red dashed lines correspond dimer bound to bound transition resonance. Positions of polaron transition resonances are shown as purple dot-dashed lines.

with different temperatures for 2% trap depths. Here, the 12 dimer binding energy is too big to let polaron transition dominate. Therefore, I only label the resonance positions for dimer transitions. We can see that although the dimer theory can not predict the exact positions of the resonance on the right side, the error (around 30kHz) is quite small considering the resonance on the right is very far away from the atomic transition resonance (more than 300kHz). And while the temperature increase, it is obvious that the tail on the left side of the atomic transition resonance becomes smaller and for the resonance on the right side, the left part of it become smaller as well. These changes are consistent with

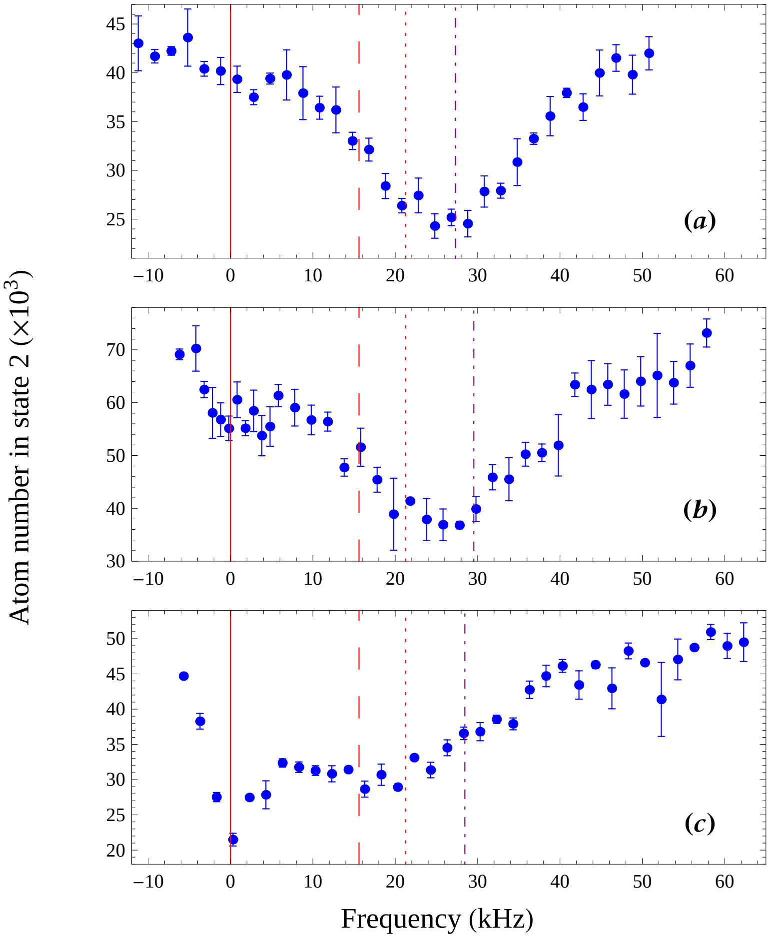

a	N_{site}	1941
	E_F	101.5kHz
	E_{p12}	83.87kHz
	E_{p13}	56.27kHz
b	N_{site}	2628
	E_F	118.1kHz
	E_{p12}	92.57kHz
	E_{p13}	63.03kHz
c	N_{site}	2225
	E_F	108.6kHz
	E_{p12}	87.66kHz
	E_{p13}	59.21kHz

Figure 6.23: 12 to 13 rf spectra for different temperatures at 842.4 G, 20% trap depth, $\nu_z = 82.5$ kHz. From data (a) to (c), temperature of the systems increases. We set the origin of x axis to be 81.6492 MHz corresponding the bare 2 to 3 atom transition frequency shown as red solid lines. Red dotted lines are the calculated positions of dimer bound state to scattering state transition resonance while red dashed lines correspond dimer bound to bound transition resonance. Positions of polaron transition resonances are shown as purple dot-dashed lines.

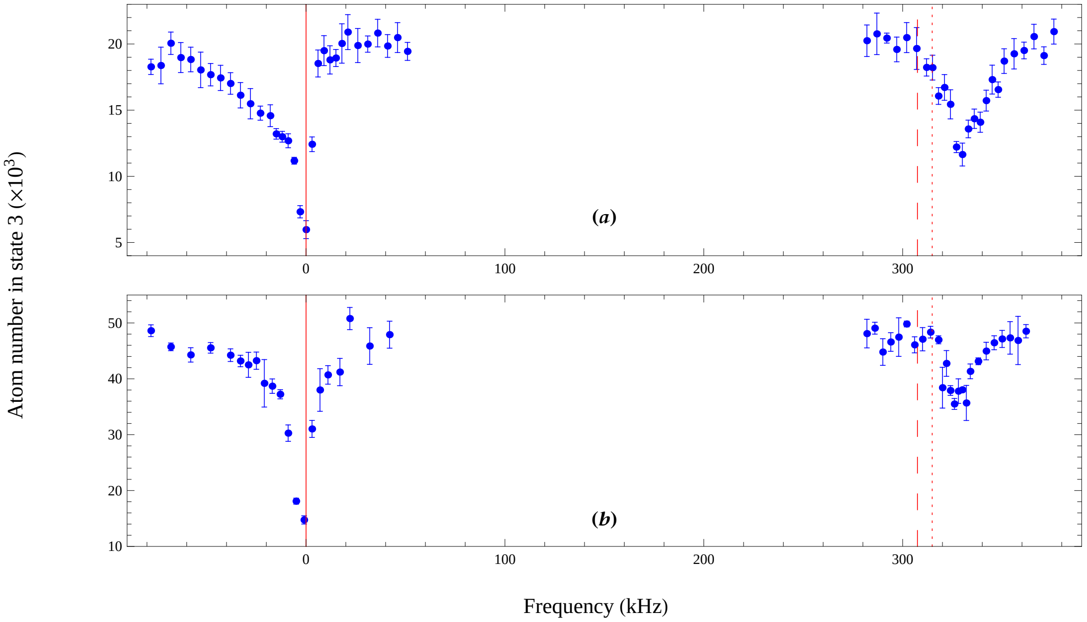

Figure 6.24: 13 to 12 rf spectra for different temperatures at 690 G, 2% trap depth, $\nu_z = 24.5$ kHz. Temperature of the system in (a) is lower than that in (b). We set the origin of x axis to be 82.718 MHz corresponding the bare 3 to 2 atom transition frequency shown as red solid lines. Red dotted lines are the calculated position for dimer scattering state to bound state transition resonance while red dashed lines correspond dimer bound to bound transition resonance.

the dimer transition assumption, which predicts that the transition from initial dimers should be suppressed with the decreasing of the dimer number while system temperature increases.

6.3.2 Spectra for different atom numbers

Then let's take a look at another parameter, number of atoms. Here we want to change the number of atoms per pancake in the 2D system $N_{pancake}$ since it will change the Fermi energy of the system as well. Compared with the obvious change of the spectrum shape when the system temperature varies, the change of the spectrum is quite small when we try to change $N_{pancake}$. In Figure 6.25, we have data at around 1-2 Feshbach resonance, 832 G for different $N_{pancake}$. System of Figure 6.25(b) has almost twice $N_{pancake}$ as system of Figure 6.25(a) has. In subfigure (c), I put both spectra in and scale them vertically to show the shape difference. We can see a tiny shift of the broader peak in subfigure (b) with respect to the one in (a). And for both spectra, the polaron transition theory predict the resonance positions quite well.

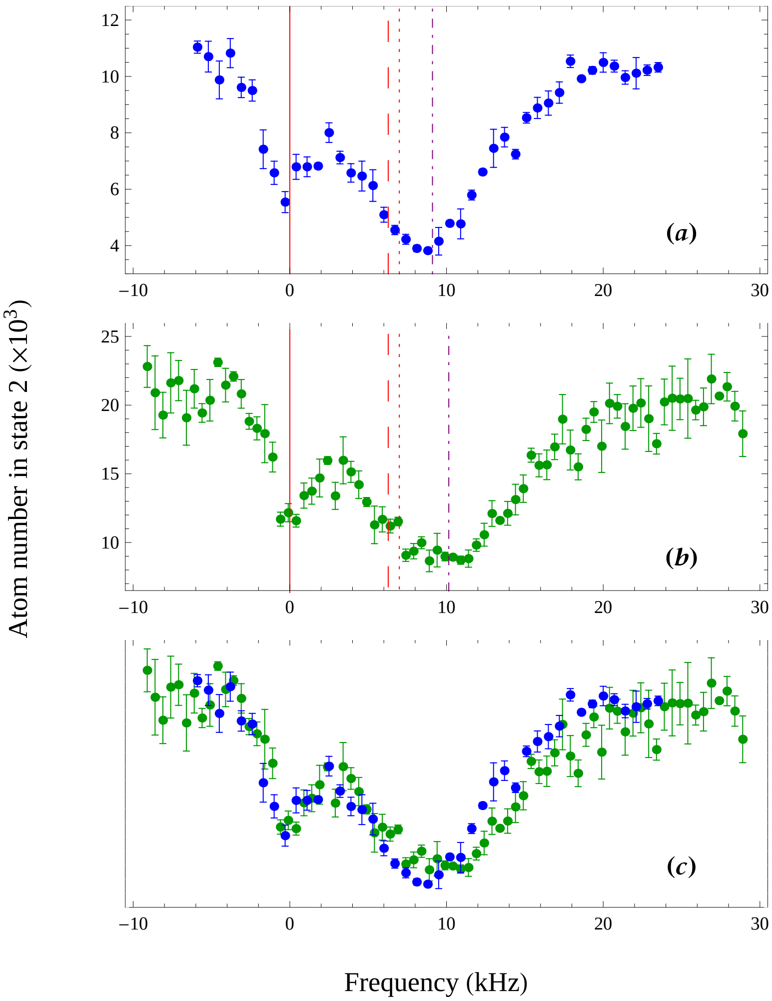

a	$N_{pancake}$	690
	E_F	16.51kHz
	E_{p12}	17.69kHz
	E_{p13}	8.59kHz
b	$N_{pancake}$	1180
	E_F	21.58kHz
	E_{p12}	20.68kHz
	E_{p13}	10.54kHz

Figure 6.25: 12 to 13 rf spectra for different atom number per pancake of quasi-2D system at 832.1 G, at 20% trap depth. (a) and (b) are data with different atom number per pancake while (c) is the comparison of the shape of (a) and (b). We set the origin of x axis to be 81.7071 MHz corresponding the bare 2 to 3 atom transition frequency shown as red solid lines. Red dotted lines are the calculated positions of dimer bound state to scattering state transition resonance while red dashed lines correspond dimer bound to bound transition resonance. Positions of polaron transition resonances are shown as purple dot-dashed lines.

Chapter 7

Conclusion

7.1 Summary of the dissertation

This dissertation presented the experimental results of radio-frequency spectroscopy in a unique geometry, quasi-two dimensional Fermi gas with $E_{F\perp} = 1.5h\nu_z$, as well as theoretical fitting. Although, 50-50 two component mixture is employed, we notice that the two dimensional non-interacting polaron transition theory fit our data much better than the corresponding dimer transition theory in the regime where $E_{F\perp}$ is comparable to E_b.

This is the first study of pairing in a quasi-two dimensional Fermi gas where we believe that our experimental results show many body effect in the strongly interacting region. Our experiments have spurred several theoretical works.

At least three theory groups tried to fit our data. Our polaron transition interpretation is supported by some of them, while other possible consequences have been discussed, like effects of higher axial states by using BCS theory. More theoretical work is required to fully understand our data.

7.2 Outlook

Based on my current work, the quasi-two dimensional system we explored has such a unique geometry which changes the system from pure 2D in a way we do not fully understand.

Next step, we can employ high resolution imaging system to take in situ images of atoms and to study the hydrodynamic expansion in this unique system. This may help us to find a reliable method to measure the temperature of the quasi-two dimensional system. For the radio frequency spectroscopy experiment, we also can do more accurate measurement with high resolution imaging by considering the inhomogeneous density in the harmonic trapping potential.

Based on the apparatus we have, we can add some equipments to give us more freedom to play with the system. For example, by adding one or two lasers we can modify the dimensionality even further. If we can upgrade the magnets system with fast response, interaction between atoms can be changed with no time. I believe more interesting experiments can be done in the near future.

Ultracold Fermi gas is such an amazing system that many researchers jump into this exciting field and do research experimentally and theoretically in order to understand its properties and interplay with Bose system. There were only six pioneer experimental groups in the ultracold Fermi gas field including our group around 2000. Till now, there are more than 200 research groups in the world studying ultracold atoms experimentally and theoretically. It is for sure that the investigation in this field has endless potential.

Appendix A

Mathematica file for ^{6}Li hyperfine structure

PROGRAM DESCRIPTION:

This Mathematica 8.0 program calculates ^{6}Li Hyperfine energies in a certain magnetic field, plots the energy level versus magnetic field, at last shows energy difference in some particular magnetic fields. Here energies are given in units of the hyperfine constant, a, where $3a/2 = 228.2MHz$ is the $F = 3/2 - F = 1/2$ splitting at $B = 0$. Note that $mu0 * B/a = 92.00 * B$ is the shift of a Bohr magneton per Tesla in units of a. Energies are plotted from $E1$ to $E6$ with $E1$ lowest.

```
gI = .0004476540  (* see Rev.Mod.Physics Vol .49 No .1, 1977  *);
gJ = -2.0023010(* see Rev.Mod.Physics Vol .49 No .1, 1977 *);
mu0 = 9.2740154 10^-24;
h = 6.6260755 10^-34;
\[Mu]0 = 1.399624604*10^10  (* Bohr magneton in Hz/T *)
a = 152.1368407 *10^6 (* Hz *)
q = \[Mu]0/a*(-gJ + gI)/2

zp[B_] := 1/2 + 2*q*B
rp[B_] := Sqrt[2 + (zp[B])^2]
sp[B_] := 1/Sqrt[1 + (zp[B] + rp[B])^2/2]
cp[B_] := Sqrt[1 - sp[B]^2]

zm[B_] := -1/2 + 2*q*B
rm[B_] := Sqrt[2 + (zm[B])^2]
sm[B_] := 1/Sqrt[1 + (zm[B] + rm[B])^2/2]
cm[B_] := Sqrt[1 - sm[B]^2]
```

```
energy1[B_] := -1/4 - rp[B]/2 - gI \[Mu]0 B/(2 a)
energy2[B_] := -1/4 - rm[B]/2 + gI \[Mu]0 B/(2 a)
energy3[B_] := 1/2 + gJ \[Mu]0 B/ (2 a) + gI \[Mu]0 B/ a
energy4[B_] := -1/4 + rm[B]/2 + gI \[Mu]0 B/(2 a)
energy5[B_] := -1/4 + rp[B]/2 - gI \[Mu]0 B/(2 a)
energy6[B_] := 1/2 - gJ \[Mu]0 B/ (2 a) - gI \[Mu]0 B/ a

Plot[{energy1[B/10000], energy2[B/10000], energy3[B/10000],
  energy4[B/10000], energy5[B/10000], energy6[B/10000]}, {B, 0, 1200},
  PlotRangeClipping -> True, Frame -> True,
 FrameLabel -> {Style["Magnetic field (B)", FontSize -> 13],
   Style["Hyperfine energies in units of \!\(\*FractionBox[\(a\), \(h\
\)]\)", FontSize -> 12]},
 PlotStyle -> {Red, Red, Blue, Blue, Blue, Blue}]

a*(energy2[0.08341] - energy1[0.08341])
a*(energy2[0.0830] - energy1[0.0830])
a*(energy3[0.08414] - energy2[0.08414])
```

Bibliography

[1] Andrea M. Fischer and Meera M. Parish. Bcs-bec crossover in a quasi-two-dimensional fermi gas. arXiv:1301.5236, 2013.

[2] A. Schirotzek, C.-H. Wu, A. Sommer, and M. W. Zwierlein. Observation of fermi polarons in a tunable fermi liquid of ultracold atoms. *Phys. Rev. Lett.*, 102:230402, 2009.

[3] E. Vogt M. Koschorreck W. Zwerger B. Fröhlich, M. Feld and M. Köhl. Radio-frequency spectroscopy of a strongly interacting two-dimensional fermi gas. *Phys. Rev. Lett.*, 106:105301, 2011.

[4] Y. Zhang, W. Ong, I. Arakelyan, and J. E. Thomas. Polaron-to-polaron transitions in the radio-frequency spectrum of a quasi-two-dimensional fermi gas. *Phys. Rev. Lett.*, 108:235302, 2012.

[5] Mohit Randeria, Ji-Min Duan, and Lih-Yir Shieh. Bound states, cooper pairing, and bose condensation in two dimensions. *Phys. Rev. Lett.*, 62:981, 1989.

[6] Richard Schmidt, Tilman Enss, Ville Pietilä, and Eugene Demler. Fermi polarons in two dimensions. *Phys. Rev. A*, 85:021302(R), 2012.

[7] Ville Pietilä. Pairing and radio-frequency spectroscopy in two-dimensional fermi gases. *Phys. Rev. A*, 86:023608, 2012.

[8] B. DeMarco and D. S. Jin. Onset of Fermi degeneracy in a trapped atomic gas. *Science*, 285:1703, 1999.

[9] A. G. Truscott, K. E. Strecker, W. I. McAlexander, G. B. Partridge, and R. G Hulet. Observation of Fermi pressure in a gas of trapped atoms. *Science*, 291:2570, 2001.

[10] K. Dieckmann, C. A. Stan, S. Gupta, Z. Hadzibabic, C. H. Schunck, and W. Ketterle. Decay of an ultracold fermionic lithium gas near a Feshbach resonance. *Phys. Rev. Lett.*, 89:203201, 2002.

[11] F. Schreck, L. Kaykovich, K. L. Corwin, G. Ferrari, T. Bourdel, J. Cubizolles, and C. Salomon. Quasipure Bose-Einstein condensate immersed in a Fermi sea. *Phys. Rev. Lett.*, 87:080403, 2001.

[12] S. R. Granade, M. E. Gehm, K. M. O'Hara, and J. E. Thomas. All-optical production of a degenerate Fermi gas. *Phys. Rev. Lett.*, 88(12):120405, 2002.

[13] S. Jochim, M. Bartenstein, G. Hendl, J. Hecker Denschlag, R. Grimm, A. Mosk, and M. Weidemüller. Magnetic field control of elastic scattering in a cold gas of fermionic lithium atoms. *Phys. Rev. Lett*, 89:273202, 2002.

[14] K. M. O'Hara, S. L. Hemmer, M. E. Gehm, S. R. Granade, and J. E. Thomas. Observation of a strongly interacting degenerate Fermi gas of atoms. *Science*, 298:2179, 2002.

[15] Immanuel Bloch, Jean Dalibard, and Wilhelm Zwerger. Many-body physics with ultracold gases. *Rev. Mod. Phys.*, 80:885, 2008.

[16] Stefano Giorgini, Lev P. Potaevski, and Sandro Stringari. Theory of ultracold atomic fermi gases. *Rev. Mod. Phys.*, 80:1215, 2008.

[17] W. Ketterle and M. W. Zwierlein. "Making, probing and understanding ultracold Fermi gases" in Ultracold Fermi Gases, Proceedings of the International School of Physics, Enrico Fermi, pp.95-287. *Rivista del Nuovo Cimento*, 31:247–422, 2008.

[18] G. A. Baker Jr. Neutron matter model. *Phys. Rev. C*, 60:054311, 1999.

[19] P. K. Kovtun, D. T. Son, and A. O. Starinets. Viscosity in strongly interacting quantum field theories from black hole physics. *Phys. Rev. Lett.*, 94:111601, 2005.

[20] J. Kinnunen, M. Rodríguez, and P. Törmä. Pairing gap and in-gap excitations in trapped fermionic superfuids. *Science*, 305:1131, 2004.

[21] A. Perali, P. Pieri, and G.C. Strinati. Quantitative comparison between theoretical predictions and experimental results for the BCS-BEC crossover. *Phys. Rev. Lett.*, 93:100404, 2004.

[22] Joseph Kinast, Andrey Turlapov, John E. Thomas, Qijin Chen, Jelena Stajic, and Kathryn Levin. Heat capacity of a strongly interacting Fermi gas. *Science*, 307:1296–1299, 2005.

[23] P. Massignan, G. M. Bruun, and H. Smith. Viscous relaxation and collective oscillations in a trapped Fermi gas near the unitarity limit. *Phys. Rev. A*, 71:033607, 2005.

[24] H. Hu, X. J. Liu, and P. D. Drummond. Temperature of a trapped unitary fermi gas at finite entropy. *Phys. Rev. A*, 73:023617, 2006.

[25] A. Bulgac, J. E. Drut, and P. Magierski. Spin 1/2 fermions in the unitary regime: A superfluid of a new type. *Phys. Rev. Lett.*, 96:090404, 2006.

[26] Cheng Chin, Rudolf Grimm, Paul Julienne, and Eite Tiesinga. Feshbach resonances in ultracold gases. *Rev. Mod. Phys.*, 82:1225, 2010.

[27] H. Feshbach. A unified theory of nuclear reactions II. *Ann. Phys.*, 19:287, 1962.

[28] E. Tiesinga and B.J. Verhaar andH. Y. C. Stoof. Threshold and resonance phenomena in ultracold ground-state collisions. *Phys. Rev. A*, 47:4114, 1993.

[29] M. Bartenstein, A. Altmeyer, S. Riedl, R. Geursen, S. Jochim, C. Chin, J. H. Denschlag, R. Grimm, A. Simoni, E. Tiesinga, C.J. Williams, and P.S. Julienne. Precise determination of ^{6}Li cold collision parameters by radio-frequency spectroscopy on weakly bound molecules. *Phys. Rev. Lett.*, 94:103201, 2005.

[30] C. A. Regal, M. Greiner, and D. S. Jin. Observation of resonance condensation of fermionic atom pairs. *Phys. Rev. Lett.*, 92:040403, 2004.

[31] M. W. Zwierlein, C. A. Stan, C. H. Schunck, S. M. F. Raupach, A. J. Kerman, and W. Ketterle. Condensation of pairs of fermionic atoms near a Feshbach resonance. *Phys. Rev. Lett.*, 92:120403, 2004.

[32] J. Kinast, S. L. Hemmer, M.E. Gehm, A. Turlapov, and J. E. Thomas. Evidence for superfluidity in a resonantly interacting Fermi gas. *Phys. Rev. Lett.*, 92:150402, 2004.

[33] M. Bartenstein, A. Altmeyer, S. Riedl, S. Jochim, C. Chin, J. Hecker Denschlag, and R. Grimm. Collective excitations of a degenerate gas at the BEC-BCS crossover. *Phys. Rev. Lett.*, 92:203201, 2004.

[34] C. Chin, M. Bartenstein, A. Altmeyer, S. Riedl, S. Jochim, J. Hecker Denschlag, and R. Grimm. Observation of the pairing gap in a strongly interacting Fermi gas. *Science*, 305:1128, 2004.

[35] G. B. Partridge, W. Li, R. I Kamar, Y. Liao, and R. G. Hulet. Pairing and phase separation in a polarized Fermi gas. *Science*, 311, 2006.

[36] C. H. Schunck, Y. Shin, A. Schirotzek, M. W. Zwierlein, and W. Ketterle. Pairing without superfluidity: The ground state of an imbalanced fermi mixture. *Science*, 316:867, 2007.

[37] Niels Henrik Abel. *Oeuvres Completes.* Johnson Reprint Corp., New York, 1998.

[38] Y. Shin, C. H. Schunck, A. Schirotzek, and W. Ketterle. Tomographic r-f spectroscopy of a trapped fermi gas at unitarity. *Phys. Rev. Lett.*, 99:090403, 2007.

[39] C. H. Schunck, Y. Shin, A. Schirotzek, and W. Ketterle. Determination of the fermion pair size in a resonantly interacting superfluid. *Nature*, 454:739, 2008.

[40] C. H. Schunck. PhD thesis, MIT, 2008.

[41] S. M. Reimann and M. Manninen. Electronic structure of quantum dots. *Rev. Mod. Phys.*, 74:1283, 2002.

[42] R. G. Hulet, E. S. Hilfer, and D. Kleppner. Inhibited spontaneous emission by a rydberg atom. *Phys. Rev. Lett.*, 55:2137, 1985.

[43] D. J. Heinzen, J. J. Childs, J. E. Thomas, and M. S. Feld. Enhanced and inhibited visible spontaneous emission by atoms in a confocal resonator. *Phys. Rev. Lett.*, 58:1320, 1987.

[44] G. Gabrielse and H. Dehmelt. Observation of inhibited spontaneous emission. *Phys. Rev. Lett.*, 55:67, 1985.

[45] Yang Guo, Yan-Feng Zhang, Xin-Yu Bao, Tie-Zhu Han, Zhe Tang, Li-Xin Zhang, Wen-Guang Zhu, E. G. Wang, Qian Niu, Z. Q. Qiu, Jin-Feng Jia, Zhong-Xian Zhao, and Qi-Kun Xue. Superconductivity modulated by quantum size effects. *Science*, 306:1915, 2004.

[46] Yoichi Yanase, Takanobu Jujo, Takuji Nomura, Hiroaki Ikeda, Takashi Hotta, and Kosaku Yamada. Theory of superconductivity in strongly correlated electron systems. *Phys. Rep.*, 387:1, 2003.

[47] M. Neumann, J. Nyéki, B. Cowan, and J. Saunders. Bilayer 3he: A simple two-dimensional heavy-fermion system with quantum criticality. *Science*, 317:1356, 2007.

[48] A. Görlitz, J. M. Vogels, A. E. Leanhardt, C. Raman, T. L. Gustavson, J. R. Abo-Shaeer, A. P. Chikkatur, S. Gupta, S. Inouye, T. Rosenband, and W. Ketterle. Realization of Bose-Einstein condensates in lower dimensions. *Phys. Rev. Lett.*, 87:130402, 2001.

[49] M. Greiner, I. Bloch, O. Mandel, T.W. Hänsch, and T. Esslinger. Bose-Einstain condensates in 1D-and 2D optical lattices. *Appl. Phys. B*, 73:769, 2001.

[50] M. Greiner, I. Bloch, O. Mandel, T.W. Hänsch, and T. Esslinger. Exploring phase coherence in a 2d lattice of Bose-Einstein condensates. *Phys. Rev. Lett.*, 87:160405, 2001.

[51] Belén Paredes, Artur Widera, Valentin Murg, Olaf Mandel, Simon Fölling, Ignacio Cirac, Gora V. Shlyapnikov, Theodor W. H?nsch, and Immanuel Bloch. Tonkscgirardeau gas of ultracold atoms in an optical lattice. *Nature*, 429:277, 2004.

[52] H. Moritz, T. Stöferle, K. Günter, M. Köhl, and T. Esslinger. Confinement induced molecules in a 1d fermi gas. *Phys. Rev. Lett.*, 94:210401, 2005.

[53] J.-P. Martikainen and P. Törmä. Quasi-two-dimensional superfluid fermionic gases. *Phys. Rev. Lett.*, 95:170407, 2005.

[54] G. Bertaina and S. Giorgini. Bcs-bec crossover in a two-dimensional fermi gas. *Phys. Rev. Lett.*, 106:110403, 2011.

[55] A. T. Sommer, L. W. Cheuk, M. J.-H. Ku, W. S. Bakr, and M. W. Zwierlein. Evolution of fermion pairing from three to two dimensions. *Phys. Rev. Lett.*, 108:045302, 2012.

[56] D. S. Petrov, M. Holzmann, and G. V. Shlyapnikov. Bose-einstein condensation in quasi-2d trapped gases. *Phys. Rev. Lett.*, 84:2551, 2000.

[57] D. S. Petrov and G. V. Shlyapnikov. Interatomic collisions in a tightly confined bose gas. *Phys. Rev. A*, 64:012706, 2001.

[58] M. Wouters, J. Tempere, and J. T. Devreese. Feshbach resonances in a quasi-two-dimensional atomic gas. *Phys. Rev. A*, 68:053603, 2003.

[59] Pascal Naidon, Eite Tiesinga, William F Mitchell, and Paul S Julienne. Effective-range description of a bose gas under strong one- or two-dimensional confinement. *New J. Phys.*, 9:19, 2007.

[60] Kirill Martiyanov, Vasiliy Makhalov, and Andrey Turlapov. Observation of a two-dimensional fermi gas of atoms. *Phys. Rev. Lett.*, 105:030404, 2010.

[61] Sascha Zöllner, G. M. Bruun, and C. J. Pethick. Polarons and molecules in a two-dimensional fermi gas. *Phys. Rev. A*, 83:021603, 2011.

[62] Meera M. Parish. Polaron-molecule transitions in a two-dimensional fermi gas. *Phys. Rev. A*, 83:051603, 2011.

[63] M. Houbiers, H. T. C. Stoof, W. I. McAlexander, and R. G. Hulet. Elastic and inelastic collisions of ^{6}Li atoms in magnetic and optical traps. *Phys. Rev. A*, 57:R1497, 1998.

[64] KersonHuang. *Statistical Mechanics.* John Wiley, New York,, 2th edition, 1987.

[65] F. Chevy. Universal phase diagram of a strongly interacting fermi gas with unbalanced spin populations. *Phys. Rev. A*, 74:063628, 2006.

[66] Michael Klawunn and Alessio Recati. Fermi polaron in two dimensions: Importance of the two-body bound state. *Phys. Rev. A*, 84:033607, 2011.

[67] K. M. O'Hara. *Optical Trapping and Evaporative Cooling of Fermionic Atoms.* PhD thesis, Duke University, 2000.

[68] J. M. Kinast. *Thermodynamics and Superfluidity of a Strongly Interacting Fermi Gas.* PhD thesis, Duke University, 2006.

[69] K. E. Strecker, G. B. Partridge, and R. G. Hulet. Conversion of an atomic Fermi gas to a long-lived molecular Bose gas. *Phys. Rev. Lett.*, 91:080406, 2003.

[70] B. E. Clancy. *Hydrodynamics of a rotating strongly interacting Fermi gas.* PhD thesis, Duke University, 2008.

[71] L. Luo. *Entropy and superfluid critical parameters of a strongly interacting Fermi gas.* PhD thesis, Duke University, 2008.

Biography

Yingyi Zhang was born December 23, 1980 in Chongqing, China. In 1999, she graduated from Chongqing 29 high school. Later that year, she entered Beijing Normal University to pursue a physics major. After graduated with honor in May 2003, she entered Peking University and was awarded an S.M in Physics three years later. She came to the USA and enrolled at Duke University in August 2006. After joining Dr.John Thomas's research group on ultra-cold Fermi gases, she contributed to the pairing research in quasi-two dimensional Fermi gas using radio frequency spectroscopy. She was awarded an A.M. in physics in December 2009. She also received the Walter Gordy Fellowship in September 2012 before graduating with a Ph.D. in May 2013.